

EXTENSION OF THE ENTROPY VISCOSITY METHOD TO THE MULTI-D  
EULER EQUATIONS AND THE SEVEN EQUATIONS MODEL.

A Dissertation

by

MARC-OLIVIER GERARD DELCHINI

Submitted to the Office of Graduate and Professional Studies of  
Texas A&M University  
in partial fulfillment of the requirements for the degree of

DOCTOR OF PHILOSOPHY

Co-Chairs of Committee,	Jean C. Ragusa
	Jean Luc Guermond
Committee Members,	Jim Morel
	Yassin Hassan
	Ray Berry
Head of Department,	Yassin Hassan

December 2014

Major Subject: Nuclear Engineering Department

Copyright 2014 Marc-Olivier Gerard Delchini

## ABSTRACT

Lorem ipsum dolor sit amet, consectetur adipiscing elit. Integer lectus quam, condimentum quis bibendum eu, sollicitudin eget lacus. Praesent non sodales odio. Class aptent taciti sociosqu ad litora torquent per conubia nostra, per inceptos himenaeos. Nulla ac luctus sapien. Morbi cursus sapien eget lorem fermentum hendrerit. Nam ac erat dui, in cursus velit. Vivamus hendrerit porttitor nisi, ut porttitor lorem volutpat eget. In ligula ligula, euismod ut condimentum sit amet, pulvinar sit amet diam. Pellentesque interdum, ipsum ullamcorper consequat dignissim, sem arcu egestas mauris, vitae interdum sem tortor ut ante. Nunc blandit laoreet nisi, non rutrum lorem hendrerit quis. Cras nunc diam, convallis et feugiat at, auctor id libero. Nunc facilisis massa eu eros imperdiet vestibulum. Vestibulum ante ipsum primis in faucibus orci luctus et ultrices posuere cubilia Curae; Donec non velit vitae tortor blandit semper.

Etiam vitae dolor nulla. Ut eros odio, rhoncus eget placerat vitae, elementum ac ante. Proin vitae odio eu nisl pharetra mattis. Pellentesque habitant morbi tristique senectus et netus et malesuada fames ac turpis egestas. Phasellus fermentum lacus consectetur neque consequat ullamcorper. Cras blandit urna non dui consequat molestie. Curabitur viverra nibh at nisi semper faucibus. Nam egestas mauris a enim dignissim nec consectetur tortor rutrum. Mauris at nisi in est luctus congue ut mattis est. Ut pretium, mi quis elementum cursus, ante eros suscipit ligula, ut porttitor elit leo sed turpis. Nam sed dui ligula.

## DEDICATION

This is an optional page. Lorem ipsum dolor sit amet, consectetur adipiscing elit. Integer lectus quam, condimentum quis bibendum eu, sollicitudin eget lacus. Praesent non sodales odio. Class aptent taciti sociosqu ad litora torquent per conubia nostra, per inceptos himenaeos. Nulla ac luctus sapien. Morbi cursus sapien eget lorem fermentum hendrerit. Nam ac erat dui, in cursus velit. Vivamus hendrerit porttitor nisi, ut porttitor lorem volutpat eget. In ligula ligula, euismod ut condimentum sit amet, pulvinar sit amet diam. Pellentesque interdum, ipsum ullamcorper consequat dignissim, sem arcu egestas mauris, vitae interdum sem tortor ut ante. Nunc blandit laoreet nisi, non rutrum lorem hendrerit quis. Cras nunc diam, convallis et feugiat at, auctor id libero. Nunc facilisis massa eu eros imperdiet vestibulum. Vestibulum ante ipsum primis in faucibus orci luctus et ultrices posuere cubilia Curae; Donec non velit vitae tortor blandit semper.

Etiam vitae dolor nulla. Ut eros odio, rhoncus eget placerat vitae, elementum ac ante. Proin vitae odio eu nisl pharetra mattis. Pellentesque habitant morbi tristique senectus et netus et malesuada fames ac turpis egestas. Phasellus fermentum lacus consectetur neque consequat ullamcorper. Cras blandit urna non dui consequat molestie. Curabitur viverra nibh at nisi semper faucibus. Nam egestas mauris a enim dignissim nec consectetur tortor rutrum. Mauris at nisi in est luctus congue ut mattis est. Ut pretium, mi quis elementum cursus, ante eros suscipit ligula, ut porttitor elit leo sed turpis. Nam sed dui ligula.

## ACKNOWLEDGEMENTS

Lorem ipsum dolor sit amet, consectetur adipiscing elit. Integer lectus quam, condimentum quis bibendum eu, sollicitudin eget lacus. Praesent non sodales odio. Class aptent taciti sociosqu ad litora torquent per conubia nostra, per inceptos himenaeos. Nulla ac luctus sapien. Morbi cursus sapien eget lorem fermentum hendrerit. Nam ac erat dui, in cursus velit. Vivamus hendrerit porttitor nisi, ut porttitor lorem volutpat eget. In ligula ligula, euismod ut condimentum sit amet, pulvinar sit amet diam. Pellentesque interdum, ipsum ullamcorper consequat dignissim, sem arcu egestas mauris, vitae interdum sem tortor ut ante. Nunc blandit laoreet nisi, non rutrum lorem hendrerit quis. Cras nunc diam, convallis et feugiat at, auctor id libero. Nunc facilisis massa eu eros imperdiet vestibulum. Vestibulum ante ipsum primis in faucibus orci luctus et ultrices posuere cubilia Curae; Donec non velit vitae tortor blandit semper.

Etiam vitae dolor nulla. Ut eros odio, rhoncus eget placerat vitae, elementum ac ante. Proin vitae odio eu nisl pharetra mattis. Pellentesque habitant morbi tristique senectus et netus et malesuada fames ac turpis egestas. Phasellus fermentum lacus consectetur neque consequat ullamcorper. Cras blandit urna non dui consequat molestie. Curabitur viverra nibh at nisi semper faucibus. Nam egestas mauris a enim dignissim nec consectetur tortor rutrum. Mauris at nisi in est luctus congue ut mattis est. Ut pretium, mi quis elementum cursus, ante eros suscipit ligula, ut porttitor elit leo sed turpis. Nam sed dui ligula.

## NOMENCLATURE

$P$	Pressure
$T$	Temperature
$\vec{u}$	vector velocity
$\rho$	Density
$E$	specific total energy
$e$	specific internal energy
$P_I$	interfacial pressure
$\vec{u}_I$	interfacial velocity
$\mu$	viscosity coefficient
$\kappa$	viscosity coefficient
$\alpha$	void fraction
$\partial_t$	partial time derivative
eos	equation of state

This page is optional.

# TABLE OF CONTENTS

	Page
ABSTRACT . . . . .	ii
DEDICATION . . . . .	iii
ACKNOWLEDGEMENTS . . . . .	iv
NOMENCLATURE . . . . .	v
TABLE OF CONTENTS . . . . .	vi
LIST OF FIGURES . . . . .	viii
LIST OF TABLES . . . . .	xi
1. INTRODUCTION: . . . . .	1
2. DISCRETIZATION METHOD AND IMPLEMENTATION DETAILS OF THE ENTROPY VISCOSITY METHOD. . . . .	1
2.1 Implementation of the entropy viscosity method (EVM) with contin- uous Galerkin finite element method: . . . . .	1
3. APPLICATION OF THE ENTROPY VISCOSITY METHOD TO THE MULTI-D EULER EQUATIONS WITH VARIABLE AREA: . . . . .	4
3.1 Introduction . . . . .	4
3.2 The Entropy Viscosity Method . . . . .	6
3.2.1 Background . . . . .	6
3.2.2 Issues in the Low-Mach Regime . . . . .	9
3.2.3 The dissipative-terms for the multi-D Euler equations with variable area . . . . .	9
3.3 All-speed Reformulation of the Entropy Viscosity Method . . . . .	11
3.3.1 New Entropy Production Residual . . . . .	11
3.3.2 Low-Mach asymptotic study of the multi-D Euler equations . . . . .	12
3.4 Solution Techniques Spatial and Temporal Discretizations . . . . .	18
3.4.1 Spatial and Temporal Discretizations . . . . .	18
3.4.2 Boundary conditions . . . . .	19

3.4.3	Stagnation pressure boundary condition . . . . .	22
3.4.4	Back pressure outlet boundary condition for subsonic flow . .	25
3.4.5	Mass flow inlet boundary condition . . . . .	27
3.4.6	Outlet boundary condition for supersonic flow . . . . .	27
3.4.7	Solver . . . . .	27
3.5	1-D shock tubes: . . . . .	28
3.5.1	Liquid water in a 1-D divergent-convergent nozzle . . . . .	29
3.5.2	Steam in a 1-D divergent-convergent nozzle . . . . .	33
3.5.3	Leblanc shock tube . . . . .	39
3.5.4	Typical 1-D shock tubes [41] . . . . .	45
3.6	2-D numerical results for supersonic flows: . . . . .	45
3.6.1	Supersonic 2-D flow over a forward facing step: . . . . .	45
3.6.2	2-D circular explosion: . . . . .	46
3.6.3	Riemann problem number 12: . . . . .	56
3.6.4	Supersonic flow in a compression corner . . . . .	56
3.6.5	Supersonic flow over a 5° double-wedge obstruction: . . . . .	65
3.7	2-D numerical results for subsonic flows: . . . . .	69
3.7.1	Subsonic flow over a 2-D cylinder . . . . .	69
3.7.2	Subsonic flow over a 2-D hump . . . . .	73
3.8	Conclusions . . . . .	75
4.	APPLICATION OF THE ENTROPY VISCOSITY METHOD TO THE SEVEN EQUATIONS MODEL. . . . .	1
5.	APPLICATION OF THE ENTROPY VISCOSITY METHOD TO THE 1-D GREY RADIATION-HYDRODYNAMIC EQUATIONS. . . . .	2
5.1	Introduction . . . . .	2
5.2	The entropy-based viscosity method applied to the 1-D Radiation- Hydrodynamic equations . . . . .	5
5.3	Numerical scheme and solution technique . . . . .	11
5.4	Numerical results . . . . .	13
5.4.1	Space/time accuracy . . . . .	13
5.4.2	Radiation shock simulations . . . . .	18
5.5	Conclusions . . . . .	34
	REFERENCES . . . . .	36

## LIST OF FIGURES

FIGURE		Page
3.1	Steady-state solution for liquid phase in a 1-D convergent-divergent nozzle with an uniform mesh of 50 cells. . . . .	31
3.2	Steady-state solution for vapor phase in a 1-D convergent-divergent nozzle. . . . .	35
3.3	Velocity profile at steady-state with the first- and second-order viscosity for a mesh with 400 cells. . . . .	39
3.4	Numerical solution for the 1-D Leblanc shock tube at $t = 4.s$ . . . . .	41
3.5	Density solution at $t = 0.314 s$ . . . . .	48
3.6	Viscosity coefficient solution at $t = 0.314 s$ . . . . .	49
3.7	Density solution at $t = 0.664 s$ . . . . .	50
3.8	Viscosity coefficient solution at $t = 0.664 s$ . . . . .	51
3.9	Density solution at $t = 1.514 s$ . . . . .	52
3.10	Viscosity coefficient solution at $t = 1.514 s$ . . . . .	53
3.11	Density solution at $t = 4 s$ . . . . .	54
3.12	Viscosity coefficient solution at $t = 4 s$ . . . . .	55
3.13	Pressure solution at $t = 5.5 \times 10^{-4}$ . . . . .	58
3.14	Viscosity coefficient at $t = 5.5 \times 10^{-4}$ . . . . .	59
3.15	Pressure solution at $t = 1.15 \times 10^{-3}$ . . . . .	60
3.16	Viscosity coefficient at $t = 1.15 \times 10^{-3}$ . . . . .	61
3.17	Pressure solution at steady-state. . . . .	62
3.18	Viscosity coefficient at steady-state. . . . .	63



3.19	Pressure and Mach number profiles at steady-state . . . . .	64
3.20	Difference between inlet and outlet mass flow rates as a function of time. . . . .	65
3.21	Pressure solution at steady-state. . . . .	67
3.22	Viscosity coefficient at steady-state. . . . .	68
3.23	Steady-state solution at $M_\infty = 10^{-3}$ . . . . .	70
3.24	Steady-state solution at $M_\infty = 10^{-4}$ . . . . .	71
3.25	Steady-state solution at $M_\infty = 10^{-5}$ . . . . .	71
3.26	Steady-state solution at $M_\infty = 10^{-7}$ . . . . .	72
3.27	Mach 0.7: iso-Mach lines at steady-state. . . . .	74
3.28	Mach $10^{-2}$ : iso-Mach lines at steady-state. . . . .	74
3.29	Mach $10^{-5}$ : iso-Mach lines at steady-state. . . . .	74
3.30	Mach $10^{-7}$ : iso-Mach lines at steady-state. . . . .	75
5.1	Material and radiation temperature profiles at steady state for Mach 1.05 test. . . . .	20
5.2	Material density profile at steady state for Mach 1.05 test. . . . .	20
5.3	First-order viscosity $\kappa_{max}$ and second-order viscosity $\kappa$ profiles at steady state for Mach 1.05 test (logarithm scale). . . . .	21
5.4	Material and radiation temperature profiles at steady state for Mach 1.2 test. . . . .	22
5.5	Material density profile at steady state for Mach 1.2 test. . . . .	23
5.6	First-order viscosity $\kappa_{max}$ and second-order viscosity $\kappa$ profiles at steady state for Mach 1.2 test (logarithm scale). . . . .	24
5.7	Material and radiation temperature profiles at steady-state for Mach 2 test. . . . .	25
5.8	Material density profile at steady-state for Mach 2 test. . . . .	26

5.9	First-order viscosity $\kappa_{max}$ and second-order viscosity $\kappa$ profiles at steady state for Mach 2 test. . . . .	27
5.10	Comparison between the material density and temperature profiles run with the high-order and first-order viscosity coefficients. . . . .	27
5.11	Material and radiation temperature profiles at steady state for Mach 5 test. Zoom at the location of the peak using different mesh resolutions. . . . .	29
5.12	Material temperature profiles at steady state for the Mach 5 test in the neighborhood spike. . . . .	29
5.13	Material density profile at steady state for Mach 5 test. . . . .	30
5.14	First-order viscosity $\kappa_{max}$ and second-order viscosity $\kappa$ profiles at steady state for Mach 5 test. . . . .	31
5.15	Material and radiation temperature profiles at steady state for Mach 50 test. . . . .	32
5.16	Material density profile at steady-state for Mach 50 test. . . . .	33
5.17	First-order viscosity $\kappa_{max}$ and second-order viscosity $\kappa$ profiles at steady-state for Mach 50 test. . . . .	33

# LIST OF TABLES

TABLE	Page
3.1 Stiffened Gas Equation of State parameters for liquid water. . . . .	30
3.2 L1 norm of the error for the liquid phase in a 1-D convergent-divergent nozzle at steady-state. . . . .	32
3.3 L2 norm of the error for the liquid phase in a 1-D convergent-divergent nozzle at steady-state. . . . .	33
3.4 Stiffened Gas Equation of State parameters for steam. . . . .	34
3.5 L1 norm of the error for the vapor phase in a 1-D convergent-divergent nozzle at steady-state. . . . .	37
3.6 L2 norm of the error for the vapor phase in a 1-D convergent-divergent nozzle at steady-state. . . . .	38
3.7 Initial conditions for the 1-D Leblanc shock tube. . . . .	40
3.8 L1 norm of the error for the 1-D Leblanc test at $t = 4.s$ . . . . .	43
3.9 L2 norm of the error for the 1-D Leblanc test at $t = 4.s$ . . . . .	44
3.10 Initial conditions for a 2-D supersonic flow past a forward-facing step.	46
3.11 Initial conditions for a 2-D explosion. . . . .	47
3.12 Analytical solution for the supersonic flow on an edge eat $15^\circ$ at $M = 2.5$ .	57
3.13 Velocity ratio for different Mach numbers. . . . .	73
5.1 $L_2$ norms of the error for for the equilibrium diffusion limit case using a manufactured solution. . . . .	15
5.2 $L_2$ norms of the error for for the streaming limit case using a manufactured solution. . . . .	17
5.3 Initial conditions for Mach 1.05. . . . .	19

5.4	Initial conditions for Mach 1.2. . . . .	22
5.5	Initial conditions for Mach 2. . . . .	25
5.6	Initial conditions for Mach 5. . . . .	28
5.7	Initial conditions for Mach 50. . . . .	31

## 1. INTRODUCTION:

Hyperbolic systems of equations are encountered in various engineering fields (extraction of oil, turbine technology, nuclear reactors, etc ...). Improving numerical solution techniques for such equations are an ongoing topic of research. This is obviously the case for fluid equations. Being able to accurately solve and predict the behavior of a fluid in a turbine or in a reactor, for example, can lead to a safe decrease in conservative safety margins, which translates into a decrease in production cost. Thus, we can see the importance of having a good understanding of the mathematical theory behind these wave-dominated systems of equations, and also, the importance of developing robust and accurate numerical methods.

A large number of theoretical studies has shown the role played by characteristic equations and the corresponding eigenvalues on how and at what speed the physical information propagates: physical shocks or discontinuities can form, leading to unphysical instabilities and oscillations that pollute the numerical solution due to entropy production [41]. Thus, a question rises: how to accurately resolve shocks and conserve the physical solution at the same time? A lot of work is available in the literature and include Riemann solvers, Godunov-type fluxes, flux limiter and artificial viscosity methods. Toro's book [41] gives a good overview of the theory related to hyperbolic systems of equations and focuses on Riemann solvers and Godunov-type fluxes that can be used with discontinuous spatial discretizations: finite volume (FV) and discontinuous Galerkin finite element method (DGFEM). Flux limiters [5, 8] can achieve high-order accuracy with DGFEM [7] but suffer from some drawbacks: difficulties were found to reach steady-state solution when using time-stepping schemes and generalization to unstructured grids is not obvious [4]. The artificial

viscosity method was first introduced by Neumann and Richtmeyer [44] but was found over-dissipative and, thus, abandoned. It is only, later with the development of high-order schemes and because of their simple implementation that they have regained interest: Lapidus [25, 13] developed a high-order viscosity method by making the viscosity coefficient proportional to the gradient of the velocity in 1-D. Lohner et al. [31] extended this concept to multi-dimension by introducing a vector that will measure the direction of maximum change in the absolute value of the velocity norm, so that shear layers are not smeared. Pressure-based viscosities were also studied [30] where the viscosity coefficient is set proportional to the Laplace of pressure, allowing to detect curvature changes in the pressure profile. Since pressure is nearly constant but in shocks, it is a good indicator of the presence of a shock. Recently, Reisner et al. [39] introduced the C-method for the compressible Euler equations with artificial dissipative terms: instead of computing the viscosity coefficient on the fly as for Lapidus and pressure-based methods, a partial differential equation (PDE) is added to the original system of equations. This additional PDE allows to solve for the viscosity coefficient and contains a source term that is function of the gradient of velocity. The method seems to yield good results in 1-D for a wide range of tests. Guermond et al. [19, 20, 14] proposed an entropy-based viscosity method for conservative hyperbolic system of equations: artificial dissipative terms are added to the system of equations with a viscosity coefficient modulated by the entropy production that is known to be large in shocks and small everywhere else. The method was successfully applied in various schemes [20, 14, 43] and showed high-order convergence with smooth solutions. Results using the ideal gas equation of state were run for 1-D Sod tube and showed good agreement with the exact solutions. 2-D tests were also performed on unstructured grids and behaved very satisfactorily [43]. The method is fairly simple to implement and is consistent with the entropy inequality.

The objective of this research is to solve hyperbolic system of equations using a continuous Galerkin finite element method (CGFEM) and an implicit temporal discretization under the Moose framework [9]. We are particularly interested in simulating the flow behavior occurring in nuclear reactors. The set of equations that will be considered are the multi-D Euler equations with variable area [41] and the multi-D seven equations model for two-phase fluids [37]. These systems of equations are well defined in a sense that they possess real eigenvalues. To numerically solve these equations, we need to rely on a numerical method that will allow us to resolve shocks and discontinuity that may form. More importantly, we need a method that is accurate for a wide range of Mach numbers and is not restricted to any type of equation of state. These previous requirements can be hard to fulfill. Numerical methods are often tested with the ideal gas equation of state which can not be used for liquid phase. The difficulty rises once a numerical method used for resolving shocks, is required to work for low Mach flows that are isentropic: in this particular case, a compressible model is used to simulate a flow in the incompressible limit. Recent publications [16, 42] highlighted the difficulties related to such a choice: asymptotic studies have shown that some of the numerical methods become ill-scaled in the low Mach limit, making the numerical solution unphysical. For example, the Roe scheme requires a fix in the low Mach limit while conserving its accuracy when shocks occur [29].

We propose to use the entropy-based viscosity method introduced by Guermond et al. to solve for the hyperbolic systems previously enumerated since the method has shown good results when used for solving the multi-D Euler equations with various discretization schemes. More importantly, it is simple to implement, can be used with unstructured grids, and its dissipative terms are consistent with the entropy minimum principle and proven valid for any equation of state under certain con-

ditions [15]. However, a few questions remains: the low Mach limit has not been investigated and the current definition requires an analytical expression of the entropy which can be difficult to obtain for some equation of state. These two issues will be addressed. A particular attention will be brought to the low Mach problem and the available literature related to the asymptotic limit of the Navier-Stokes [34] and Euler equations [16, 42] should be of great insight in order to understand how the dissipative terms behave.

It is also proposed to investigate how the entropy viscosity method can be applied to the multi-D radiation-hydrodynamic equations [33]. These equations are known to develop solutions with shocks [3]. They consist of coupling the multi-D Euler equations with a radiation-diffusion equation through some source terms. Most of the current solvers are based on the study of the hyperbolic terms in order to derive a Riemann-type solver [38]. Flux-limiter technique [21] are also used and suffer from the same drawbacks as for the pure multi-D Euler equations. Therefore, it will be valuable to assess how the entropy viscosity method can adapt to this multi-physics system, and if successful, will offer an alternative to the current available numerical methods.

Thus, the proposal is organized as follows: Section 1 will recall the main feature of the current version of the entropy-based viscosity method. Section 2 will introduce the system of equations under considerations. A short description of the equations and their properties will be given. In Section 3, the problem formulation is discussed for each system of equations and suggestions of test cases are given in order to test the numerical method.



## 2. DISCRETIZATION METHOD AND IMPLEMENTATION DETAILS OF THE ENTROPY VISCOSITY METHOD.

### 2.1 Implementation of the entropy viscosity method (EVM) with continuous Galerkin finite element method:

After describing the theoretical approach that leads to the derivation of the dissipative terms consistent with the entropy minimum principle and the definition of the viscosity coefficient, this section focuses on the implementation of the method: details are given on how to implement and compute the jump, the entropy residual and the dissipative terms, for instance. Most of the explanation given in this section can be applied to any schemes other than the Galerkin continuous finite element method. Special attention is required for the jump since their definition is scheme dependent. In this section, to explain the steps involved in the implementation of the EVM, we consider a on-uniform 2-D mesh family  $\Omega$ . Each member of this family is called element,  $e$ , and the set of its faces is denoted by  $\delta e = \{\delta e_k\}$ , where  $k$  is the number of faces. To integrate the integral over each element  $e$  and the boundaries  $\delta e$ , a quadrature rule,  $Q = \{q\}$  is used. For the purpose of this section, the EVM is applied to a hyperbolic system of  $n$  equations given in Eq. (2.1).

$$2\partial_t U(\vec{r}, t) + \vec{\nabla} \cdot F(U(\vec{r}, t)) = \vec{\nabla} \cdot G(U(\vec{r}, t)) \quad (2.1)$$

where  $U(\vec{r}, t)$  and  $F(U(\vec{r}, t))$  are the vector conservative variables and the hyperbolic flux, respectively. The term  $G(U(\vec{r}, t))$  denotes the artificial dissipative terms that are assumed consistent with the entropy minimum principle [14]. All of the terms depend on space,  $\vec{r}$  and time,  $t$ . It is also assumed that the eigenvalues,  $\lambda = \{\lambda_1, \lambda_2, \dots, \lambda_n\}$

are known. Lastly, the entropy residual is assumed to be of the following form:

$$\partial_t S(U(\vec{r}, t)) + \vec{\nabla} \Phi(U(\vec{r}, t)) \geq 0 \quad (2.2)$$

where  $S$  is the entropy function and  $\Phi$  is the associated entropy flux.

The first step in the implementation of the EVM is the integration of the dissipative terms over each element of the mesh. The continuous finite element approach consists of multiplying each term by a test function and then, integrating over the volume of each element. Since the dissipative terms are second-order spatial derivatives, an integration per part is performed leading to:

$$\vec{\nabla} \cdot G(U(\vec{r}, t)) \rightarrow \int_e \vec{\nabla} \cdot G(U(\vec{r}, t)) \phi(\vec{r}) = \int_e G(U(\vec{r}, t)) \phi(\vec{r}) - \int_e G(U(\vec{r}, t)) \vec{\nabla} \phi(\vec{r})$$

where  $\phi$  is a test function. Then, each integral is evaluating using the quadrature rule at the set of quadrature points  $\vec{r}_q$ :

$$\int_{\delta e} G(U(\vec{r}, t)) \phi(\vec{r}) - \int_e G(U(\vec{r}, t)) \vec{\nabla} \phi(\vec{r}) = \sum_{q, \delta e} G(U(\vec{r}_q, t)) \phi(\vec{r}_q) - \sum_{q, e} G(U(\vec{r}_q, t)) \vec{\nabla} \phi(\vec{r}_q)$$

The dissipative term  $G(U(\vec{r}, t))$  is function of the viscosity coefficient and the derivative of the conservative variables that need to be evaluated at the quadrature points. Obtaining the derivative values at the quadrature points with a continuous finite element discretization type is straightforward. On the other hand, computing the viscosity coefficient at the same quadrature points require a little bit more of computational work and is explained in the following. Details about the integral over the faces of each element will be given in the next paragraph.

The viscosity coefficient is not obtained by solving a PDE, but simply computed on the fly from the conservative variables. The definition of the viscosity coeffi-

cient  $\mu(\vec{r}, t)$  involves two other viscosity coefficients: a first-order viscosity coefficient  $\mu_{max}(\vec{r}, t)$  that is an upper bound, and a high-order viscosity coefficient often also called entropy viscosity coefficient that is denoted by  $\mu_e(\vec{r}, t)$ . It is assumed that these viscosity coefficients are function of both space and time. The first-order viscosity coefficient is function of the local maximum eigenvalues and the mesh size  $d$ :  $\mu_{max}(\vec{r}, t) = \frac{d}{2} \max \lambda_k(\vec{r}, t)$ . For a shape regular mesh, the mesh size  $d$  is expected to be finite. It is assumed that each element has its own finite mesh size denoted by  $d_e$ . For instance, when using libMesh (REF), a function can be called in order to get the mesh size or diameter of the cell under consideration. Obtaining the local maximum eigenvalue is self explanatory and has to be done for each quadrature point. At this point, in each element,  $q$  different values of the first-order viscosity coefficient is available to us that we denote by the set:  $\mu_{max}^e = \{\mu_{max}(\vec{r}_q, t)\}$ .

The high-order viscosity coefficient is trickier to compute since it involves the entropy residual and the jumps at the interface between cells.

### 3. APPLICATION OF THE ENTROPY VISCOSITY METHOD TO THE MULTI-D EULER EQUATIONS WITH VARIABLE AREA:

#### 3.1 Introduction

Over the past years an increasing interest raised for computational methods that can solve both compressible and incompressible flows. In engineering applications, there is often the need to solve for complex flows where a near incompressible regime or low Mach flow coexists with a supersonic flow domain. For example, such flow are encountered in aerodynamic in the study of airships. In the nuclear industry, flows are nearly the incompressible regime but compressible effects cannot be neglected because of the heat source and thus needs to be accurately resolved.

When solving the multi-D Euler equations for a wide range of Mach numbers, multiple problems have to address: stability, accuracy and acceleration of the convergence in the low Mach regime. Because of the hyperbolic nature of the equations, shocks can form during transonic and supersonic flows, and require the use of the numerical methods in order to stabilize the scheme and correctly resolve the discontinuities. The literature offers a wide range of stabilization methods: flux-limiter [6, 7], pressure-based viscosity method ([30]), Lapidus method ([25, 31, 13]), and the entropy-viscosity method([19, 20]) among others. These numerical methods are usually developed using simple equation of states and tested for transonic and supersonic flows where the disparity between the acoustic waves and the fluid speed is not large since the Mach number is of order one. This approach leads to a well-known accuracy problem in the low Mach regime where the fluid velocity is smaller than the speed of sound by multiple order of magnitude. The numerical dissipative terms become ill-scaled in the low Mach regime and lead to the wrong numerical solution

by changing the nature of the equations solved. This behavior is well documented in the literature [16, 42, 24] and often treated by performing a low Mach asymptotic study of the multi-D Euler equation. This method was originally used [16] to show convergence of the compressible multi-D Euler equations to the incompressible ones. Thus, by using the same method, the effect of the dissipative terms in the low Mach regime, can be understood and, when needed, a fix is developed in order to ensure the convergence of the equations to the correct physical solution. This approach was used as a fixing method for multiple well known stabilization methods alike Roe scheme ([29]) and SUPG [24] while preserving the original stabilization properties of shocks.

We propose, through this paper, to investigate how the entropy viscosity method, when applied to the multi-D Euler equations with variable area, behaves in the low Mach regime. This method was initially introduced by Guermond et al. to solve for the hyperbolic systems and has shown good results when used for solving the multi-D Euler equations with various discretization schemes. More importantly, it is simple to implement, can be used with unstructured grids, and its dissipative terms are consistent with the entropy minimum principle and proven valid for any equation of state under certain conditions [15].

This paper is organized as follows: in Section 3.2 the current definition of the entropy viscosity method is recalled, and inconsistency with the low Mach regime are pointed out. Since our interest is in the variable area version of the multi-D Euler equation, the reader is guided through the steps leading to the derivation of the dissipative terms on the model of [15]. Then in Section 3.3, a new definition of the viscosity coefficient is introduced and derived from a low Mach asymptotic study. After detailing the spatial and temporal discretization method in Section 3.4, 1- and 2-D numerical results are presented in Section 3.5 for a wide range of Mach numbers: low Mach flow

over a cylinder and a circular bump, and supersonic flow in a compression corner [1]. Convergence studies are performed in 1-D, in order to demonstrate the accuracy of the solution.

For purpose of clarity, the multi-D Euler equations with variable area are recalled in Eq. (3.1) and the corresponding variables are defined:

$$\left\{ \begin{array}{l} \partial_t (\rho A) + \vec{\nabla} \cdot (\rho \vec{u} A) = 0 \\ \partial_t (\rho \vec{u} A) + \vec{\nabla} \cdot [(\rho \vec{u} \otimes \vec{u} + P \mathbf{I}) A] = P \vec{\nabla} A \\ \partial_t (\rho E A) + \vec{\nabla} \cdot [\vec{u} (\rho E + P) A] = 0 \\ P = P(\rho, e) \end{array} \right. \quad (3.1)$$

where  $\rho$ ,  $\rho \vec{u}$  and  $\rho E$  are the density, the momentum and the total energy, respectively, and will be referred to as the conservative variables. The pressure  $P$  is computed with an equation of state expressed in function of the density  $\rho$  and the specific internal energy  $e$ . The tensor product  $\vec{a} \otimes \vec{b}$  is taken with the following convention:  $(\vec{a} \otimes \vec{b})_{i,j} = a_i b_j$ . Lastly, the terms  $\partial_t$ ,  $\vec{\nabla}$ ,  $\vec{\nabla} \cdot$  and  $\mathbf{I}$  denote the temporal derivative, the gradient and divergent operators, and the identity tensor, respectively. The variable area  $A$  is assumed spatial dependent.

## 3.2 The Entropy Viscosity Method

### 3.2.1 Background

In this section, the entropy-based viscosity method [19, 20, 14] is recalled for the multi-D Euler equations (with constant area  $A$ ) [43]. The entropy-based viscosity method consists of adding dissipative terms, with a viscosity coefficient modulated by the entropy production which allows high-order accuracy when the solution is smooth. Thus, two questions arise: (i) how are the viscosity dissipative terms derived and (ii) how to numerically compute the entropy production. Answers to the first

question can be found in [15] by Guermond et al., that details the proof leading to the derivation of the artificial dissipative terms (Eq. (3.2)) consistent with the entropy minimum principle theorem. The viscous regularization obtained is valid for any equation of state as long as the opposite of the physical entropy function,  $s$ , is convex with respect to the internal energy  $e$  and the specific volume  $1/\rho$ . As for the entropy production, it is locally evaluated by computing the local entropy residual  $D_e(\vec{x}, t)$  defined in Eq. (3.4), that is known to be peaked in shocks [41].

$$\begin{cases} \partial_t(\rho) + \vec{\nabla} \cdot (\rho \vec{u}) = \vec{\nabla} \cdot (\kappa \vec{\nabla} \rho) \\ \partial_t(\rho \vec{u}) + \vec{\nabla} \cdot (\rho \vec{u} \otimes \vec{u} + P \mathbf{I}) = \vec{\nabla} \cdot (\mu \rho \vec{\nabla}^s \vec{u} + \kappa \vec{u} \otimes \vec{\nabla} \rho) \\ \partial_t(\rho E) + \vec{\nabla} \cdot [\vec{u}(\rho E + P)] = \vec{\nabla} \cdot (\kappa \vec{\nabla}(\rho e) + \frac{1}{2} \|\vec{u}\|^2 \kappa \vec{\nabla} \rho + \rho \mu \vec{u} \vec{\nabla} \vec{u}) \\ P = P(\rho, e) \end{cases} \quad (3.2)$$

where  $\kappa$  and  $\mu$  are local positive viscosity coefficients.  $\vec{\nabla}^s \vec{u}$  denotes the symmetric gradient operator that guarantees the method to be rotational invariant [15].

In the current version of the method,  $\kappa$  and  $\mu$  are set equal, so that the above viscous regularization (Eq. (3.2)) is equivalent to the parabolic regularization [2] when considering the 1-D form of the equation. The current definition includes a first-order viscosity coefficient referred to with the subscript *max*, and a high-order viscosity coefficient referred to with the subscript *e*. The first-order viscosity coefficients  $\mu_{max}$  and  $\kappa_{max}$  are proportional to the local largest eigenvalue  $\|\vec{u}\| + c$  and equivalent to an upwind-scheme (see Eq. (3.3)), when used, which is known to be over-dissipative and monotone [41]:

$$\mu_{max}(\vec{r}, t) = \kappa_{max}(\vec{r}, t) = \frac{h}{2} (\|\vec{u}\| + c), \quad (3.3)$$

where  $h$  is defined as the ratio of the grid size to the polynomial order of the test functions used.

The second-order viscosity coefficients  $\kappa_e$  and  $\mu_e$  are set proportional to the entropy production that is evaluated by computing the local entropy residual  $D_e$ . It also includes the interfacial jump of the entropy flux  $J$  that will allow to detect any discontinuities other than shocks:

$$\mu_e(\vec{r}, t) = \kappa_e(\vec{r}, t) = h^2 \frac{\max(|D_e(\vec{r}, t)|, J)}{\|s - \bar{s}\|_\infty} \quad \text{with } D_e(\vec{r}, t) = \partial_t s + \vec{u} \cdot \vec{\nabla} s \quad (3.4)$$

where  $\|\cdot\|_\infty$  and  $\bar{\cdot}$  denote the infinite norm operator and the average operator over the entire computational domain, respectively. The definition of the jump  $J$  is discretization-dependent and examples of definition can be found in [43] for DGFEM. The denominator  $\|s - \bar{s}\|_\infty$  is used for dimensionality purposes and should not be of the same order as  $h$ , on penalty of loosing the high-order accuracy. Currently, there are no theoretical justification for choosing the denominator.

The definition of the viscosity coefficients  $\mu$  and  $\kappa$  is function of the first- and second-order viscosity coefficients as follows:

$$\mu(\vec{r}, t) = \min(\mu_e(\vec{r}, t), \mu_{max}(\vec{r}, t)) \quad \text{and} \quad \kappa(\vec{r}, t) = \min(\kappa_e(\vec{r}, t), \kappa_{max}(\vec{r}, t)). \quad (3.5)$$

This definition allows the following properties. In shock regions, the second-order viscosity coefficient experiences a peak because of entropy production, and thus, saturates to the first-order viscosity that is known to be over-dissipative and will smooth out oscillations. Anywhere else, the entropy production being small, the viscosity coefficients  $\mu$  and  $\kappa$  are of order  $h^2$ .

Using the above definition of the entropy-based viscosity method, high-order accu-



racy was demonstrated and excellent results were obtained with 1-D Sod shock tubes and various 2-D tests [19, 20, 43].

### 3.2.2 *Issues in the Low-Mach Regime*

In the Low-Mach Regime, the flow is known to be isentropic resulting in very little entropy production. Since the entropy viscosity method is directly based on the evaluation of the local entropy production, it will be interested to study how the entropy viscosity coefficients  $\mu$  and  $\kappa$  scale in the low Mach regime. Mathematically, it means that the entropy residual  $D_e$  will be very small, so will be the denominator  $\|s - \bar{s}\|_\infty$ , thus making the ratio, used in the definition of the viscosity coefficients Eq. (3.4), undetermined. Therefore, the current definition of the viscosity coefficients seems unadapted to subsonic flow and could lead to ill-scaled dissipative terms. A solution would be to recast the entropy residual as a function of other variables in order to have more freedom in the choice of the normalization parameter. With this approach, the viscosity coefficients are still defined proportional to the entropy residual that is a good indicator of the flow type (subsonic, transonic and supersonic flow). Plus, a different normalization parameter could be chosen, based on a low Mach asymptotic study so that the viscosity coefficients are well-scaled in the low Mach asymptotic limit (see Section 3.3).

### 3.2.3 *The dissipative-terms for the multi-D Euler equations with variable area*

One of the focus of this paper is to investigate the application of the entropy viscosity method to the multi-D Euler equations with variable area. The variable area version of the Euler equations is mostly used in 1-D and 2-D for obvious reasons, and differs from Eq. (3.1) by the momentum equation as shown in Eq. (3.6), that contains a non-conservative term proportional to the area gradient. For the purpose of this paper, the variable area is assumed to be a smooth function and only spatial

dependent. An example can be found in [37] where a fluid flows through a 1-D convergent-divergent nozzle and reaches a steady-state solution.

$$\begin{cases} \partial_t (\rho A) + \vec{\nabla} \cdot (\rho \vec{u} A) = 0 \\ \partial_t (\rho \vec{u} A) + \vec{\nabla} \cdot [A (\rho \vec{u} \otimes \vec{u} + P \mathbf{I})] = P \vec{\nabla} A \\ \partial_t (\rho E) + \vec{\nabla} \cdot [\vec{u} (\rho E + P)] = 0 \end{cases} \quad (3.6)$$

The application of the entropy viscosity method to the above system of equations is expected to be straightforward since it degenerates to the Eq. (3.1) when assuming a constant area. Details of the derivations of the dissipative terms are available to the reader in Appendix ?? and are very similar to what was done in [15]. An entropy residual is derived without the dissipative terms. Then, the same entropy residual is re-derived after adding dissipative terms to each equation of the system given in Eq. (3.6), and the entropy minimum principle is used as a condition to obtain a definition for each of the dissipative terms. The final result including the dissipative terms is given in Eq. (3.7):

$$\begin{cases} \partial_t (\rho A) + \vec{\nabla} \cdot (\rho \vec{u} A) = \vec{\nabla} \cdot (A \kappa \vec{\nabla} \rho) \\ \partial_t (\rho \vec{u} A) + \vec{\nabla} \cdot [A (\rho \vec{u} \otimes \vec{u} + P \mathbf{I})] = P \vec{\nabla} A + \vec{\nabla} \cdot \left[ A \left( \mu \rho \vec{\nabla}^s \vec{u} + \kappa \vec{u} \otimes \vec{\nabla} \rho \right) \right] \\ \partial_t (\rho E) + \vec{\nabla} \cdot [\vec{u} (\rho E + P)] = \vec{\nabla} \cdot \left[ A \left( \kappa \vec{\nabla} (\rho e) + \frac{1}{2} \|\vec{u}\|^2 \kappa \vec{\nabla} \rho + \rho \mu \vec{u} \vec{\nabla} \vec{u} \right) \right] \end{cases} \quad (3.7)$$

The dissipative terms are very similar to the ones obtained for the multi-D Euler equations: each dissipative flux is multiplied by the variable area  $A$  in order to ensure conservation of the flux. When assuming a constant area, Eq. (3.2) is retrieved. The definition of the viscosity coefficients  $\mu$  and  $\kappa$  is explained in Section 3.3.2.

### 3.3 All-speed Reformulation of the Entropy Viscosity Method

In this section, the entropy residual  $D_e$  is recast as a function of the pressure, the density and the speed of sound. Then, a low Mach asymptotic study of the multi-D Euler equations is performed in order to derive the correct normalization parameter.

#### 3.3.1 New Entropy Production Residual

The first step in defining a viscosity coefficient that behaves well in the low mach limit is to recast the entropy residual in terms of the thermodynamic variables as shown in Eq. (3.8):

$$D_e(\vec{r}, t) = \partial_t s + \vec{u} \cdot \vec{\nabla} s = \frac{s_e}{P_e} \left( \underbrace{\frac{dP}{dt} - c^2 \frac{d\rho}{dt}}_{\tilde{D}_e(\vec{r}, t)} \right), \quad (3.8)$$

where  $\frac{d}{dt}$  denotes the material or total derivative, and  $P_e$  is the partial derivative of pressure with respect to internal energy. The steps that lead to the new formulation of the entropy residual  $D_e$  can be found in Appendix ??.

The entropy residual  $D_e$  and  $\tilde{D}_e$  are proportional to each other and therefore will experience the same variation when taking the absolute value. Thus, locally evaluating  $\tilde{D}_e$  instead of  $D_e$  should allow us to measure the entropy production point wise. This new expression given in Eq. (3.8) has multiple advantages:

- an analytical expression of the entropy function is not longer needed: the entropy residual  $\tilde{D}_e$  is evaluated using the local values of the pressure, the density and the speed of sound. Deriving an entropy function for some complex equation of states can be difficult.
- with the proposed expression of the entropy residual function of pressure and

density, additional normalizations suitable for low Mach flows of the entropy residual can be devised. Examples include the pressure itself, or combination of the density, the speed of sound and the norm of the velocity:  $\rho c^2$ ,  $\rho c||\vec{u}||$  and  $\rho||\vec{u}||^2$ .

The viscosity coefficients  $\mu$  and  $\kappa$  are now defined proportional to the new entropy residual  $\tilde{D}_e$  on the model of Eq. (3.4) as follows:

$$\mu(\vec{r}, t) = \kappa(\vec{r}, t) = h^2 \frac{\max(\tilde{D}_e, J)}{n(P)} \quad (3.9)$$

where  $n(P)$  is a normalization parameter to determine and all other variables were defined previously.

As mentioned earlier, the normalization parameter  $n(P)$  must be of the same units as the pressure for the viscosity coefficients to have the unit of a dynamic viscosity ( $m^2/s$ ). Multiples options are available to us:  $P$ ,  $\rho c^2$ ,  $\rho c||\vec{u}||$  and  $\rho||\vec{u}||^2$ . The choice of the normalization parameter cannot be random if the definition of the viscosity coefficient is wanted to be well-scaled for a wide range of Mach numbers. For example, by choosing  $n(P) = \rho||\vec{u}||^2$ , the viscosity coefficient will become very large as the Mach number decreases which would be unnecessary since the equations will not develop any shock or discontinuity. Therefore, it is proposed to carry, in Section 3.3.2, a low-Mach asymptotic study of the multi-D Euler equations in order to determine the correct expression for the normalization parameter  $n(P)$ .

### 3.3.2 Low-Mach asymptotic study of the multi-D Euler equations

The asymptotic study requires the multi-D Euler equations to be non dimensionalized: the objective is to make the Mach number appears and thus, use a polynomial expansion of the variables as a function of the Mach number in order to derive the

leading, first- and second-order equations. Before detailing the steps of the asymptotic method, let us have a closer look at the system of equations under consideration. The initial system of equations is composed of the multi-D Euler equations. For stability purpose, artificial dissipative terms are added to each equation as explained in Section 3.2. The resulting system of equations is alike the multi-D Navier-Stokes equations in a sense that it contains second-order derivative terms. Thus, it would be interesting to look at the steps employed in the asymptotic study of the multi-D Navier-Stokes equations in order to understand how the dissipative terms are treated. Fortunately, this process is well-documented in the literature [16, 42, 24] for both multi-D Euler equations and Navier-Stokes equations. The work presented here is mainly inspired of [34] that focuses on the asymptotic study in the low Mach regime of Navier-Stokes equations. During the derivation, the reader has to keep in mind that the objective of this section is to derive a normalization parameter for the definition of the viscosity coefficients so that the multi-D Euler equations degenerate to the incompressible system of equations, which implies that the dissipative terms are well-scaled. The main steps of the derivation are presented in the following of this section:

To express Eq. (3.2) in dimensionless variables, the following dimensional variables are introduced:

$$\begin{aligned} \rho &= \frac{\rho^*}{\rho_\infty}, P = \frac{P^*}{\rho_\infty c_\infty^2}, \mu = \frac{\mu^*}{\mu_\infty}, E = \frac{E^*}{c_\infty^2}, \mu = \frac{\mu^*}{\mu_\infty}, \\ \kappa &= \frac{\kappa^*}{\kappa_\infty}, x = \frac{x^*}{L_\infty}, t = \frac{t^*}{L_\infty/u_\infty}, u = \frac{u^*}{u_\infty} \end{aligned} \quad (3.10)$$

where the subscript  $\infty$  and the upper script  $*$  denote the far field or stagnation quantities and the dimensionless variables, respectively. The reference quantities are chosen such that the non dimensional flow quantities are of order one for any low

reference-Mach number

$$M_\infty = \frac{u_\infty^*}{c_\infty^*} \quad (3.11)$$

where  $c_\infty^*$  is a reference value for the speed of sound.

Then, using the non dimensional quantities and the multi-D Euler equations from Eq. (3.2) , the following non dimensional form is obtained:

$$\left\{ \begin{array}{l} \partial_t \rho + \nabla \cdot (\rho \vec{u}) = \frac{1}{Re_\infty Pr_\infty} \nabla \cdot (\kappa \nabla \rho) \\ \partial_t (\rho \vec{u}) + \nabla \cdot (\rho \vec{u} \otimes \vec{u}) + \frac{1}{M_\infty^2} \nabla (P) = \frac{1}{Re_\infty} \nabla \cdot (\rho \mu \nabla \vec{u}) + \frac{1}{Re_\infty Pr_\infty} \nabla \cdot (\vec{u} \otimes \kappa \nabla \rho) \\ \partial_t (\rho E) + \nabla \cdot [\vec{u} (\rho E + P)] = \frac{1}{Re_\infty Pr_\infty} \nabla \cdot (\kappa \nabla (\rho e)) + \frac{\tilde{M}_\infty^2}{Re_\infty} \nabla \cdot (\vec{u} \rho \mu \nabla \vec{u}) \\ + \frac{M_\infty^2}{2 Re_\infty Pr_\infty} \nabla \cdot (\kappa u^2 \nabla \rho) \\ P = (\gamma - 1) (\rho E + M_\infty^2 \rho u^2) \end{array} \right.$$

where the *numerical* Reynolds ( $Re_\infty$ ) and Prandtl ( $Pr_\infty$ ) numbers are defined as follows:

$$Re_\infty = \frac{u_\infty L_\infty}{\mu_\infty} \text{ and } Pr_\infty = \frac{\mu_\infty}{\kappa_\infty}. \quad (3.12)$$

Since it is chosen to have the same definition for both  $\mu$  and  $\kappa$  the numerical Prandtl number is unconditionally equal to one:  $Pr_\infty = 1$ .

Once the dimensionless equations are obtained, the next step consists of expanding each variable in term of the Mach number (example given in Eq. (3.13) for the pressure  $P$ ) in order to derive the leading, first- and second-order equations.

$$P(\vec{r}, t) = P_0(\vec{r}, t) + P_1(\vec{r}, t)M_\infty + P_2(\vec{r}, t)M_\infty^2 + \dots \text{ with } M_\infty \rightarrow 0 \quad (3.13)$$

Before deriving the leading-order equation, a choice needs to be made on how the numerical Reynolds number scales. Multiple options are available to us and a few

example are given:  $Re_\infty = M_\infty$ , or  $Re_\infty = M_\infty^{-1}$  or  $Re_\infty = 1$ . Let us assume for academy purpose that the numerical Reynolds number scales as the inverse of the Mach number square:  $Re_\infty = M_\infty^{-2}$ . The best way to evaluate the impact of this choice on the equations, is to look at the momentum equation and try to derive the order  $M_\infty^{-2}$ :

$$\vec{\nabla} P_0 = \vec{\nabla} \cdot (\rho_0 \mu_0 \vec{\nabla} \vec{u}_0 + \vec{u}_0 \otimes \vec{\nabla} \rho_0) \quad (3.14)$$

which is known to be ([24])

$$\vec{\nabla} P_0 = 0 \quad (3.15)$$

It is clear that Eq. (3.14) and Eq. (3.15) will not yield the same result. The same conclusion is drawn when deriving the order  $M_\infty^{-1}$  of the momentum equation, making our initial assumption not suitable. From the above result, it is understood that the numerical Reynolds number has to scale as one so that it does not affect the orders  $M_\infty^{-2}$  and  $M_\infty^{-1}$  of the momentum equations:  $Re_\infty = 1$ . Thus, with such assumption, Eq. (3.12) implies:

At order  $M_\infty^{-2}$ :

$$\vec{\nabla} P_0 = 0$$

At order  $M_\infty^{-1}$ :

$$\vec{\nabla} P_1 = 0$$

At leading-order:

$$\begin{aligned} \partial_t \rho_0 + \vec{\nabla} \cdot (\rho_0 \vec{u}_0) &= \vec{\nabla} \cdot (\kappa_0 \vec{\nabla} \rho_0) \\ \partial_t (\rho_0 \vec{u}_0) + \vec{\nabla} \cdot (\rho_0 \vec{u}_0 \otimes \vec{u}_0) + \vec{\nabla} P_2 &= \vec{\nabla} \cdot (\rho_0 \mu_0 \vec{\nabla} \vec{u}_0 + \vec{u}_0 \otimes \vec{\nabla} \rho_0) \\ \partial_t (\rho_0 E_0) + \vec{\nabla} \cdot [\vec{u}_0 (\rho_0 E_0 + P_0)] &= \vec{\nabla} \cdot (\kappa_0 \vec{\nabla} (\rho_0 e_0)) \end{aligned}$$

Under this form, the dissipative terms only affect the leading-order equations in the asymptotic limit.

It is now determined that the numerical Reynolds number  $Re_\infty$  has to scale as one. Following Eq. (3.12),  $Re_\infty$  is a function of the  $\mu_\infty$ , and thus  $n_P$ . It can be shown using Eq. (3.10) and the definitions of  $\tilde{D}$  given in Eq. (3.8) that:

$$\mu_\infty = \frac{\rho_\infty c_\infty^2 u_\infty L}{n_{P,\infty}} \quad (3.16)$$

where  $n_{P,\infty}$  is the far-field quantity for the normalization parameter  $n_P$ . Substituting Eq. (3.16) into Eq. (3.12) and remembering that the numerical Reynolds number scales as one, it yields:

$$n_{P,\infty} = \rho_\infty c_\infty^2 \quad (3.17)$$

Eq. (3.17) tells us that in the asymptotic limit, the normalization parameter  $n_P$  scales as  $\rho_\infty c_\infty^2$  which leaves us with two options: either  $n_P = \rho c^2$  or  $n_P = P$ . The choice was made to use  $n_P = \rho c^2$  in the asymptotic limit: it was found to behave well and the pressure can become locally negative and null in some particular case as shown in Section 3.5. This normalization parameter is only valid in the asymptotic limit and the purpose of this paper is to define a viscosity coefficient  $\mu$  that is valid for a wide range of Mach numbers. Thus, it is proposed to define the high-order viscosity coefficient  $\mu_e$  as follows:

$$\mu_e = h^2 \frac{\max(\tilde{D}_e, J)}{(1 - f(M))\rho c^2 + f(M)\rho||\vec{u}||^2} \quad (3.18)$$



where  $f(M)$  is a function of the local Mach number  $M$  with the following properties:

$$\begin{cases} f(M) \rightarrow 0 \text{ as } M \rightarrow 0 \\ f(M) \rightarrow 1 \text{ as } M \geq 1 \end{cases} \quad (3.19)$$

The choice of the function  $f(M)$  is not fixed and a few examples are available in the literature. A simple definition is  $f(M) = \min(M, 1)$  which meets the conditions of Eq. (3.19). Another definition for  $f(M)$  was proposed by [29]. All of the numerical results presented in Section 3.5 were obtained by using  $f(M) = \min(M, 1)$  which is simple to implement. A convergence test for a subsonic flow over a 2-D cylinder will show that this definition of  $f(M)$  yields the correct behavior in the asymptotic limit. The definition of the high-order viscosity coefficient  $\mu_e(\vec{r}, t)$  should behave well for complex flow where a near incompressible regime coexists with a supersonic flow domain since  $f(M)$  is function of the local Mach number.

For clarity purpose, the full definition of the viscosity coefficient  $\mu(\vec{r}, t)$  is recalled:

$$\begin{cases} \mu(\vec{r}, t) = \max(\mu_{max}(\vec{r}, t), \mu_e(\vec{r}, t)) \\ \text{where } \mu_{max}(\vec{r}, t) = \frac{h}{2}(|\vec{u}| + c) \\ \text{and } \mu_e(\vec{r}, t) = h^2 \frac{\max(\tilde{D}_e, J)}{(1-f(M))\rho c^2 + f(M)\rho|\vec{u}|^2} \\ \mu(\vec{r}, t) = \kappa(\vec{r}, t) \end{cases} \quad (3.20)$$

These viscosity coefficients are valid for both the multi-D Euler equations with variable and constant area and are employed with the dissipative terms detailed in Eq. (3.12). The reader will notice that, through the derivation, none assumption was made on the type of equation of state besides the convexity condition on the entropy function  $s$ . The remaining of this paper (Section 3.5) will focus on demonstrating that the definition of the viscosity coefficient given in Eq. (3.20) is indeed

well-scaled in the asymptotic limit and that shocks are still well resolved.

### 3.4 Solution Techniques Spatial and Temporal Discretizations

In order to detail the partial and temporal discretization used for this study, the system of equations Eq. (3.7) is considered under the following form for simplicity:

$$\partial_t U + \vec{\nabla} \cdot F(U) = S \quad (3.21)$$

where  $U$  is the vector solution,  $F$  is a conservative vector flux and  $S$  is a vector source that can contain the non-conservative term  $P\vec{\nabla}A$ .

#### 3.4.1 Spatial and Temporal Discretizations

The system of equation given in Eq. (5.15) is discretized using a continuous Galerkin finite element method and high-order temporal integrators provided by the MOOSE framework.

##### 3.4.1.1 CFEM

In order to apply the continuous finite element method, Eq. (5.15) is multiplied by a smooth test function  $\phi$ , integrated by part and each integral is split onto each finite element  $e$  of the discrete mesh  $\Omega$  bounded by  $\partial\Omega$ , to obtain a weak solution:

$$\sum_e \int_e \partial_t U \phi - \sum_e \int_e F(U) \cdot \vec{\nabla} \phi + \int_{\partial\Omega} F(U) \vec{n} \phi - \sum_e \int_e S \phi = 0 \quad (3.22)$$

The integrals over the elements  $e$  are evaluated using quadrature-point rules. The Moose framework provides a wide range of test function and quadrature rules: trapezoidal and Gauss rules among others. Linear Lagrange polynomials will be used as test functions and should ensure second-order convergence for smooth functions. The order of convergence will be demonstrated.

### 3.4.1.2 Temporal integrator

The MOOSE framework offers both first- and second-order explicit and implicit temporal integrators. In all of the numerical examples presented in Section 3.5, the time-dependent term  $\int_e \partial_t U \phi$  will be evaluated using the second-order temporal integrator BDF2. By considering three solutions,  $U^{n-1}$ ,  $U^n$  and  $U^{n+1}$  at three different time  $t^{n-1}$ ,  $t^n$  and  $t^{n+1}$ , respectively, it yields:

$$\begin{aligned} \int_e \partial_t U \phi &= \int_e (\omega_0 U^{n+1} + \omega_1 U^n + \omega_2 U^{n-1}) \phi \\ \text{with } \omega_0 &= \frac{2\Delta t^{n+1} + \Delta t^n}{\Delta t^{n+1} (\Delta t^{n+1} + \Delta t^n)}, \\ \omega_1 &= -\frac{\Delta t^{n+1} + \Delta t^n}{\Delta t^{n+1} \Delta t^n} \\ \text{and } \omega_2 &= \frac{\Delta t^{n+1}}{\Delta t^n (\Delta t^{n+1} + \Delta t^n)} \end{aligned} \tag{3.23}$$

where  $\Delta t^n = t^n - t^{n-1}$  and  $\Delta t^{n+1} = t^{n+1} - t^n$ .

### 3.4.2 Boundary conditions

Because we cannot consider infinitely large domain, the computational domain needs to be truncated at some particular points. These particular points are referred to as boundaries and need to be treated with great care in order to preserve the mathematical and physical properties of the equations to solve. An error in the treatment of the boundary conditions can lead to inaccurate transient and steady-state numerical solutions. The conditions applied to the boundaries of the computational domain are called boundary conditions and correspond to a set of boundary values to supply and relations that will link the boundary values to the rest of the computational domain. When dealing with wave-dominated problem alike the multi-D Euler equations, the eigenvalues and the characteristic equations are of great help since

they inform us on how the physical information travel through the computational domain. A great amount of work on the treatment of the inlet and outlet boundary conditions is available in the literature (REFS). The method proposed depend on the equation of state and the discretization method. For discontinuous schemes alike finite volume and discontinuous Galerkin method, providing some boundary values, a Riemann problem is often solved. A Riemann solver is derived from the study of the eigenvalues and characteristic equations, and therefore will preserve the balance of the system, but is strongly dependent on the equation of state used. In the case of continuous schemes, the same approach cannot be used since the variables are continuous at the interfaces. Instead a more direct approach is required and is the focus of this section.

This short paragraph aims at illustrating the reasoning behind the treatment of the boundary conditions. For academic purpose, let us consider a 1-D computational domain with a left inlet and right outlet boundaries. The 1-D characteristic equations and the eigenvalues for the multi-D Euler equations are recalled:

$$\left\{ \begin{array}{l} dP - \rho c du = 0 \text{ along } \frac{dx}{dt} = u - c = \lambda_1 \\ d\rho + \text{ along } \frac{dx}{dt} = u = \lambda_2 \\ dP + \rho c du = 0 \text{ along } \frac{dx}{dt} = u + c = \lambda_3 \end{array} \right. \quad (3.24)$$

The 1-D characteristic equations can be derived by either performing matrix calculations or by combining the conservative form of the 1-D Euler equations. These two approach are equivalent and lead to the same form of the characteristic equations given in Eq. (3.24). The three eigenvalues  $\lambda_i$  in 1-D are also recalled in Eq. (3.24). We are focusing on the inlet boundary. The sign of the eigenvalues at the inlet given in Eq. (3.24) will depend on the flow type: either supersonic with a Mach number

larger than one and all eigenvalues are positive, or subsonic with a Mach number smaller than one and  $\lambda_2$  and  $\lambda_3$  are positive but  $\lambda_1$  is negative. More specifically, for a supersonic flow, none physical information exits the computational domain. In another hand, for a subsonic flow, waves are both exiting and entering the computational domain at the inlet. From a numerical point of view, it means that in the case of a supersonic flow, all of the quantities need to be supplied to the code. When dealing with a subsonic flow, only two variables will be supplied and the third one will be computed using relations derived from the characteristic equations. From this simple study of the sign of the eigenvalues, it is understood that a distinction between supersonic and subsonic needs to be made in order to properly evaluate the boundary values. A similar approach can be used for the treatment of the outlet boundary.

In this section, four types of boundary conditions will be described: static pressure, stagnation pressure, mass inflow and wall boundary conditions. For each of them, details regarding the theory in 1-D and the implementations for a temporal implicit solver described in Section 3.4.1.2 will be given. The characteristic equations and eigenvalues are independent of the equation of states. However, derivation of the relations to implement for the subsonic and supersonic boundary conditions will depend on the equation of state: the Stiffened Gas equation of state is considered here. The method used here is partly derived from the work of Berry et al. [37] that was applied to the two-phase flow seven equations model solved with a temporal explicit solver. It is also chosen to work with the primitive variables (density  $\rho^*$ , velocity  $u^*$  and pressure  $P^*$ ) that are computed at the boundaries using relations that will depend on the boundary type. The upper script  $*$  denotes the values on the element located at the boundary (node, curve and face in 1, 2 and 3-D, respectively). From a numerical point of view, the boundary terms are under the form of an integral

over the surface  $\int_{\partial\Omega} F(U^*) \vec{n} \phi$  as shown in Eq. (3.22). For each type of boundary conditions, it is explained how to compute the primitive variables at the boundary: then the hyperbolic flux  $F(U^*)$  is easily obtained.

### 3.4.3 Stagnation pressure boundary condition

The stagnation pressure boundary condition is used whenever a pipe is connected to a very large tank or reservoir. The tank is so large in comparison to the pipe that the flow coming from the tank is considered to be at quasi-steady-state. This boundary condition assumes a subsonic flow: two eigenvalues are positive and one is negative. Physically it means that information exits and enters the computational domain at the inlet boundary. In order to be consistent with the physic, two boundary values have to be provided and the third one needs to be obtained from the computational domain. The stagnation pressure and temperature are usually supplied for this type of boundary. A general definition for a stagnation pressure is the following: *the stagnation pressure is the static pressure a flow retain when brought to rest isentropically from a given fluid state*. For incompressible flow, the stagnation pressure is simply the sum of the static pressure and the kinetic energy. When brought to rest, all of the kinetic energy is converted into internal energy that is function of the static pressure. For compressible flow described by the Stiffened gas equation of state, the stagnation pressure and temperature are function of the Mach number  $M$  as follows:

$$P_0 = P_s \left( 1 + \frac{\gamma - 1}{2} M^2 \right) \quad (3.25)$$

$$T_0 = T_s \left( 1 + \frac{\gamma - 1}{2} M^2 \right)^{\frac{\gamma - 1}{\gamma}} \quad (3.26)$$

where  $P_s$  and  $T_s$  denote the static pressure and temperature respectively. The stagnation relations given in Eq. (3.25) are derived by assuming an isentropic flow. From the stagnation pressure and temperature, the stagnation density and enthalpy can be computed using the equation of state. The sub script 0 is used to denote any stagnation variable.

We now need to find out how to compute the primitive variables in order to get the flux  $F(U^*)$  at the boundary. For a temporal explicit scheme and a finite volume discretization method, Berry et al. [37] used the characteristic equations and the isentropic assumption along with the definition of the stagnation variables to derive relations that relate the boundary node values to the middle-point value of the first cell in. A non-linear equation, obtained from the integration of the characteristic equations over the first cell in, has to be solved to get the boundary velocity value. This typical finite volume approach is not easily adaptable to a continuous finite element method since the cell values are not constant. The method to compute and implement the boundary conditions detailed in this section, takes advantage of the non-linear solver that is used to solve each implicit time step. First, relations that link the pressure  $P^*$  and the density  $\rho^*$  to the velocity  $u^*$  are derived by using enthalpy and entropy conservation through the boundary. In order to derive analytical expression for the entropy, an equation of state is required. As mentioned earlier in this section, the Stiffened Gas equation of state is used to describe the fluid. Derivation of the analytical expression for the entropy  $S$  can be found in (REF) and lead to the following expression:

$$S(\rho, P) = C_v \log \frac{P + P_\infty}{\rho^\gamma}$$

where  $C_v$  is a constant heat capacity. Since the flow is assumed to be isentropic at the boundary, the following relation can be used:

$$S_0 = S^* \rightarrow \frac{P_0 + P_\infty}{\rho_0^\gamma} = \frac{P^* + P_\infty}{\rho^{*\gamma}} = K$$

which can be recast under the flooding form to obtain our first relation:

$$P^* = K\rho^{*\gamma} - P_\infty \quad (3.27)$$

where  $K$  is computed from the stagnation pressure and temperature, and using the equation of state to obtain the stagnation density. The second relation is obtained by using an enthalpy balance between the boundary and a far field location in the tank. The enthalpy is denoted by  $H$  and defined as  $H = E + p/\rho$ . Thus,

$$H_0 = H^* \rightarrow \bar{H} = \frac{\gamma(P_0 + P_\infty)}{\rho_0(\gamma - 1)} = \frac{\gamma(P^* + P_\infty)}{\rho^*(\gamma - 1)} + \frac{1}{2}u^{*2}$$

after splitting the total energy in the sum of the internal and kinetic energy and using the Stiffened Gas equation of state to express the internal energy as a function of the pressure and the density. The constant  $\bar{H}$  is again computed from the stagnation variables. Using Eq. (3.27), the second relation for the density  $\rho^*$  only function of the velocity  $u^*$  is obtained:

$$\rho^* = \left( \frac{\gamma - 1}{K\gamma} \left( \bar{H} - \frac{u^{*2}}{2} \right) \right)^{\frac{1}{\gamma-1}} \quad (3.28)$$

From Eq. (3.27) and Eq. (3.28), once a value for the velocity  $u^*$  is known, the pressure and the density values at the boundary can be computed. In [37], the velocity at the boundary is computed from a non-linear equation that is obtained



by integrating the characteristic equations over the first cell in. The objective is to link the inside of the computational domain to the boundary in order to transmit the proper physical information entering and exiting the boundary. Our approach differs from [37] in a sense that it takes advantage of the non-linear solver used to solve for the numerical solution at each implicit time step. While iterating on the solution to converge the residual, a direct connection between the boundary values and the rest of the computational domain is ensured. Thus, it is believed that the non-linear function to compute the velocity used in [37] is not required and the connection between the boundary and the rest of the domain will be simply ensured by taking the latest value of the velocity  $u_k^*$  given by the non-linear solver, where  $k$  denotes the  $k^{th}$  iterate. Thus, given the last iterate of the velocity value at the boundary  $u_k^*$ , the corresponding pressure  $p_k^*$  and density  $\rho_k^*$  values can be computed from Eq. (3.27) and Eq. (3.28). During a non-linear solve, the velocity gets updated based on the inside values and so are the pressure and density. The boundary values are converged once the residual of the full computational domain is converged. From the star primitive values  $U^* = \{\rho^*, u^*, P^*\}$ , the flux  $F(U^*)$  can be computed and then used to weakly impose the boundary in Eq. (3.22). It is also possible to strongly impose the boundary conditions by computing the conservative variables from the star primitive values and using Dirichlet method (REF).

**Remark.** *For the stagnation pressure boundary condition, it can be also chosen to specify the stagnation density instead of the stagnation temperature. Using the equation of state, the third value can be easily obtained.*

#### 3.4.4 Back pressure outlet boundary condition for subsonic flow

The back pressure boundary condition is applied when a flow exits a computational domain and has to match a specified back pressure at the exit. This type

of boundary condition is only valid for subsonic flow (outlet boundary condition for supersonic flow is treated in Section 3.4.6). This boundary condition is often referred in the literature as a static pressure outlet boundary condition. We rather use this terminology for the static pressure inlet boundary.

Once again, the basis of the method relies on the sign of the eigenvalues. A subsonic flow at the outlet is considered: the eigenvalues  $\lambda_2$  and  $\lambda_3$  are positive and the eigenvalue  $\lambda_1$  is negative. Therefore, only one variable needs to be specified in order to be consistent with the mathematical properties of the system of equations: this variable is the back pressure  $P_b$ . For an explicit temporal discretization, alike in [37], the characteristic equations associated to the eigenvalues  $\lambda_2$  and  $\lambda_3$  are used to compute the values of the density and the velocity at the outlet: the characteristic equations are integrated over the last cell and a relation linking the star values to the first node-in values is obtained. In the case of an implicit temporal discretization, the non-linear solver substitutes itself to the characteristic equations. The values of the density  $\rho^*$  and the velocity  $u^*$  are updated through the iterations and , thus are related to the rest of the computational domain. Every time the pressure is required, it is set equal to the back pressure  $P_b$ . When considering the  $k^{th}$  iteration, the 1-D flux at the boundary looks like:

$$F(U_k^*) = \begin{cases} \rho_k^* u_k^* \\ \rho_k^* (u_k^*)^2 + P_b \\ u_k^* (\rho_k^* E_k^* + P_b) \end{cases} \quad (3.29)$$

where  $E_k^*$  is computed using the equation of state and the values  $\rho_k^*$ ,  $u_k^*$  and  $P_b$ .

#### 3.4.5 Mass flow inlet boundary condition

#### 3.4.6 Outlet boundary condition for supersonic flow

A supersonic boundary condition is required when the flow becomes supersonic at the outlet. In that case, all of the eigenvalues are locally positive which means all of the physical information exits the computational domain. Then, the primitive values at the boundary are all taken equal to the last iterate ones and used to compute the flux at the boundary as follows:

$$F(U_k^*) = \begin{cases} \rho_k^* u_k^* \\ \rho_k^* (u_k^*)^2 + P_k^* \\ u_k^* (\rho_k^* E_k^* + P_k^*) \end{cases} \quad (3.30)$$

where  $E_k^*$  is computed using the equation of state and the values  $\rho_k^*$ ,  $u_k^*$  and  $P_k^*$ .

The outlet supersonic boundary condition is often paired to the back pressure outlet boundary condition described in Section 3.4.4. When implementing an outlet boundary condition a switch statement on the Mach number is required in order to account for flow going from subsonic to supersonic or the other way around. The only major difference between the two types of boundary condition is the treatment of the pressure.

#### 3.4.7 Solver

A Free-Jacobian-Newton-Krylov (FJNK) method is used to solve for the solution at each time step. The jacobian matrix of the discretized equations was derived by hand, hard coded and used as a preconditioner. This method requires the partial derivative of the pressure with respect to the conservative variables to be known. The contribution of the artificial dissipative terms to the jacobian matrix is simplified by

assuming constant viscosity coefficients as shown in Eq. (3.31) for the dissipative terms of the continuity equation:

$$\frac{\partial}{\partial U_i} \left( \kappa \vec{\nabla} \rho \vec{\nabla} \phi \right) = \kappa \frac{\partial}{\partial U_i} (\rho) \vec{\nabla} \phi \quad (3.31)$$

where  $U_i$  denotes the set of conservative variables.

### 3.5 1-D shock tubes:

This section is dedicated to presenting 1- and 2-D numerical results obtained by solving Eq. (3.7) with the entropy viscosity method. This section has two objectives: validate our new definition of the viscosity coefficients for the low Mach limit, and, make sure that the new definition can still resolve shocks.

The first set of 1-D simulations consist of liquid water and steam flowing in a convergent-divergent nozzle. This test is interesting for multiple reasons: a steady-state is reached (some stabilization methods are known to have difficulties to reach a steady-state ([6, 7])), it can be performed for liquid and gas phases, and, an analytical solution of the steady-state solution is available which allow for convergence study. The 1-D Leblanc shock tube test [32] (in a straight pipe) is also performed and consists of a flow developing shocks. A convergence study will be performed in order to demonstrate convergence of the numerical solution to the exact solution.

This section also included 2-D simulations from subsonic to supersonic flows. Subsonic flows of a gas over a 2-D cylinder and a hump [11] are simulated and results are shown for various far-field Mach numbers. Numerical results of a supersonic flow in a compression corner are provided to illustrate the capabilities of the new definition in the supersonic case. Convergence studies are performed when an analytical solution is available.

For each simulation, informations relative to the boundary conditions and the equa-

tion of state will be provided. All of the numerical solution presented in this section are run with the second-order temporal integrator *BDF2* and linear polynomials test functions. The integrals are numerically computed using a second-order Gauss quadrature rule. The Ideal Gas [35] or Stiffened Gas equation of state [28] are used and a generic formulation is recalled in Eq. (3.32).

$$P = (\gamma - 1)\rho(e - q) - \gamma P_\infty \quad (3.32)$$

where the parameters  $q$  and  $P_\infty$  are fluid dependent and will be specified in time. Eq. (3.32) degenerates to the Ideal Gas equation of state by setting  $q$  and  $P_\infty$  to zero. The Ideal and Stiffened Gas equation of states have a convex entropy  $s$ :

$$s = C_v \ln \left( \frac{P + P_\infty}{\rho^{\gamma-1}} \right)$$

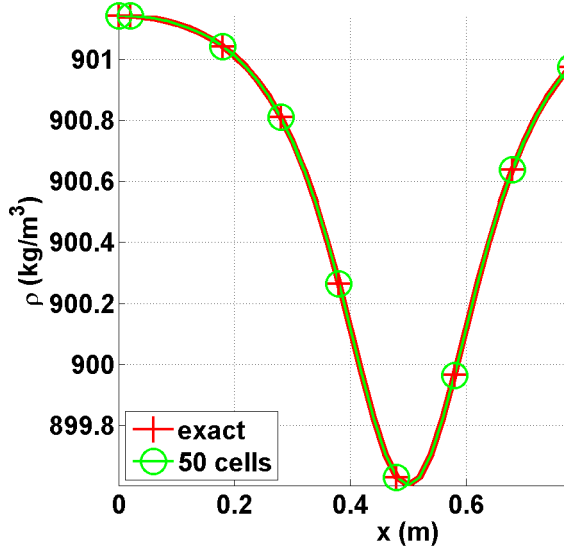
### 3.5.1 *Liquid water in a 1-D divergent-convergent nozzle*

The simulation consists of liquid water flowing through a 1-D convergent-divergent nozzle with the following equation,  $A(x) = 1 + 0.5 \cos(2\pi x/L)$ , where  $L = 1m$  is the length of the nozzle. At the inlet, the stagnation pressure and temperature are set to  $P_0 = 1MPa$  and  $T_0 = 453K$ , respectively. At the outlet, only the static pressure is specified:  $P_s = 0.5MPa$ . Details about the theory related to the inlet and outlet boundary conditions can be found in [37]. Initially, the temperature is uniform and set equal to the stagnation temperature and the pressure linearly decreases from the stagnation pressure to the static one. Finally, the liquid is assumed at rest. The Stiffened Gas equation of state is used to model the liquid water with the parameters provided in Table 3.1.

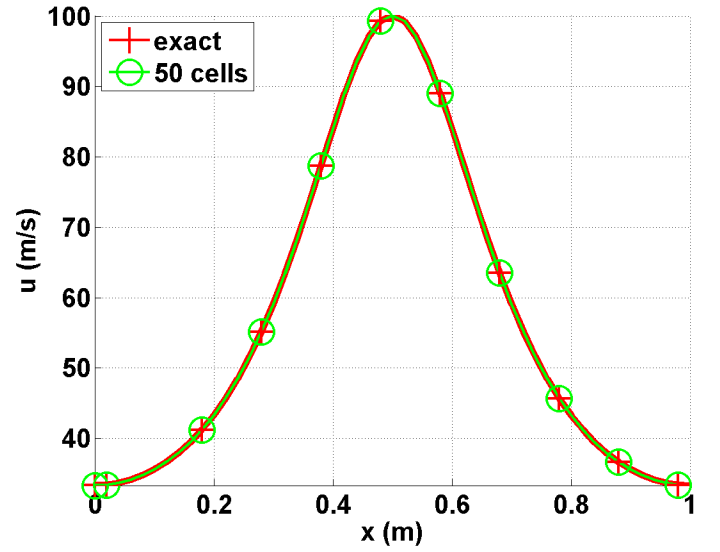
Table 3.1: Stiffened Gas Equation of State parameters for liquid water.

$\gamma$	$C_v \text{ (} J \cdot kg^{-1} \cdot K^{-1} \text{)}$	$P_\infty \text{ (} Pa \text{)}$	$q \text{ (} J \cdot kg^{-1} \text{)}$
2.35	1816	$10^9$	$-1167.10^3$

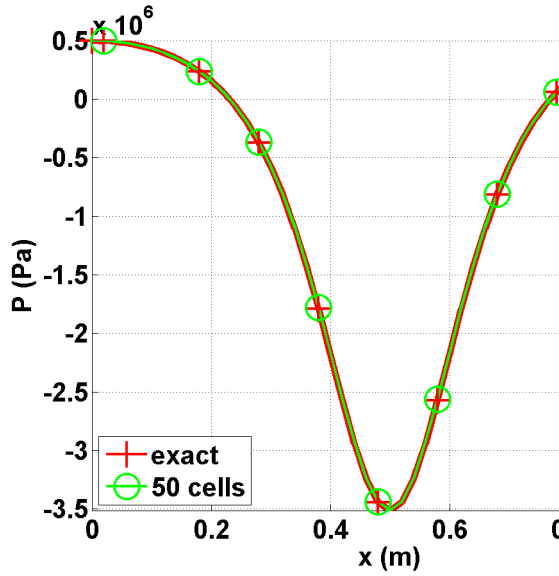
Because of the low pressure difference between the inlet and the outlet, and the large value of  $P_\infty$ , the flow remains subsonic and thus, should not display any shock. Enthalpy and entropy are conserved through the nozzle, and these conservation relations are used to determine the exact solution at steady-state [27]. Plots of the velocity, density and pressure are given at steady-state in Fig. 3.1a, Fig. 3.1b, Fig. 3.1c, respectively, along with the exact solution for comparison. The viscosity coefficients are also plotted in Fig. 3.1d. The mesh used is uniform and has 50 cells.



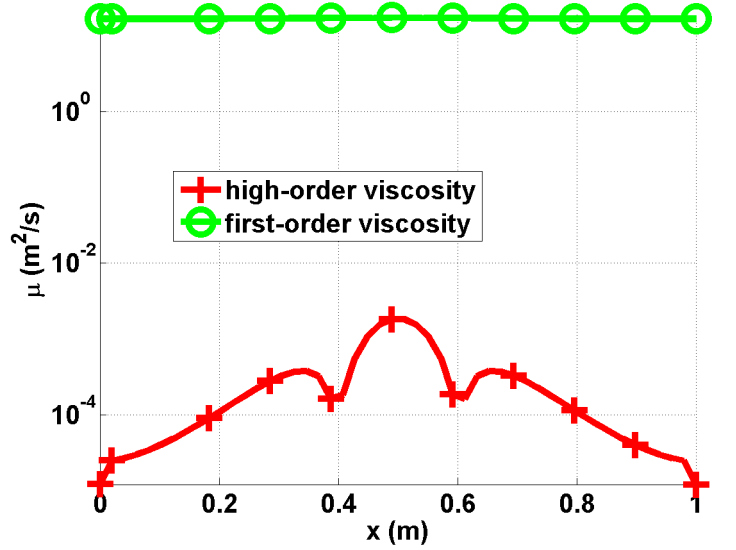
(a) Velocity solution at steady-state.



(b) Density solution at steady-state



(c) Pressure solution at steady-state.



(d) Viscosity coefficients at steady-state.

Figure 3.1: Steady-state solution for liquid phase in a 1-D convergent-divergent nozzle with an uniform mesh of 50 cells.

The numerical and exact solutions of the velocity, pressure and density given in Fig. 3.1 for a fairly coarse mesh (50 cells) perfectly overlap: it is noted that

the numerical solution is symmetric with respect to the nozzle throat located in  $x = 0.5m$ . The second-order viscosity coefficient is very small compare to the first-order one as expected: (i) the numerical solution is smooth as shown in Fig. 3.1d and (ii) the flow is in a low Mach regime and thus isentropic . A convergence study was performed using the exact solution as a reference: the L1 and L2 norms of the error and the corresponding convergence rates are computed at steady-state on various uniform mesh from 4 to 256 cells. The results for linear polynomials  $\mathbb{Q}_1$  are reported in Table 3.2 and Table 3.3 for the primitive variables: density, velocity and pressure.

Table 3.2: L1 norm of the error for the liquid phase in a 1-D convergent-divergent nozzle at steady-state.

cells	density	rate	pressure	rate	velocity	rate
4	$2.8037 \cdot 10^{-1}$	—	$8.4705e \cdot 10^5$	—	7.2737	—
8	$1.3343 \cdot 10^{-1}$	1.0713	$4.7893e \cdot 10^5$	0.24227	6.1493	0.074683
16	$2.9373 \cdot 10^{-2}$	2.1835	$1.0613e \cdot 10^5$	2.3247	1.2275	2.4501
32	$5.1120 \cdot 10^{-3}$	2.5225	$1.8446 \cdot 10^4$	2.6959	$1.8943 \cdot 10^{-1}$	3.0966
64	$1.0558 \cdot 10^{-3}$	2.2755	$3.7938 \cdot 10^3$	2.3207	$3.7919 \cdot 10^{-2}$	2.3323
128	$2.3712 \cdot 10^{-4}$	2.1547	$8.4471 \cdot 10^2$	2.0624	$8.5517 \cdot 10^{-3}$	2.0473
256	$5.6058 \cdot 10^{-5}$	2.0806	$1.9839 \cdot 10^2$	2.0478	$2.0475 \cdot 10^{-3}$	1.9833
512	$1.3278 \cdot 10^{-5}$	2.0778	46.622	2.0478	$4.9516 \cdot 10^{-4}$	1.9669



Table 3.3: L2 norm of the error for the liquid phase in a 1-D convergent-divergent nozzle at steady-state.

cells	density	rate	pressure	rate	velocity	rate
4	$3.106397 \cdot 10^{-1}$	—	$5.254445 \cdot 10^5$	—	3.288543	—
8	$7.491623 \cdot 10^{-2}$	2.07	$1.636966 \cdot 10^5$	1.60	1.823880	0.90
16	$2.079858 \cdot 10^{-2}$	1.80	$4.627338 \cdot 10^4$	1.75	$4.990605 \cdot 10^{-1}$	1.83
32	$5.329627 \cdot 10^{-3}$	1.90	$1.180287 \cdot 10^4$	1.92	$1.261018 \cdot 10^{-1}$	1.93
64	$1.341583 \cdot 10^{-3}$	1.94	$2.967104 \cdot 10^3$	1.98	$3.160914 \cdot 10^{-2}$	1.99
128	$3.359766 \cdot 10^{-4}$	1.99	$7.428087 \cdot 10^2$	1.99	$7.907499 \cdot 10^{-3}$	1.99
256	$8.403859 \cdot 10^{-5}$	1.99	$1.857861 \cdot 10^2$	1.99	$1.977292 \cdot 10^{-3}$	1.99
512	$2.10075 \cdot 10^{-5}$	1.99	27.048	1.99	$4.9516 \cdot 10^{-4}$	1.99

It is observed that the convergence rate for the L1 and L2 norm of the error is 2: the entropy viscosity method conserves the high-order accuracy when the numerical solution is smooth, and the new definition of the entropy viscosity coefficient seems to behave as expected in the low Mach limit.

### 3.5.2 Steam in a 1-D divergent-convergent nozzle

Instead of liquid water, we now simulate a flow of steam using the exact same 1-D geometry, initial conditions and boundary conditions as in Section 3.5.1. The Stiffened gas equation of state is still used but with different parameters that are given in Table 3.4: steam is a gas and compressible effects will become dominant.

Table 3.4: Stiffened Gas Equation of State parameters for steam.

$\gamma$	$C_v \text{ (} J \cdot kg^{-1} \cdot K^{-1} \text{)}$	$P_\infty \text{ (} Pa \text{)}$	$q \text{ (} J \cdot kg^{-1} \text{)}$
1.43	1040	0	$2030 \cdot 10^3$

The pressure difference applied between the inlet and outlet is large enough to make the steam accelerates through the nozzle and result in the formation of shock in the divergent part. The behavior is different from what is observed for the liquid water phase in Section 3.5.1 because of the liquid to gas density ratio that is of 1000. Even though a shock forms, an exact solution at steady-state is still available [27]. The objective of this section is to show that using the new definition of the viscosity coefficient in Eq. (3.20), the shock can be correctly resolved without spurious oscillation. The steady-state numerical solution is shown in Fig. 3.2 and was run with a mesh of 1600 cells.

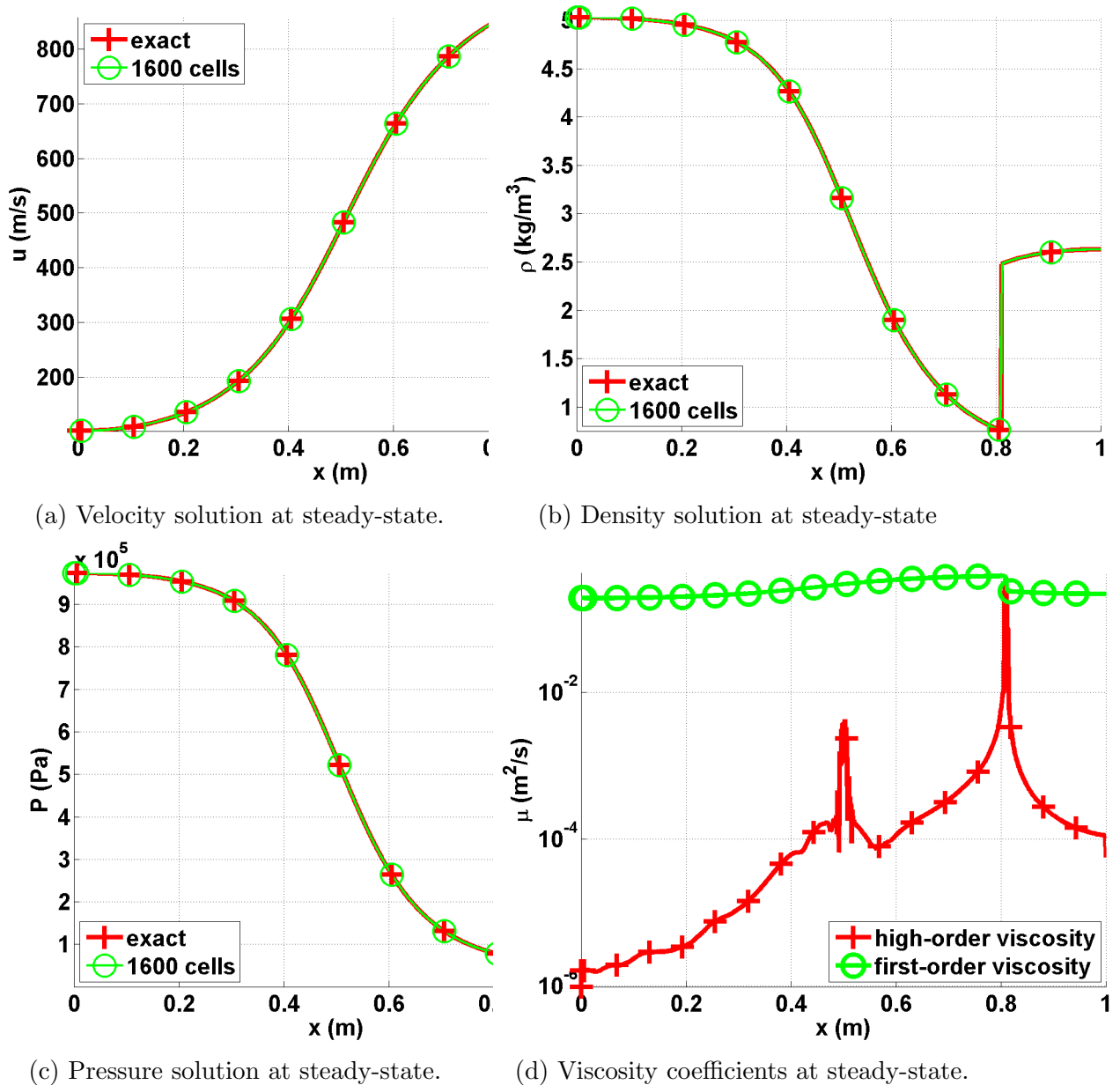


Figure 3.2: Steady-state solution for vapor phase in a 1-D convergent-divergent nozzle.

The steady-state solution of the density, velocity and pressure are given in Fig. 3.2a, Fig. 3.2b and Fig. 3.2c. The steady-solution displays a shock around  $x = 0.8m$  and

match the exact solution. In Fig. 3.2d, the first- and second-order viscosity coefficients are log plotted at steady-state: the second-order viscosity coefficient is peaked in the shock region around  $x = 0.8m$  as expected, and saturate to the first-order viscosity coefficient. The profile also displays another peak at  $x = 0.5m$  that corresponds to the position of the sonic point for a 1-D convergent-divergent nozzle: this particular point is known to develop small instabilities that are detected when computing the jumps of the pressure and density gradients. Anywhere else, the second-order viscosity coefficient is small. In order to prove convergence of the numerical solution to the exact solution, a convergence study is performed. Because of the presence of a shock, second-order accuracy cannot be achieved. However, the convergence rate of a numerical solution containing a shock is known and expected to be of 1 and 1/2 when computing the L1 and L2 norms of the error, respectively (see Theorem 9.3 in [12]). Results are reported in Table 3.5 and Table 3.6 for the primitive variables: density, velocity and pressure.

Table 3.5: L1 norm of the error for the vapor phase in a 1-D convergent-divergent nozzle at steady-state.

cells	density	rate	pressure	rate	velocity	rate
5	$0.72562 \cdot 10^{-1}$	—	$1.5657 \cdot 10^5$	—	173.69	—
10	$0.4165 \cdot 10^{-1}$	0.80088	$9.6741 \cdot 10^4$	0.63425	120.69	0.52519
20	$0.20675 \cdot 10^{-1}$	1.0104	$4.9193 \cdot 10^4$	0.96971	72.149	0.74228
40	$0.093703 \cdot 10^{-1}$	1.1417	$2.0103 \cdot 10^4$	0.72728	34.716	1.0554
80	$0.047328 \cdot 10^{-1}$	0.9854	$1.0208 \cdot 10^4$	0.9777	16.082	1.1101
160	$0.023965 \cdot 10^{-2}$	0.9817	$5.1969 \cdot 10^3$	0.9739	7.9573	1.0150
320	$0.020768 \cdot 10^{-2}$	0.9886	$2.5116 \cdot 10^3$	1.0490	3.7812	1.0734
640	$0.0059715 \cdot 10^{-2}$	1.0160	$1.2754 \cdot 10^3$	0.9776	1.8353	1.0428

Table 3.6: L2 norm of the error for the vapor phase in a 1-D convergent-divergent nozzle at steady-state.

cells	density	rate	pressure	rate	velocity	rate
5	$9.7144 \cdot 10^{-1}$	—	$2.0215 \cdot 10^5$	—	236.94	—
10	$5.9718 \cdot 10^{-1}$	0.70195	$1.3024 \cdot 10^5$	0.63425	166.56	0.50854
20	$2.9503 \cdot 10^{-1}$	1.0173	$6.6503 \cdot 10^4$	0.96971	103.36	0.68831
40	$1.8193 \cdot 10^{-1}$	0.69747	$4.0171 \cdot 10^4$	0.72728	66.374	0.6390
80	$1.3366 \cdot 10^{-1}$	0.44485	$2.3163 \cdot 10^4$	0.43576	42.981	0.62692
160	$9.6638 \cdot 10^{-2}$	0.46790	$1.7263 \cdot 10^4$	0.42413	31.717	0.43844
320	$7.0896 \cdot 10^{-2}$	0.44688	$1.2763 \cdot 10^4$	0.43571	23.138	0.45499
640	$5.2191 \cdot 10^{-2}$	0.44190	$9.4217 \cdot 10^3$	0.43790	16.910	0.45238

The convergence rates for the L1 and L2 norms of the error are close to the theoretical values which prove convergence of the numerical solution to the exact solution.

It is also interesting to investigate the effect of the first-order viscosity onto the steady-state solution. In Fig. 3.3, the steady-state velocity profile is plotted when using the first- and second-order viscosity coefficients: the main difference between the two numerical solution is in the resolution of the shock around  $x = 0.8m$ . The first-order viscosity coefficient is by definition more dissipative and will smooth out the solution. In the other hand, the high-order viscosity better resolves the shock and allow high-order accuracy away from the shock region. It is also noted that the numerical solution obtained with the first-order viscosity coefficient is satisfying: this is due to the nature of the solution that contains a standing shock, and thus,

will force the shock to form even with large artificial dissipation.

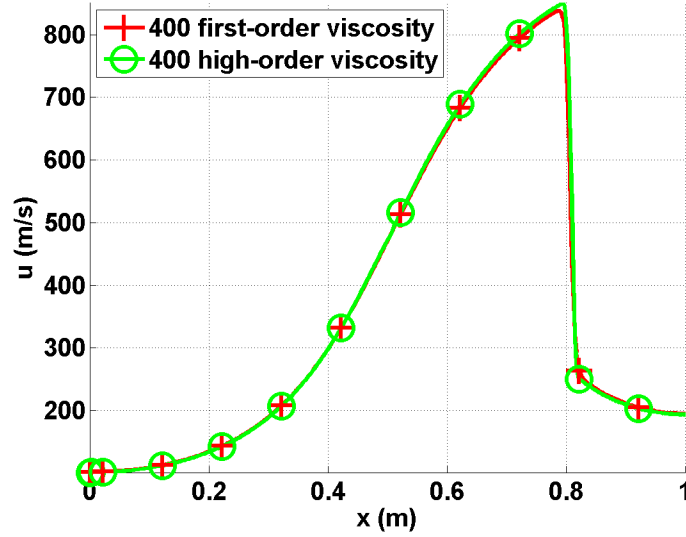


Figure 3.3: Velocity profile at steady-state with the first- and second-order viscosity for a mesh with 400 cells.

### 3.5.3 Leblanc shock tube

The 1-D Leblanc shock tube is a Riemann problem designed to test the robustness and the accuracy of the stabilization method. The initial conditions are given in Table 3.7. The ideal gas equation of state is used to compute the fluid pressure with the following heat capacity ratio  $\gamma = 5/3$ .

Table 3.7: Initial conditions for the 1-D Leblanc shock tube.

	$\rho$	$u$	$e$
left	1.	0.	0.1
right	$10^{-3}$	0.	$10^{-7}$

This test is computationally challenging because of the large left to right pressure ratio. The computational domain consists of a 1-D pipe of length  $L = 9m$  with an interface located at  $x = 2m$ . At  $t = 0.s$ , the interface is removed, allowing the fluid to move. The numerical solution is run until  $t = 4.s$  and the density, momentum and total energy profiles are given in Fig. 3.4a, Fig. 3.4b and Fig. 3.4c, respectively, along with the exact solution. The viscosity coefficients are also plotted in Fig. 3.4d. These plots were run with three different uniform mesh of 800, 3200 and 6000 cells and a constant time step  $\Delta t = 10^{-3}s$ .



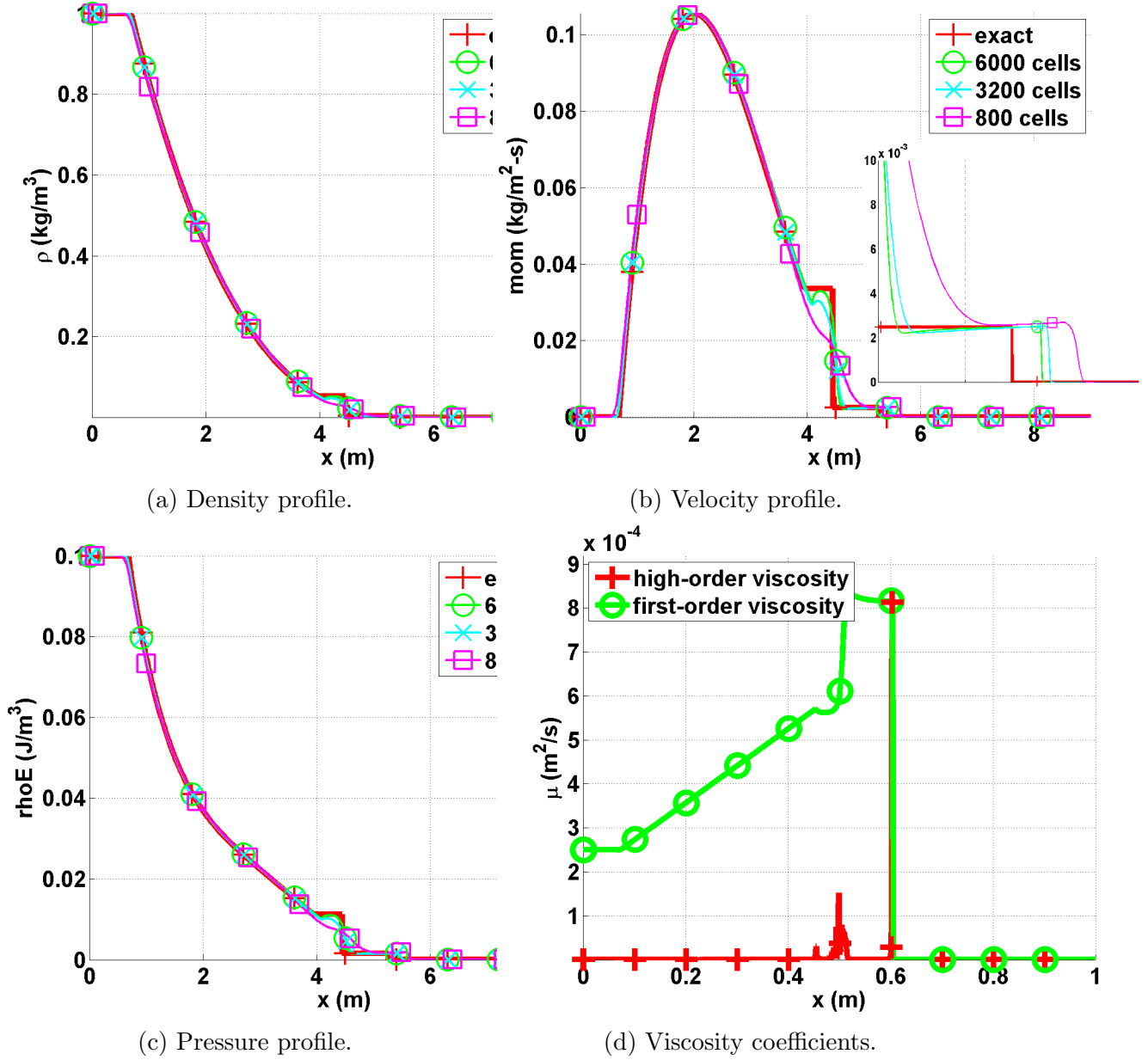


Figure 3.4: Numerical solution for the 1-D Leblanc shock tube at  $t = 4.s$ .

The density, momentum and total energy profiles given in Fig. 3.4 do not display any oscillations. In Fig. 3.4b, the shock region is zoomed in for better resolution: the shock is well resolved and do not show any oscillation. It is also observed that

the shock position of the numerical solution converges to the exact position when refining the mesh. The contact wave is shown in Fig. 3.4b at  $x = 4.5m$ . The second-order viscosity coefficient profile is shown in Fig. 3.4d and behaves as expected: it saturates to the first-order viscosity in the shock region and thus prevent oscillations from forming. In the contact wave at  $x = 4.5m$ , a smaller peak is observed that is due to the presence of the jumps in the definition of the second-order viscosity coefficient (Eq. (3.20)).

Once again, a convergence study is performed in order to prove convergence of the numerical solution to the exact solution. As for the vapor phase in the 1-D nozzle (Section 3.5.2), the expected convergence rate for the L1 and L2 norms of the error are 1 and 1/2, respectively. The exact solution was obtained by running a 1-D Riemann solver and used as a reference solution to compute the L1 and L2-norms of the error that are reported in Table 3.8 and Table 3.9 for the conservative variables: density, momentum and total energy.

Table 3.8: L1 norm of the error for the 1-D Leblanc test at  $t = 4.s$ .

cells	density	rate	momentum	rate
100	$1.0354722 \cdot 10^{-2}$	—	$3.5471714 \cdot 10^{-3}$	—
200	$7.2680512 \cdot 10^{-3}$	0.51064841	$2.5933119 \cdot 10^{-3}$	0.45187331
400	$5.0825628 \cdot 10^{-3}$	0.51601245	$2.0668092 \cdot 10^{-3}$	0.32739054
800	$3.4025056 \cdot 10^{-3}$	0.57895861	$1.4793838 \cdot 10^{-3}$	0.48240884
1600	$2.1649953 \cdot 10^{-3}$	0.65223363	$9.7152832 \cdot 10^{-4}$	0.6066684
3200	$1.2465433 \cdot 10^{-3}$	0.79643094	$5.5937409 \cdot 10^{-4}$	0.79644263
6400	$6.4476928 \cdot 10^{-4}$	0.95107804	$3.0244198 \cdot 10^{-4}$	0.88715502
12800	$3.3950948 \cdot 10^{-4}$	0.92533116	$1.5958118 \cdot 10^{-4}$	0.9223679

cells	total energy	rate
100	0.0014033046	—
200	$9.8611746 \cdot 10^{-4}$	0.5089968
400	$7.7844421 \cdot 10^{-4}$	0.34116585
800	$5.5702549 \cdot 10^{-4}$	0.48285029
1600	$3.5720171 \cdot 10^{-4}$	0.64100438
3200	$2.0491799 \cdot 10^{-4}$	0.80169235
6400	$1.0914891 \cdot 10^{-4}$	0.90874889
12800	$5.7909794 \cdot 10^{-5}$	0.91441847

Table 3.9: L2 norm of the error for the 1-D Leblanc test at  $t = 4.s$ .

cells	density	rate	momentum	rate
100	$5.7187851 \cdot 10^{-3}$	—	$1.7767236 \cdot 10^{-3}$	—
200	$3.8995238 \cdot 10^{-3}$	0.55241073	$1.4913161 \cdot 10^{-3}$	0.25263314
400	$2.8103526 \cdot 10^{-3}$	0.4725468	$1.3305301 \cdot 10^{-3}$	0.164585
800	$2.1081933 \cdot 10^{-3}$	0.41474398	$1.1398931 \cdot 10^{-3}$	0.22310254
1600	$1.5731052 \cdot 10^{-3}$	0.42239201	$9.0394227 \cdot 10^{-4}$	0.33459602
3200	$1.0610667 \cdot 10^{-3}$	0.56809979	$6.2735595 \cdot 10^{-4}$	0.52694639
6400	$7.3309974 \cdot 10^{-4}$	0.53343397	$4.4545754 \cdot 10^{-4}$	0.49399631
12800	$5.1020991 \cdot 10^{-4}$	0.52291857	$3.1266758 \cdot 10^{-4}$	0.5106583

cells	total energy	rate
100	$7.6112265 \cdot 10^{-4}$	—
200	$5.5497308 \cdot 10^{-4}$	0.45571115
400	$4.6063172 \cdot 10^{-4}$	0.26880405
800	$3.7798953 \cdot 10^{-4}$	0.28526749
1600	$2.9584646 \cdot 10^{-4}$	0.35349763
3200	$2.054455 \cdot 10^{-4}$	0.52609289
6400	$1.4670834 \cdot 10^{-4}$	0.48580482
12800	$1.0299897 \cdot 10^{-5}$	0.51032105

The convergence rates are close to the expected values which prove convergence of the numerical solution to the exact solution.

### 3.5.4 Typical 1-D shock tubes [41]

## 3.6 2-D numerical results for supersonic flows:

This section focuses on demonstrating the ability of the entropy viscosity method, with the new definition of the viscosity coefficients derived in Section 3.3.2, to accurately resolve shocks occurring in transonic flows. Such tests were already performed in [43] with the former definition of the entropy viscosity method recalled in Section 3.2.1, and using a discontinuous Galerkin finite element discretization. Our objective here, is to show that the new definition of the viscosity coefficients is still capable of resolving shocks. The numerical tests presented in this section include: flow past a forward facing step (REFS), a circular explosion (REFS), a steady-state flow over a double wedge and a steady-state flow in a compression corner. The last two tests will also allow us to evaluate the ability of the method to reach a steady-state. For each numerical results presented in this section, information relative to the equation of state and its parameters, the boundary conditions, the initial conditions, the mesh and the discretization order will be provided along with the numerical results. For clarity purpose we will refer to as  $\Omega$ . Since only 2-D computational domain is considered, left, right, bottom and top boundaries are referred to as  $\delta\Omega_1$ ,  $\delta\Omega_2$ ,  $\delta\Omega_3$  and  $\delta\Omega_4$ , respectively, with  $\delta\Omega = (\delta\Omega_1, \delta\Omega_2, \delta\Omega_3, \delta\Omega_4)$ .

### 3.6.1 Supersonic 2-D flow over a forward facing step:

This benchmark was first introduced by (NAME + REF) and later popularized by Woodward et al. (REF). It consists of a Mach 3 flow past a forward-facing step in a 2-D wind tunnel. The geometry is given in (FIGURE) and was discretized with an uniform mesh of  $1.5 \times 10^4$  cells. A supersonic inlet boundary condition is used to set the flow conditions. A slip wall boundary condition is specified at the top and bottom wall following the method explained in (SECTION FOR BCS). The

outflow, in  $x = 4$  is free since the flow remains supersonic at the outlet boundary. The uniform initial conditions are given in Table 3.10 for the primitive variables. The Ideal gas equation of state is used with a adiabatic gas constant  $\gamma = 1.4$ .

Table 3.10: Initial conditions for a 2-D supersonic flow past a forward-facing step.

primitive variables	$\rho$	$\vec{u}$	P
value	1.4	(3., 0.)	1.

The numerical solution was obtained with a  $Q_1$  continuous Galerkin finite element method and the second-order temporal integrator *BDF2*. The solution was run until  $t = 4.s$  with a *CFL* of 2. The density and viscosity coefficients profiles are plotted at different times during the transient, to witness how the entropy-viscosity method adapt to the solution itself.

### 3.6.2 2-D circular explosion:

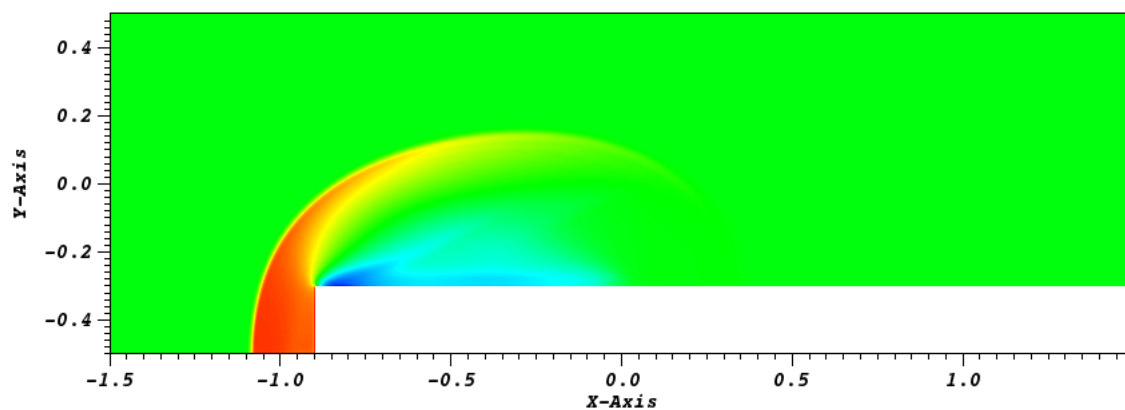
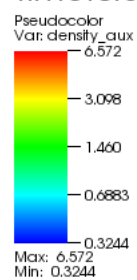
We now consider a 2-D circular explosion (REFS) that is known to develop an unstable layer contact. The computational domain is a square of dimension  $\Omega = (-1, 1)^2$  as shown in (FIGURE). The initial conditions are also given in (FIGURE) and consists of a pressure and density step located in the center of the computational domain. The values of the initial conditions are given in Table 3.11 in function of the radius  $r^2 = x^2 + y^2$ . The Ideal gas equation of state is sill used with the same parameters as in Section 3.6.1. Dirichlet boundary conditions are used to specify the values on the boundaries  $\delta\Omega$  of the computational domain  $\Omega$ , assuming that the simulation is stopped before the waves reach the boundaries.

Table 3.11: Initial conditions for a 2-D explosion.

primitive variables	$\rho$	$\vec{u}$	P
$r \in [0, 0.4]$	1	(0, 0)	1
$r \geq 0.4$	0.125	(0, 0)	0.1

Once again, the numerical solution was obtained with a  $\mathbb{Q}_1$  continuous Galerkin finite element method and the second-order temporal integrator *BDF2*. The solution was run until  $t = 0.25s$  with a *CFL* of 2. An uniform mesh was used made of 2000 elements. The density and the viscosity coefficients profiles are given in Fig. 3.5-Fig. 3.12. It was chosen to show the numerical solution at times  $t = 0.314$ ,  $t = 0.664$ ,  $t = 1.551$  and  $t = 4$  s to illustrate the ability of the entropy viscosity method to detect shocks and discontinuities during a transient, and add significant dissipation only in their close neighborhood.

DB: ForwardFacingStep\_out\_save.e  
Time:0.314



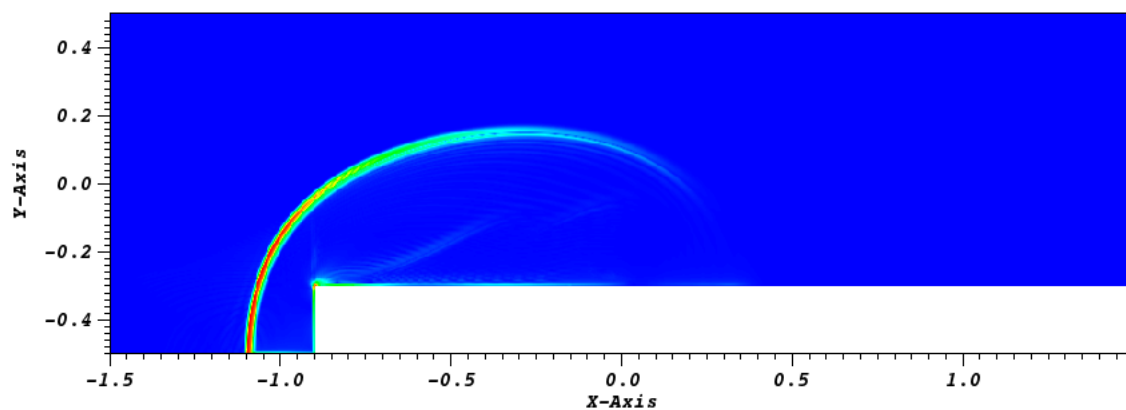
user: delchini  
Wed May 14 15:59:30 2014

Figure 3.5: Density solution at  $t = 0.314$  s.



DB: ForwardFacingStep\_out\_save.e  
Time:0.314

Pseudocolor  
Var: mu\_aux  
0.006864  
0.005148  
0.003432  
0.001716  
2.371e-12  
Max: 0.006864  
Min: 2.371e-12

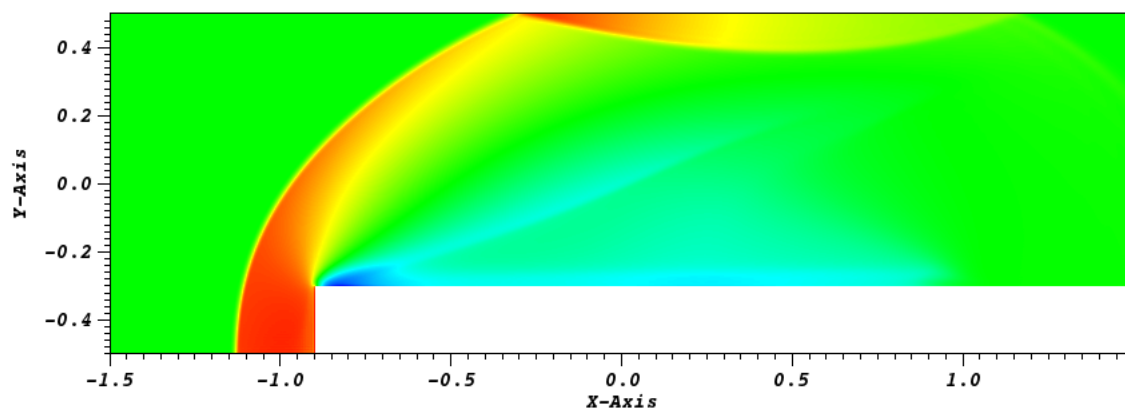


user: delchini  
Wed May 14 15:51:08 2014

Figure 3.6: Viscosity coefficient solution at  $t = 0.314$  s.

DB: ForwardFacingStep\_out\_save.e  
Time:0.664

Pseudocolor  
Var: density\_aux  
6.567  
3.024  
1.392  
0.6411  
0.2952  
Max: 6.567  
Min: 0.2952

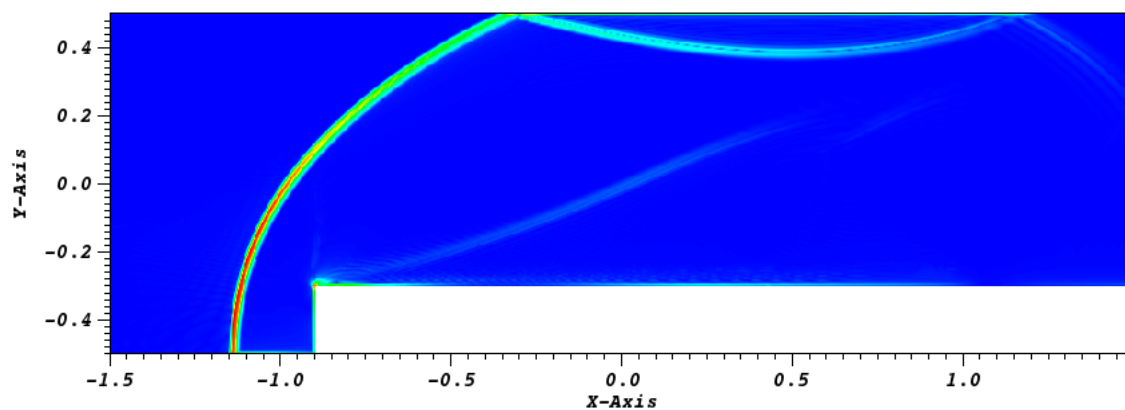


user: delchini  
Wed May 14 15:54:46 2014

Figure 3.7: Density solution at  $t = 0.664$  s.

DB: ForwardFacingStep\_out\_save.e  
Time:0.664

Pseudocolor  
Var: mu\_aux  
0.006815  
0.005111  
0.003408  
0.001704  
3.255e-12  
Max: 0.006815  
Min: 3.255e-12

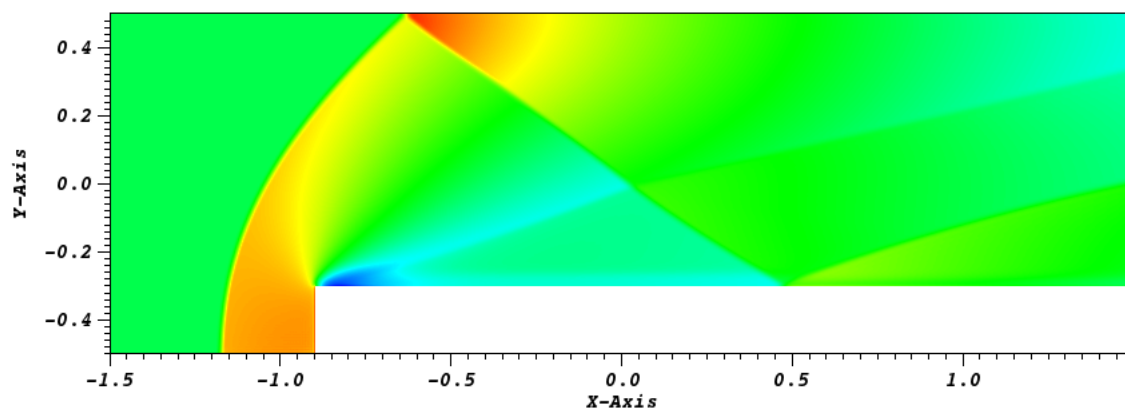


user: delchini  
Wed May 14 15:53:35 2014

Figure 3.8: Viscosity coefficient solution at  $t = 0.664$  s.

DB: ForwardFacingStep\_out\_save.e  
Time: 1.514

Pseudocolor  
Var: density\_aux  
9.487  
4.141  
1.807  
0.7887  
0.3442  
Max: 9.487  
Min: 0.3442

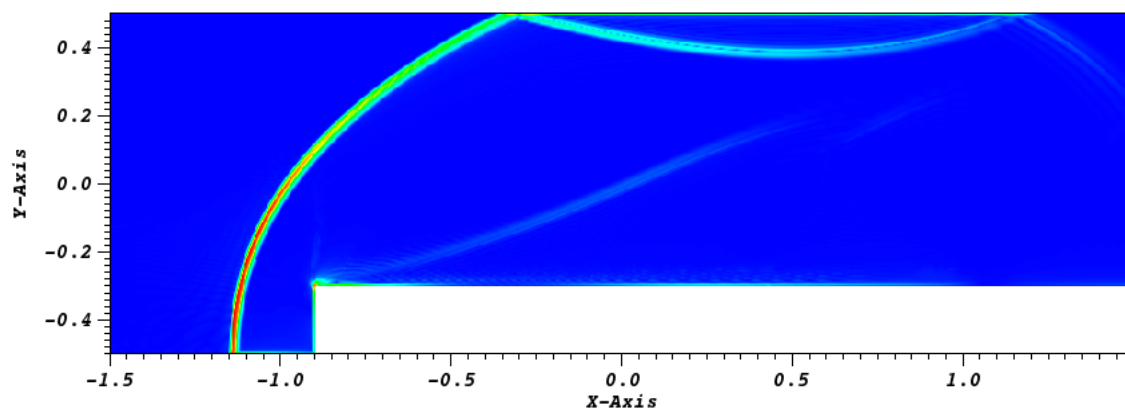


user: delchini  
Wed May 14 15:56:46 2014

Figure 3.9: Density solution at  $t = 1.514$  s.

DB: ForwardFacingStep\_out\_save.e  
Time:0.664

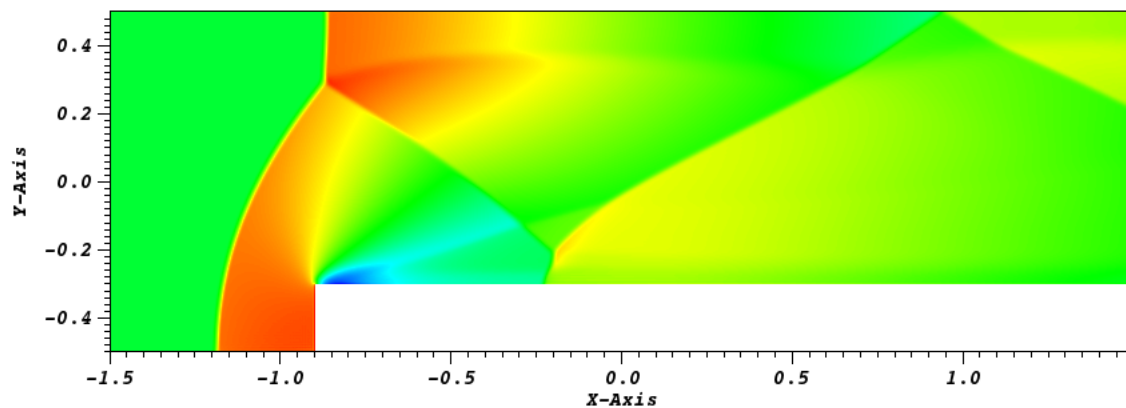
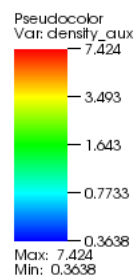
Pseudocolor  
Var: mu\_aux  
0.006815  
0.005111  
0.003408  
0.001704  
3.255e-12  
Max: 0.006815  
Min: 3.255e-12



user: delchini  
Wed May 14 15:53:35 2014

Figure 3.10: Viscosity coefficient solution at  $t = 1.514$  s.

DB: ForwardFacingStep\_out\_save.e  
Time:4



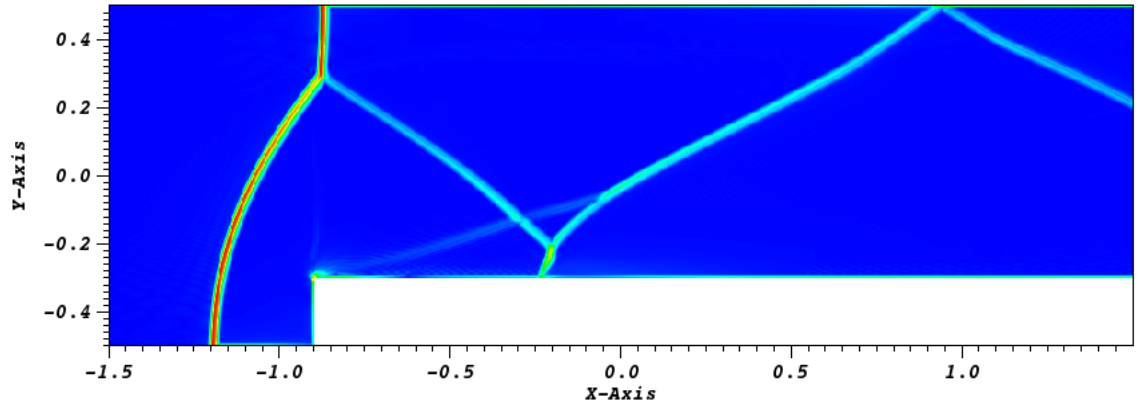
user: delchini  
Wed May 14 15:58:39 2014

Figure 3.11: Density solution at  $t = 4$  s.

DB: ForwardFacingStep\_out\_save.e

Time:4

Pseudocolor  
Var:  $\mu_{aux}$   
0.006790  
0.005092  
0.003395  
0.001698  
0.000000  
Max: 0.006790  
Min: 0.000000



user: delchini  
Wed May 14 15:58:11 2014

Figure 3.12: Viscosity coefficient solution at  $t = 4$  s.

The numerical solution of the density at  $t = 4$  s compares well to the ones obtained in (REFS), as least in a visual norm. The triple-point feature and the contact wave emerging from it are well resolved even if no Kelvin-Helmoltz instability is observed (REF). It is also noticed that a significant amount of entropy is produced near the corner region. This is due to the corner singularity and this phenomenon is well documented (REFS). This artifact can be treated either by using special boundary condition to the corner since its normal vector is not defined, or by aggressively re-

fining the mesh in the singularity region, or lastly, by modifying the geometry and use a round corner.

### 3.6.3 Riemann problem number 12:

Riemann problem number 12 (REF) is a popular 2-D benchmark that is known to develop contact and shock waves, as well as fine structures. The computational domain  $\Omega = (0, 1)^2$  is initialized with four square regions. In each region a different set of initial values is set as follows:

$$\left\{ \begin{array}{llll} \rho = 4/5, & \vec{u} = (0, 0) & P = 1 & \text{for } x \in (0, 0.5) \text{ and } y \in (0, 0.5) \\ \rho = 1, & \vec{u} = (3/\sqrt{17}, 0) & P = 1 & \text{for } x \in (0, 0.5) \text{ and } y \in (0.5, 1) \\ \rho = 17/32, & \vec{u} = (0, 3/\sqrt{17}) & P = 1 & \text{for } x \in (0.5, 1) \text{ and } y \in (0, 0.5) \\ \rho = 17/32, & \vec{u} = (0, 0) & P = 2/5 & \text{for } x \in (0.5, 1) \text{ and } y \in (0.5, 1) \end{array} \right.$$

The same equation of state as in Section 3.6.1 is used. An uniform mesh of  $400 \times 400$  elements was used along with a  $\mathbb{Q}_1$  continuous Galerkin finite element method and the second-order temporal integrator *BDF2*. The simulation is run until  $t = 0.25s$  with a *CFL* of 1. The density and viscosity profiles are given in (FIGS).

### 3.6.4 Supersonic flow in a compression corner

This is an example of a supersonic flow over a wedge of angle  $15^\circ$  where an oblique shock is generated at steady-state. The Mach number upstream of the shock is fixed to  $M = 2.5$ . The initial conditions are uniform: the pressure and temperature are set to  $P = 101325 \text{ Pa}$  and  $T = 300 \text{ K}$ , respectively. The initial velocity is computed from the upstream Mach number and using the Ideal Gas equation of state with the same parameters as in Section 3.7.2. The code is run until steady-state. An analytical solution for this supersonic flow is available and give the downstream to upstream pressure, entropy and Mach number ratios [1]. The analytical and



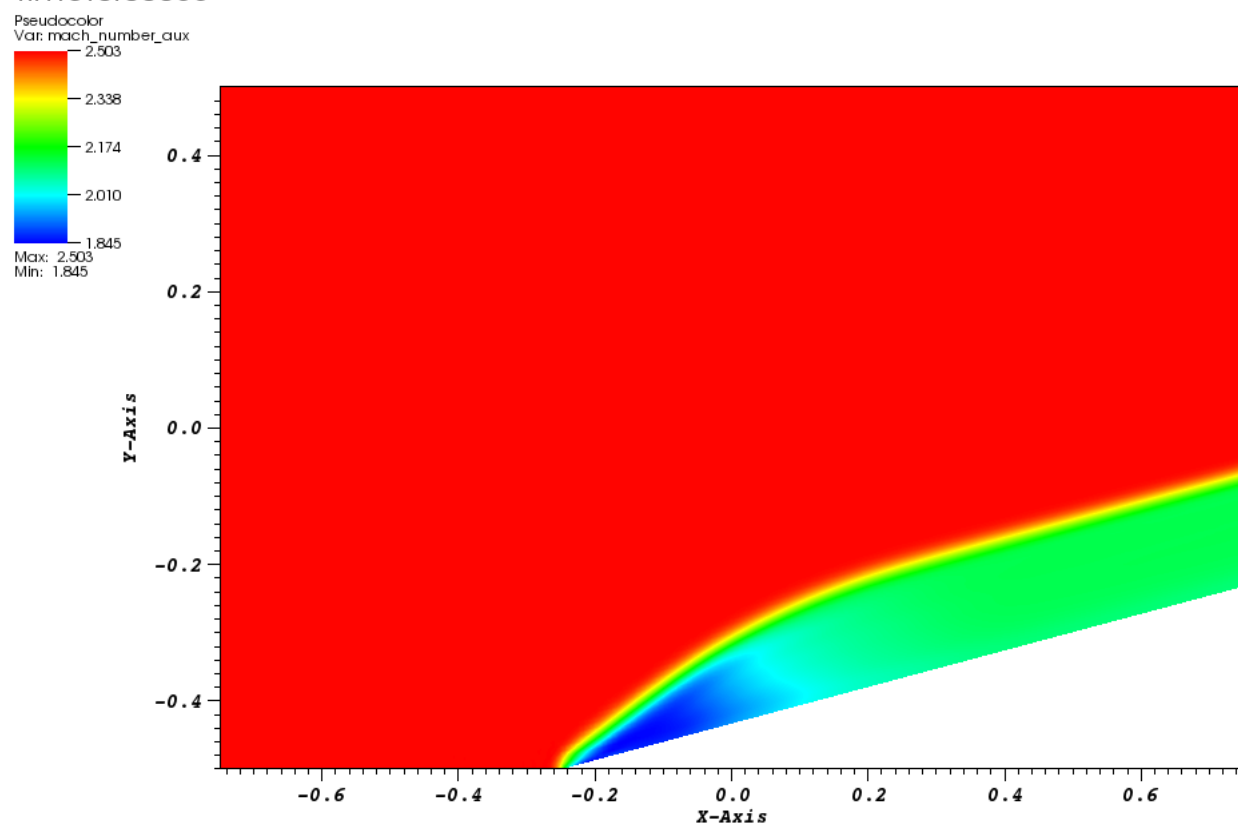
numerical ratios are given in see in Table 3.12, and are very close. The pressure and viscosity coefficient solution are given for different times in Fig. 3.13 - Fig. 3.18.

Table 3.12: Analytical solution for the supersonic flow on an edge eat  $15^\circ$  at  $M = 2.5$ .

	analytical downstream to upstream ratio	numerical downstream to upstream ratio
Pressure	2.47	2.467
Mach number	0.74	0.741
Entropy	1.03	1.026

The inlet is supersonic and therefore, the pressure, temperature and velocity are specified using Dirichlet boundary conditions. The outlet is also supersonic and none of the characteristics enter the domain through this boundary: the values will be computed by the implicit solver.

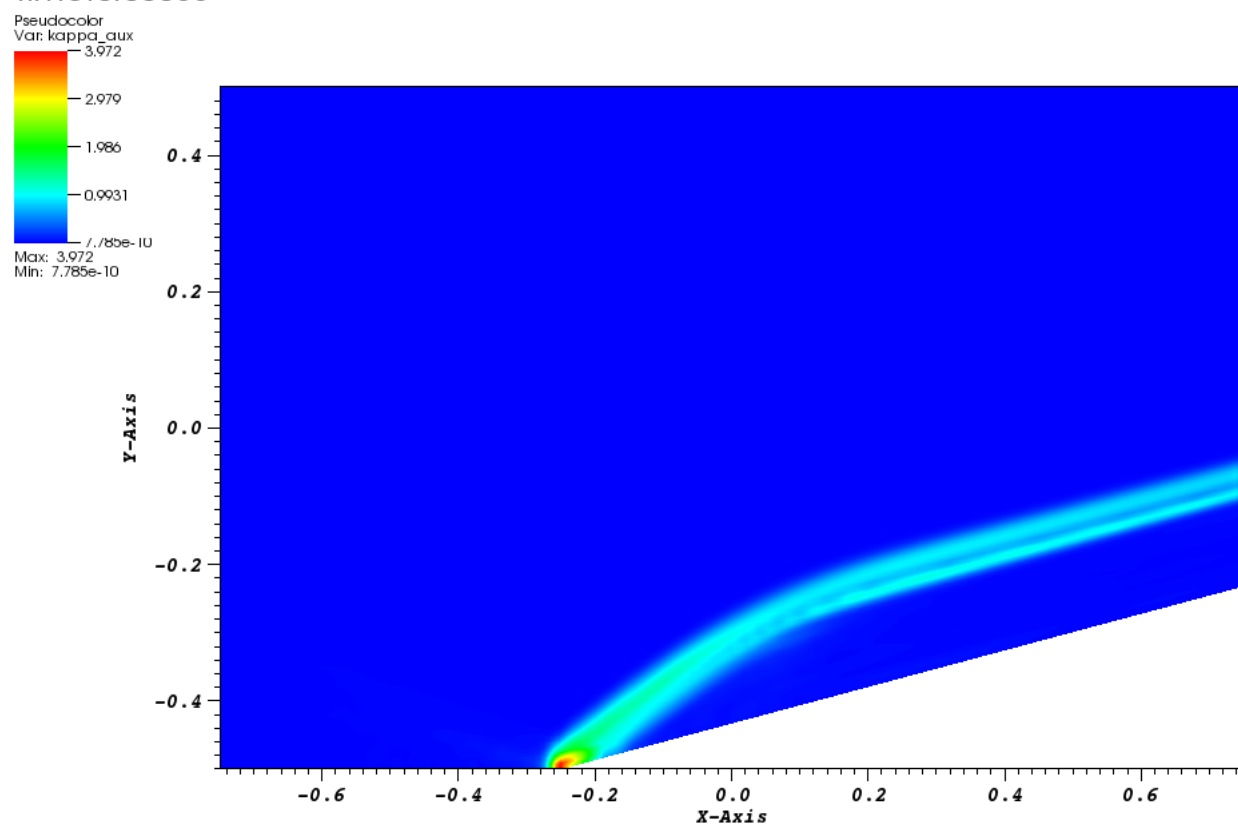
DB: CompressionCorner2DQuad\_high\_pressure\_out.e  
Time:0.00055



user: delchini  
Wed May 14 16:42:33 2014

Figure 3.13: Pressure solution at  $t = 5.5 \times 10^{-4}$ .

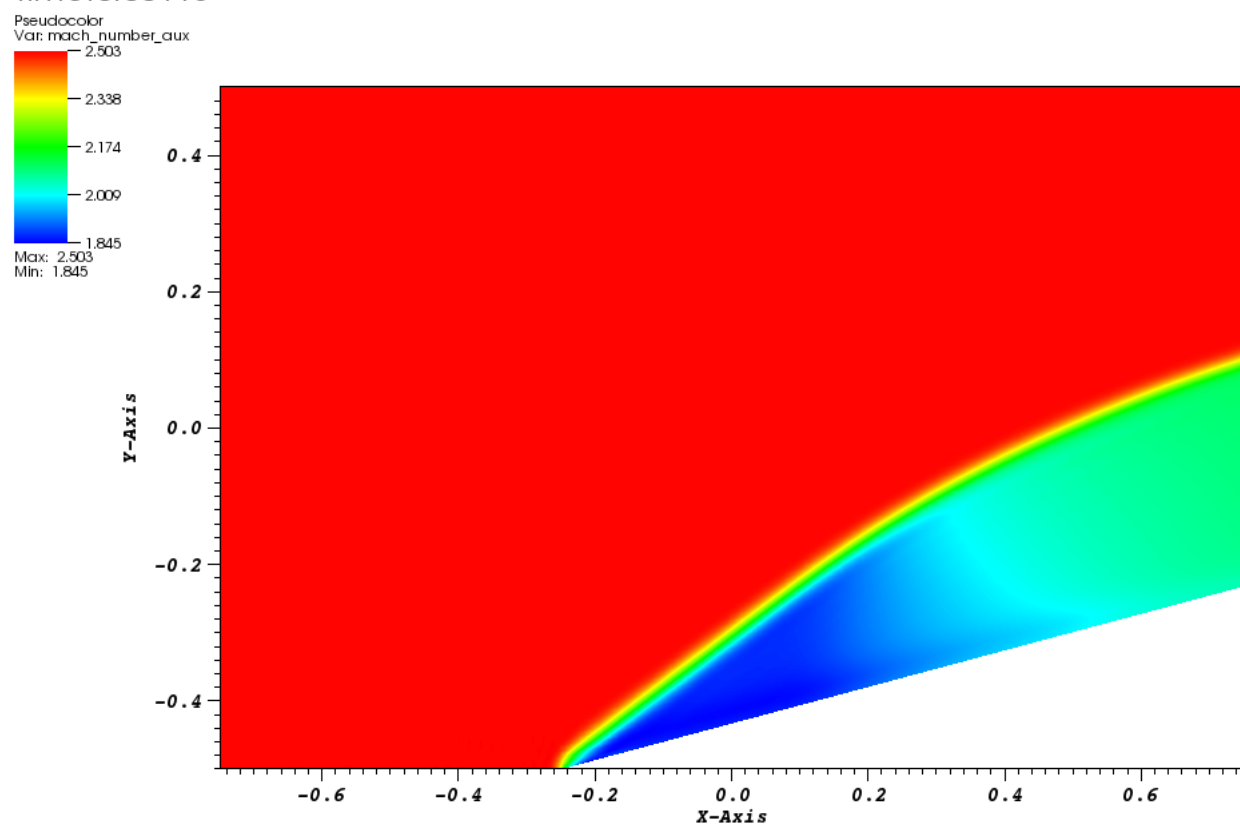
DB: CompressionCorner2DQuad\_high\_pressure\_out.e  
Time:0.00055



user: delchini  
Wed May 14 16:43:40 2014

Figure 3.14: Viscosity coefficient at  $t = 5.5 \times 10^{-4}$ .

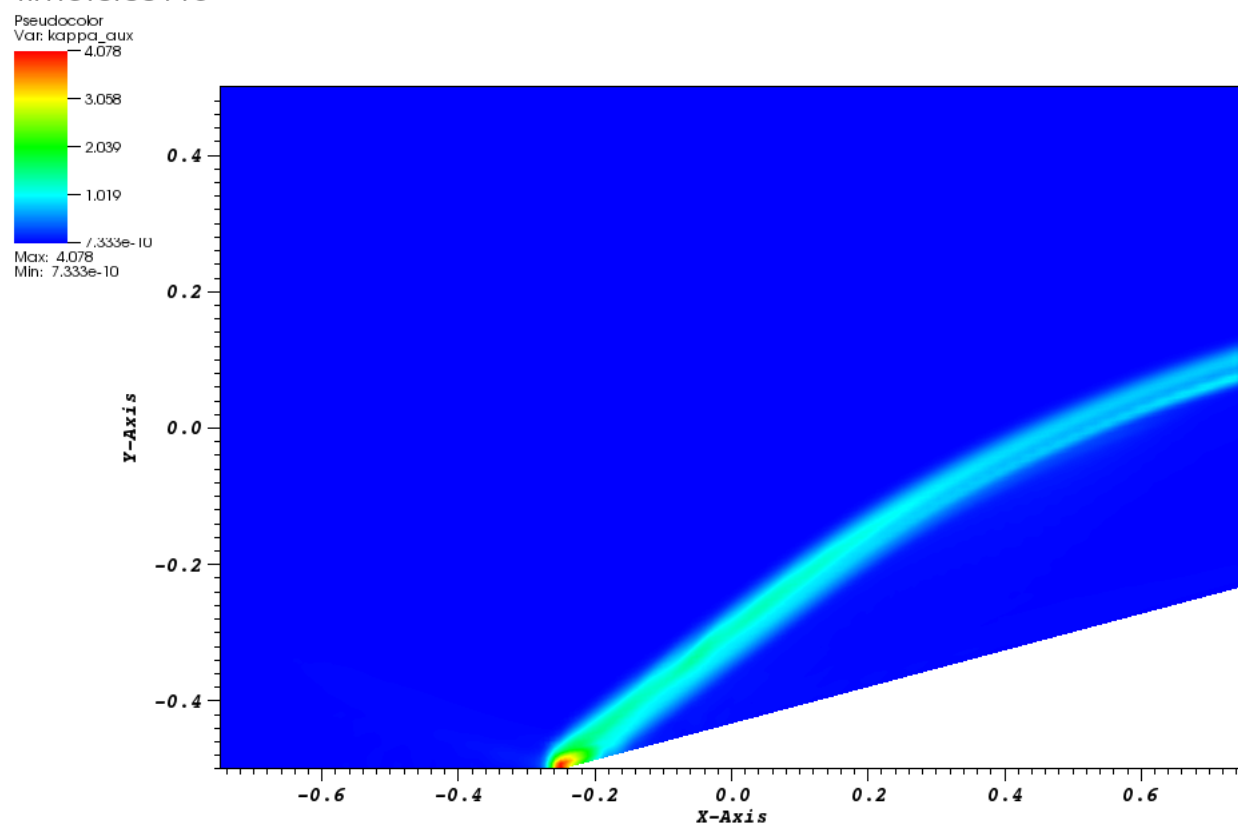
DB: CompressionCorner2DQuad\_high\_pressure\_out.e  
Time:0.00115



user: delchini  
Wed May 14 16:44:54 2014

Figure 3.15: Pressure solution at  $t = 1.15 \times 10^{-3}$ .

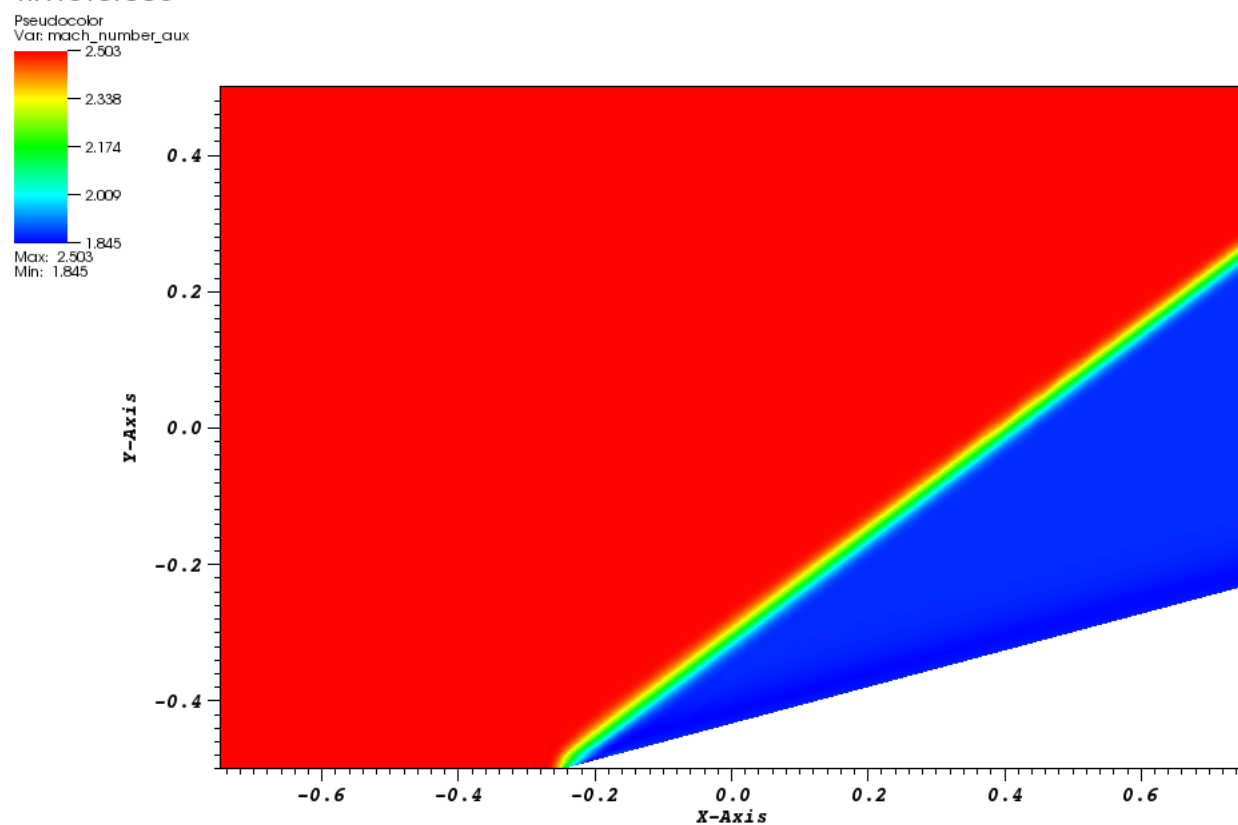
DB: CompressionCorner2DQuad\_high\_pressure\_out.e  
Time:0.00115



user: delchini  
Wed May 14 16:44:19 2014

Figure 3.16: Viscosity coefficient at  $t = 1.15 \times 10^{-3}$ .

DB: CompressionCorner2DQuad\_high\_pressure\_out.e  
Time:0.005

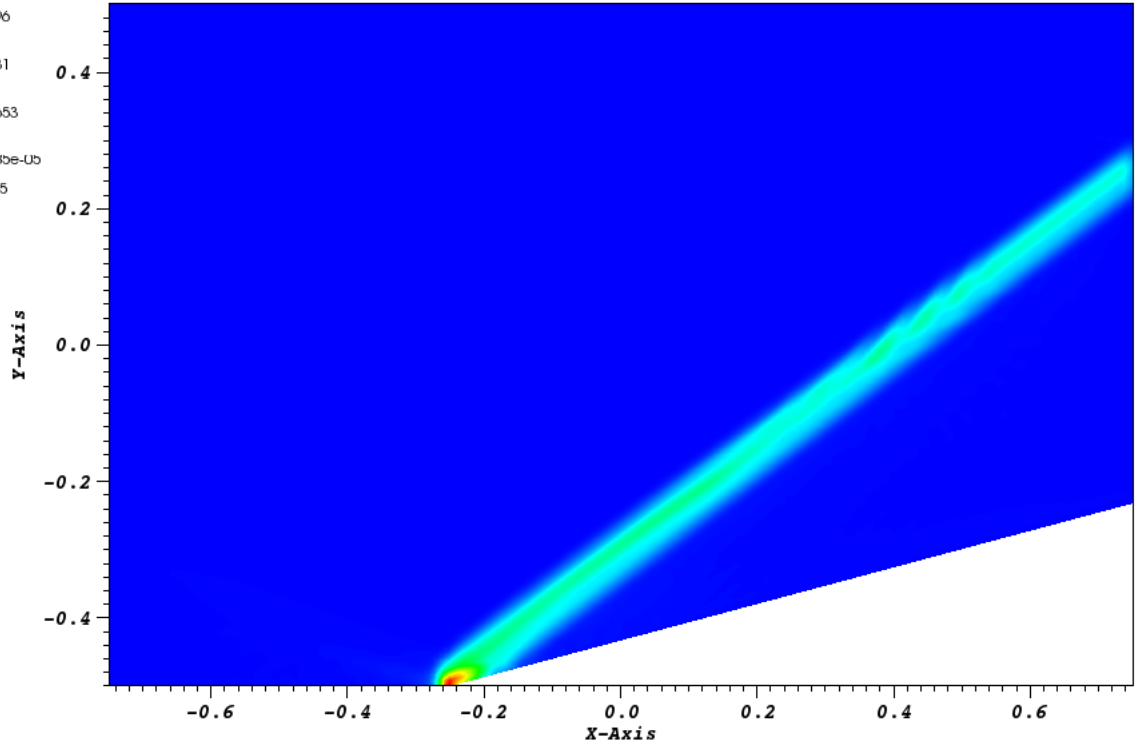


user: delchini  
Wed May 14 16:57:07 2014

Figure 3.17: Pressure solution at steady-state.

DB: CompressionCorner2DQuad\_high\_pressure\_out.e  
Time:0.005

Pseudocolor  
Var: kappa\_aux  
3.861  
2.896  
1.931  
0.9653  
1.185e-05  
Max: 3.861  
Min: 1.185e-05



user: delchini  
Wed May 14 16:57:36 2014

Figure 3.18: Viscosity coefficient at steady-state.

From the above figures, it is observed that the solution is formed of two regions of constant state. During the transient, the shock moves from the bottom wall to its steady-state solution. The same variations are observed in viscosity coefficient solution. At steady-state, the viscosity coefficient is large in the shock region and small anywhere else and thus, behaves as expected. At the corner of the edge at  $x = -0.25 \text{ m}$ , the viscosity coefficient is peaked because of the treatment of the wall boundary condition: at this particular node, the normal is not well defined and can

cause numerical errors.

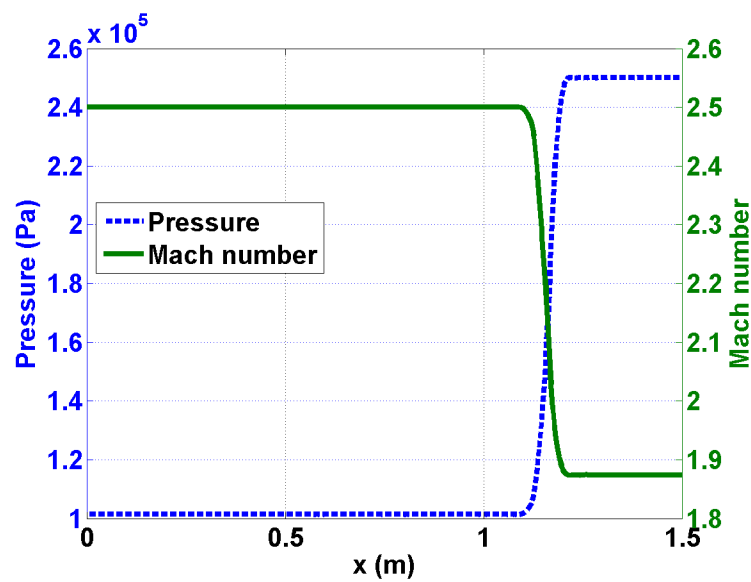


Figure 3.19: Pressure and Mach number profiles at steady-state



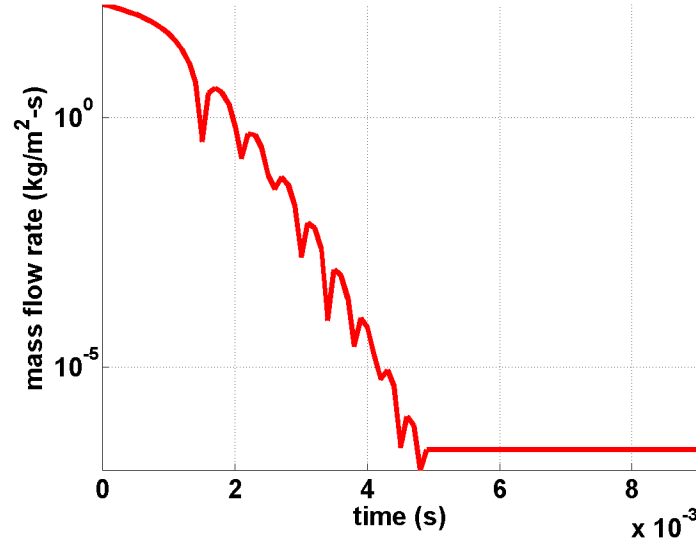


Figure 3.20: Difference between inlet and outlet mass flow rates as a function of time.

The 1-D plots of the pressure and the mach number at  $y = 0$ , are also given in Fig. 3.19: the shock does not show any spurious oscillations and is well resolved. Finally, the difference between the inlet and outlet mass flow rates is plotted in Fig. 3.20 and show that a steady-state is reached.

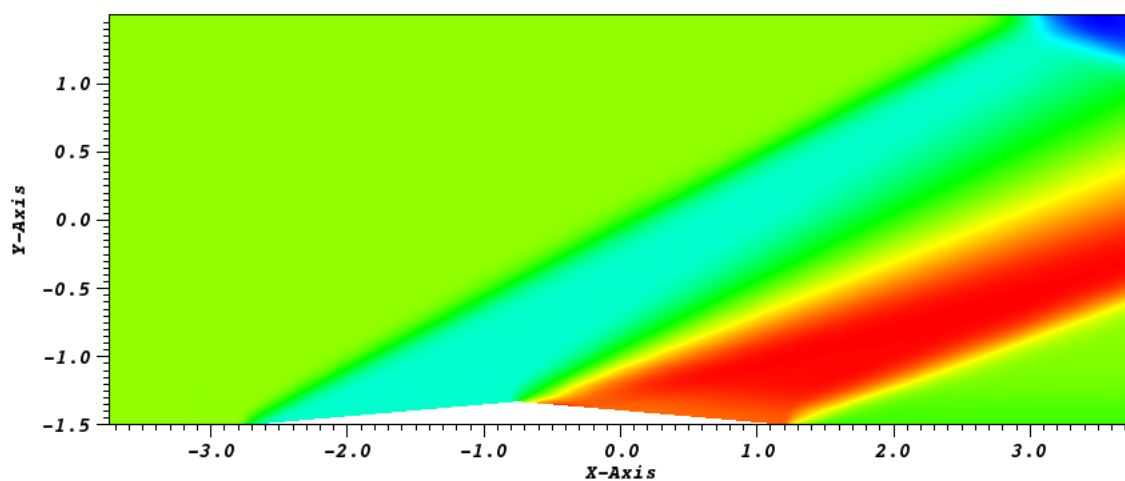
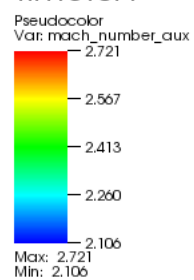
Overall, the numerical solution does not show any oscillations, match the analytical solution, and the shock is well resolved.

### 3.6.5 Supersonic flow over a $5^\circ$ double-wedge obstruction:

The last of the 2-D supersonic example that is proposed to study is a Mach2, 5 flow over a double-wedge obstruction located on the lower wall. The interesting feature of this test is that a steady-state is reached. The geometry used is shown in (FIG) and was discretized with 4000  $Q_1$  elements. The double wedge extends on the bottom boundary from  $x = 1$  to  $x = 5$  m. The top wall is located at  $y = 5$  m. A supersonic inlet boundary condition was set at the inlet by specifying the pressure,  $P = 101,325$

$Pa$ , the temperature,  $T = 300\ K$  and the vector velocity  $\vec{u} = (868.032, 0)\ m \cdot s^{-1}$ . The wall-boundary and supersonic outlet boundary conditions were implemented following the method described in (SECTION BCS). The second-order temporal integrator *BDF2* was used with a *CFL* of 5 to reach the steady-state that was detected by monitoring the norm of the total residual. The Ideal gas equation of state was used with an adiabatic constant  $\gamma = 1.4$  and a volumetric heat capacity  $C_v = 716.7\ J \cdot K^{-1}$  (air properties). The Mach number and viscosity coefficients profiles at steady-state are given in Fig. 3.21 and Fig. 3.22, respectively.

DB: DoubleWedgeObstruction\_out.e  
Time:0.1

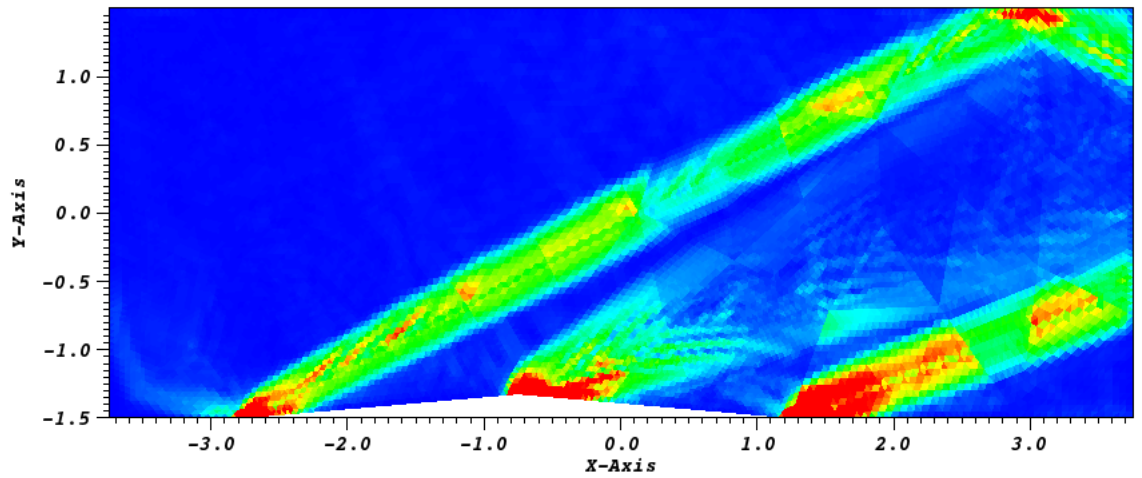


user: delchini  
Wed May 14 17:16:17 2014

Figure 3.21: Pressure solution at steady-state.

DB: DoubleWedgeObstruction\_out.e  
Time:0.1

Pseudocolor  
Var:  $\mu_{aux}$   
5.000  
3.751  
2.502  
1.254  
0.004772  
Max: 27.73  
Min: 0.004772



user: delchini  
Wed May 14 17:21:06 2014

Figure 3.22: Viscosity coefficient at steady-state.

The stay-state solution consists of a two shocks that form because of the interaction of the flow with the double wedge. The first wedge generates a shock that reflects on the top wall and then exits the computational domain: the interaction of the shock with the wall close to the outlet boundary requires a robust implementation of the boundary conditions and the stabilization method. The second shock is generated by the trailing wedge. In between the two shock regions, an expansion fan is formed.

### 3.7 2-D numerical results for subsonic flows:

#### 3.7.1 Subsonic flow over a 2-D cylinder

The flow of a fluid over a 2-D cylinder is a typical benchmark case to test the behavior of a numerical method in the low Mach regime. For this test, an analytical solution is available in the incompressible limit or low Mach limit (REFS) and often referred to as potential flow. The main features of the potential flow are the following:

- The solution is symmetric: the iso-mach number lines are used to assess the symmetry of the numerical solution.
- The velocity at the top of the cylinder is twice the incoming velocity set at the inlet.
- The pressure fluctuations are proportional to the inlet Mach number square, as follows:

$$\tilde{P} = \frac{\max(P) - \min(P)}{\max(P)} \propto M_\infty^2$$

where  $\tilde{P}$  and  $M_\infty$  are the pressure fluctuations and the inlet Mach number, respectively.

The computational domain consists of a  $1 \times 1$  square with a circular hole of radius 0.05 in its middle. At the inlet, a subsonic stagnation boundary condition is used: the stagnation pressure and temperature are computed using the following relations, valid for the Stiffened and Ideal gas equation of states:

$$\begin{cases} P_0 = P \left(1 + \frac{\gamma-1}{2} M^2\right)^{\frac{\gamma}{\gamma-1}} \\ T_0 = T \left(1 + \frac{\gamma-1}{2} M^2\right) \end{cases} \quad (3.33)$$

The static pressure  $P_s = 101325 \text{ Pa}$  is set at the subsonic outlet and a static pressure boundary type is used. The implementation of the pressure boundary conditions is done on the model of [37]. A solid wall boundary condition is set for the top and bottom walls of the computational domain: the normal velocity is zero since no mass can penetrate the solid body. The mesh is made of triangular cells.

The steady-state for Mach numbers ranging from  $M_\infty = 10^{-3}$  to  $M_\infty = 10^{-7}$  is shown in Fig. ???. The iso-Mach lines are drawn with 50 intervals ranging from  $10^{-8}$  to  $2M_\infty$ , and allow to assess the symmetry of the numerical solution.

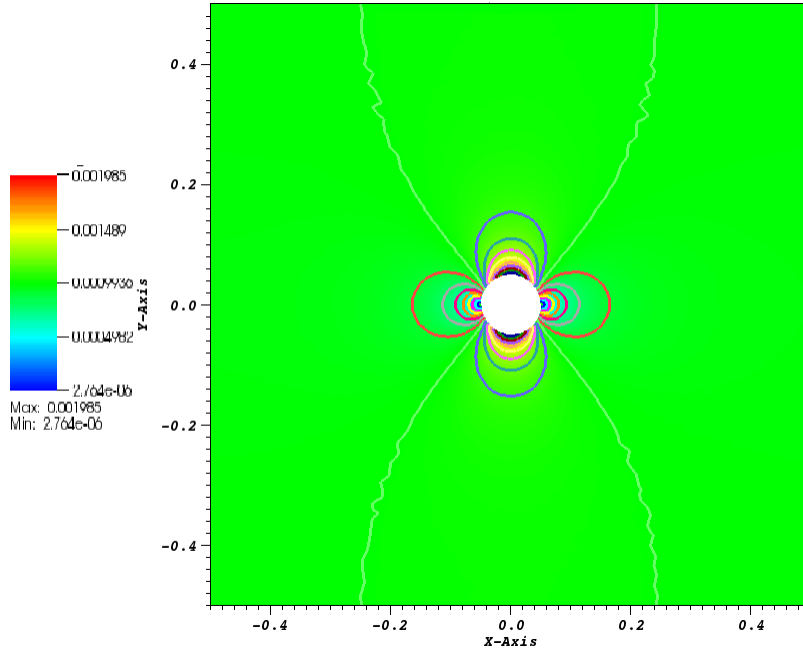


Figure 3.23: Steady-state solution at  $M_\infty = 10^{-3}$ .

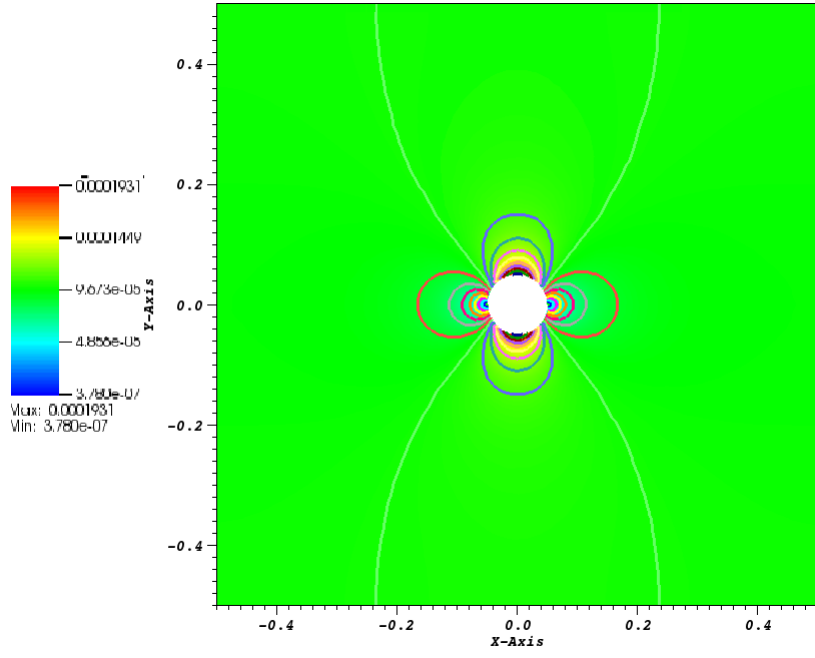


Figure 3.24: Steady-state solution at  $M_\infty = 10^{-4}$ .

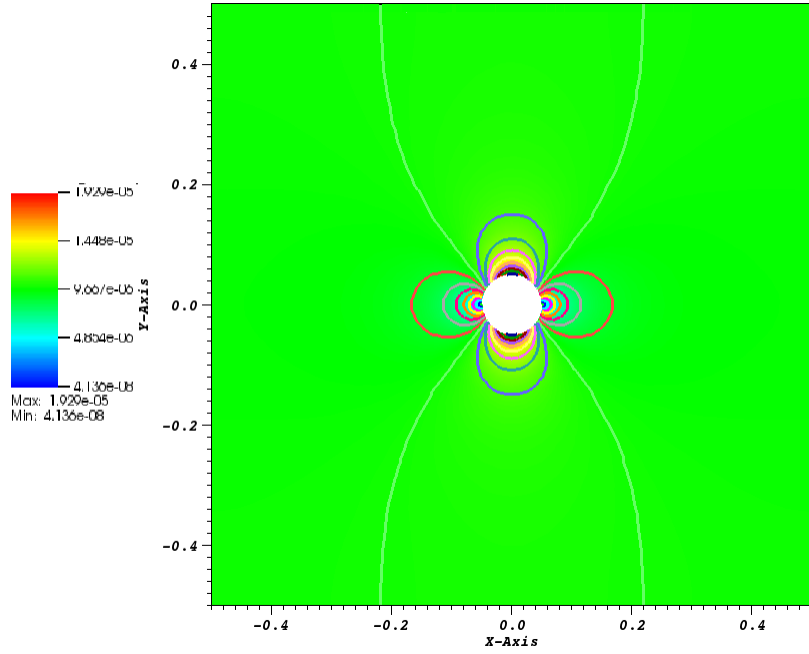


Figure 3.25: Steady-state solution at  $M_\infty = 10^{-5}$ .

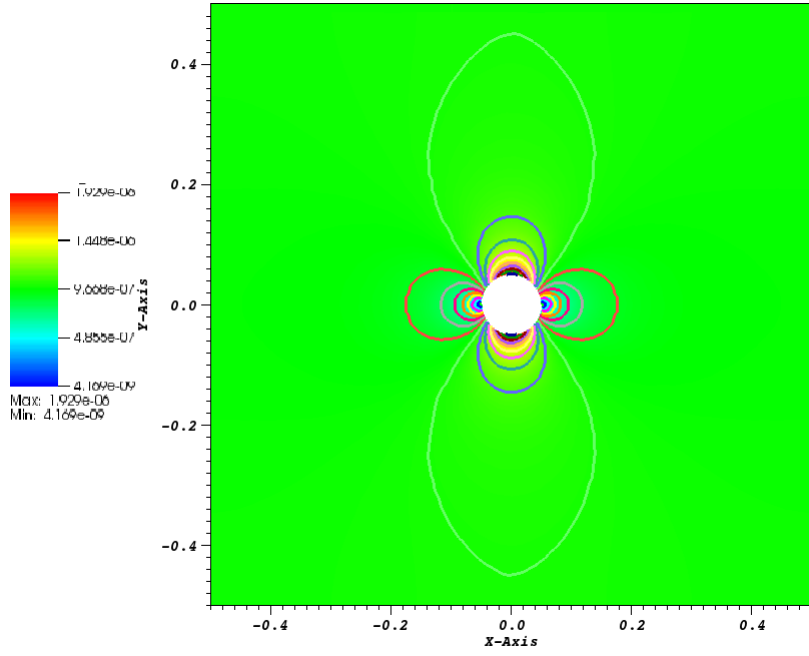


Figure 3.26: Steady-state solution at  $M_{\infty} = 10^{-7}$ .

In Table 3.13, the velocity at the top of the cylinder and at the inlet are given for the different values of the Mach number presented in Fig. ???. The ratio of the inlet velocity to the velocity at the top of cylinder is also computed and is very close to 2 as expected.



Table 3.13: Velocity ratio for different Mach numbers.

Mach number	inlet velocity	velocity at the top of the cylinder	ratio
$10^{-3}$	$2.348 \cdot 10^{-3}$	$1.176 \cdot 10^{-3}$	1.99
$10^{-4}$	$2.285 \cdot 10^{-4}$	$1.145 \cdot 10^{-4}$	1.99
$10^{-5}$	$2.283 \cdot 10^{-5}$	$1.144 \cdot 10^{-5}$	1.99
$10^{-6}$	$2.283 \cdot 10^{-6}$	$1.144 \cdot 10^{-6}$	1.99
$10^{-7}$	$2.283 \cdot 10^{-7}$	$1.144 \cdot 10^{-7}$	1.99

### 3.7.2 Subsonic flow over a 2-D hump

This is a another example of an internal flow configuration. It consist of a channel of height  $L = 1 \text{ m}$  and length  $3L$ , with a circular bump of length  $L$  and thickness  $0.1L$ . The bump is located on the bottom wall at a distance  $L$  from the inlet. The system is initialized with an uniform pressure  $P = 101325 \text{ Pa}$  and temperature  $T = 300 \text{ K}$ . The initial velocity is computed from the Mach number,  $M_\infty$ , the pressure, the temperature and the Ideal Gas equation of state with the heat capacity  $C_v = 717 \text{ J/kg} - \text{K}$  and the heat capacity ratio  $\gamma = 1.4$ . At the inlet, a subsonic stagnation boundary condition is used and the stagnation pressure and temperature are computed using Eq. (3.33). The static pressure  $P_s = 101325 \text{ Pa}$  is set at the subsonic outlet. An uniform grid is used to get the numerical solution until steady-state is reached. The results are shown in Fig. 3.27, Fig. 3.28, Fig. 3.29 and Fig. 3.30 for the inlet Mach numbers  $M_\infty = 0.7$ ,  $M_\infty = 0.01$ ,  $M_\infty = 10^{-4}$  and  $M_\infty = 10^{-7}$ , respectively. It is expected that, within the low Mach number range, the solution does not depend on the Mach number and is identical to the solution obtained with an incompressible flow code. On the other hand, for a flow at  $M = 0.7$ , the compressible

effects become more important and shock can form.

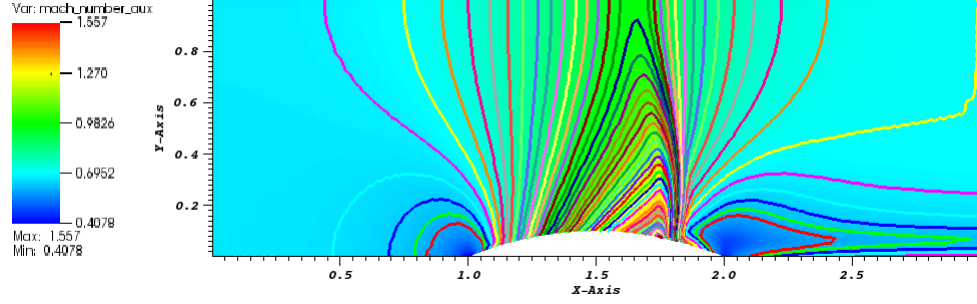


Figure 3.27: Mach 0.7: iso-Mach lines at steady-state.

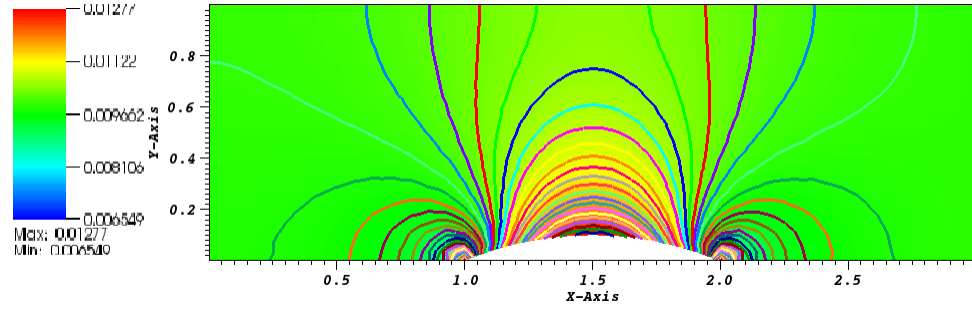


Figure 3.28: Mach  $10^{-2}$ : iso-Mach lines at steady-state.

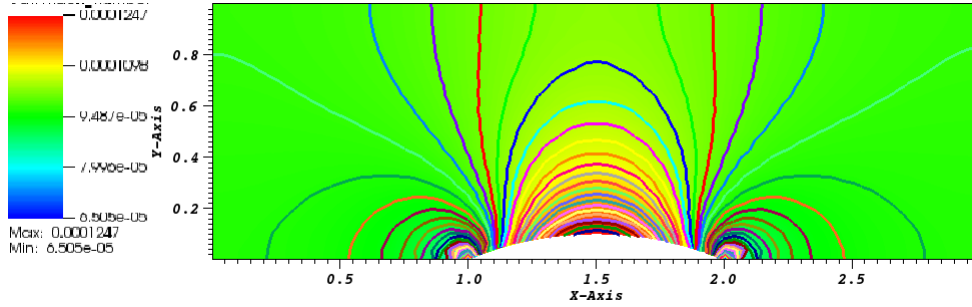


Figure 3.29: Mach  $10^{-5}$ : iso-Mach lines at steady-state.

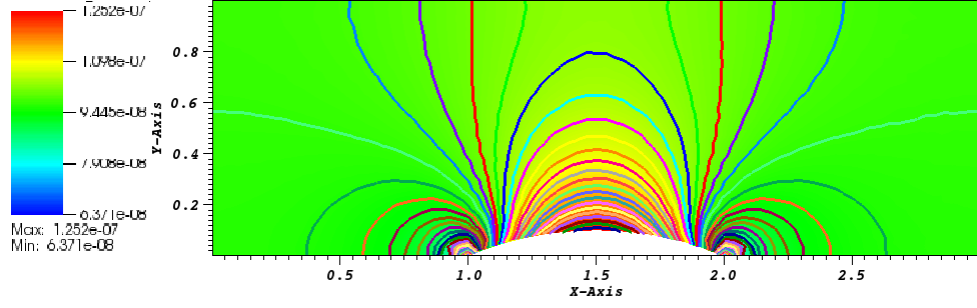


Figure 3.30: Mach  $10^{-7}$ : iso-Mach lines at steady-state.

The results showed in Fig. 3.28, Fig. 3.29 and Fig. 3.30 correspond to the low Mach regime. The iso-Mach lines are drawn ranging from the minimum and the maximum of each legend with 50 intervals. The steady-state solution is symmetric and does not depend on the value of the inlet Mach number as expected.

In Fig. 3.27, the steady-state numerical solution develops a shock: the compressibility effect are no longer negligible. The iso-Mach lines are also plotted with 50 intervals and ranging from 0.4 to 1.6. The shock is well resolved and does not display any instability or spurious oscillation.

The results presented in Fig. ?? were obtained with the new definition of the viscosity coefficient (see Eq. (3.20)), and, illustrate the capabilities of the entropy-viscosity method to adapt to the type of flow (subsonic and transonic flows) without using any tuning parameters, but by just evaluating the entropy residual that is an indicator of the entropy production.

### 3.8 Conclusions

A new version of the entropy viscosity method valid for a wide range of Mach number and applied to the multi-D Euler equations with variable area was derived and presented. The definition of the viscosity coefficient is now consistent with the

low Mach asymptotic limit, does not require an analytical expression of the entropy function, and thus, could be used with any equation of state having a convex entropy. Tests were performed with the Ideal and Stiffened Gas equation of states. In 1-D, convergence of the numerical solution (either smooth or with shocks) to the exact solution was demonstrated by computing the convergence rates of the L1 and L2 norms of the error for flows in convergence-divergent nozzle and a straight pipe. 2-D simulations were also performed for both subsonic and supersonic flows, and various geometries: the entropy viscosity method behaves well for a wide range of Mach number. The numerical results obtained for a flow over a circular bump (subsonic and transonic flows) illustrates the capabilities of the method to adapt to the flow type.

As future work, the entropy viscosity method will be extended to the 1-D seven equations model [37]. This two-phase flow system of equations is a good candidate for two reasons: it is unconditionally hyperbolic and degenerates to the multi-D Euler equations when one phase disappears.

4. APPLICATION OF THE ENTROPY VISCOSITY METHOD TO THE  
SEVEN EQUATIONS MODEL.

## 5. APPLICATION OF THE ENTROPY VISCOSITY METHOD TO THE 1-D GREY RADIATION-HYDRODYNAMIC EQUATIONS.

Text goes here.

### 5.1 Introduction

Solving the radiation hydrodynamic equations is a challenging task for multiple reasons. First, the characteristic time scales between the radiation and hydrodynamics are different by several orders of magnitude which often requires the radiation part to be solved implicitly to ensure stability. Second, as with any wave-dominated problems, high resolution schemes are needed to accurately resolve shocks. Third, achieving high-order accuracy is challenging but some recent developments provided high-order accuracy results both in time and space when discretizing either the Euler equations [17, 19, 20, 18] or the radiation equation independently from each other.

Significant effort has been put into developing Riemann solvers for both the radiation and hydrodynamic equations. Balsara [3] developed a Riemann solver for the radiation-hydrodynamic equations by considering the frozen approximation that decouples the two physics components. However, such an approach may be questionable in the equilibrium diffusion limit. In this case, the coupling terms drive the physics and have to be accounted for. A *generalized Riemann solver* that accounts exactly for the relaxation terms was developed in [3]. Another approach assumes the strong equilibrium diffusion limit in which radiation diffusion is negligible and the radiation simply advects at the material velocity [10]. In this limit, the radiation hydrodynamics equation can be expressed in the form of the Euler equations with a radiation-modified equation of state (REOS) . Any solution technique for the Euler equations may be applied to these equations. Thus, one may develop approximate

Riemann solvers for these equations and applied them in a general context.

Edwards and al. [21] proposed a two-stage semi-implicit IMEX scheme to solve the coupled radiation-hydrodynamic equations. They applied a Trapezoidal/BDF2 temporal discretization scheme to the nonlinear grey radiation diffusion. The radiation and hydrodynamic equations are solved implicitly and explicitly, respectively. A Riemann solver along with a flux limiter is used to resolve shocks and other waves. Their results show good agreement with semi-analytical solutions.

In this article we propose to solve the 1-D radiation-hydrodynamics equations by using *the entropy viscosity method*. This technique, developed by Guermond et al. for hyperbolic systems of equations [19, 20], consists in adding appropriate dissipative terms to the governing equations. The viscosity coefficient of these terms is modulated by the local entropy production. These dissipative terms are devised to stabilize the numerical scheme and to remove the non-physical oscillations appearing at the shock locations. Generally speaking, entropy is produced at shocks [41]. Thus, by setting the viscosity coefficient proportional to the entropy production, shocks can be detected and tracked and an adequate amount of viscosity is added locally to stabilize the numerical scheme. The entropy production is computed on the fly, by analyzing the entropy residual. This residual is strongly peaked in shocks and small elsewhere. The entropy viscosity method was shown to achieve high-order accuracy away from the shock regions, was successfully applied to non-linear hyperbolic equations using various discretization methods (finite volume, continuous and discontinuous finite elements, spectral method) and yielded high-order accuracy on non-uniform meshes and complex geometries [20, 43]. Because of the similarity between Euler equations and the radiation hydrodynamic equations, it is conjectured that the entropy viscosity method may be a good candidate for resolving shocks occurring in radiation-hydrodynamic phenomena.

The 1-D grey radiation-hydrodynamic (GRH) equations are recalled in Eq. (5.1):

$$\left\{ \begin{array}{l} \partial_t (\rho) + \partial_x (\rho u) = 0 \\ \partial_t (\rho u) + \partial_x (\rho u^2 + P + \frac{\epsilon}{3}) = 0 \\ \partial_t (\rho E) + \partial_x [u (\rho E + P)] = -\frac{u}{3} \partial_x \epsilon - \sigma_a c (aT^4 - \epsilon) \\ \partial_t \epsilon + \frac{4}{3} \partial_x (u \epsilon) = \frac{u}{3} \partial_x \epsilon + \partial_x \left( \frac{c}{3\sigma_t} \partial_x \epsilon \right) + \sigma_a c (aT^4 - \epsilon) \end{array} \right. , \quad (5.1)$$

where  $\rho$ ,  $u$ ,  $E$ ,  $\epsilon$ ,  $P$  and  $T$  are the material density, material velocity, material specific total energy, radiation energy density, material pressure and temperature, respectively. The total and absorption cross sections,  $\sigma_t$  and  $\sigma_a$ , are either constant or density- and temperature-dependent. The variables  $a$  and  $c$  are the Boltzman constant and the speed of light, respectively. Lastly, the symbols  $\partial_t$  and  $\partial_x$  denote the temporal and spatial partial derivatives, respectively. The material temperature and pressure are computed with the Ideal Gas equation of state (IGEOS):

$$\left\{ \begin{array}{l} P = (\gamma - 1) C_v \rho T \\ e = C_v T \end{array} \right. , \quad (5.2)$$

where  $e$  is the specific internal energy and is obtained from the expression  $e = E - 0.5u^2$ . The heat capacity  $C_v$  and the heat ratio coefficient  $\gamma$  are assumed constant.

The objective of this paper is to extend the entropy-based viscosity method to the 1-D grey radiation-hydrodynamic equations. The approach followed in this paper is similar to those of [3, 38]: an infinite opacity is assumed and the relaxation terms are ignored in order to make Eq. (5.1) hyperbolic. Then, an entropy equation is derived and used to obtain the functional forms of the viscous stabilization terms. Definitions for the viscosity coefficients are provided.

This paper is organized as follows. In Section 5.2, the entropy viscosity method is



extended to the grey radiation-hydrodynamic equations; details regarding the derivation of the adequate dissipative terms and definitions for the new viscosity coefficients are provided. Spatial and temporal discretization schemes are discussed in Section 5.3 along with the solution algorithm employed to solve the discretized equations. Numerical results are presented in Section 5.4 where the second-order accuracy of the scheme is demonstrated in both the equilibrium diffusion and streaming limits, using the method of manufactured solutions applied to the GRH equations. Then, several numerical test cases, taken from the published literature, are provided; in these simulations, the Mach number varies from 1.05 to 50 [36]. Conclusions are presented in Section 5.5.

## 5.2 The entropy-based viscosity method applied to the 1-D

### Radiation-Hydrodynamic equations

In this section, we extend the entropy viscosity method [19, 20, 43] to the 1-D radiation-hydrodynamic equations in a staged process. First, the reader is guided through the main steps that lead to the derivation of the dissipative terms, using the entropy minimum principle [40]. Then, a definition for the entropy viscosity coefficient based upon the entropy production is given.

We recall that the entropy viscosity method was developed for hyperbolic system of equations. However, the radiation hydrodynamic equations are not strictly hyperbolic but several numerical techniques are based on the study of their hyperbolic parts [3, 38]. Thus, following the same rationale, the system of equations given in Eq. (5.1) is made hyperbolic by assuming an infinite opacity (the frozen approximation) and by ignoring the relaxation terms. These two assumptions yield the

following system of equations:

$$\begin{cases} \partial_t (\rho) + \partial_x (\rho u) = 0 \\ \partial_t (\rho u) + \partial_x (\rho u^2 + P + \frac{\epsilon}{3}) = 0 \\ \partial_t (\rho E) + \partial_x [u (\rho E + P)] = -\frac{u}{3} \partial_x \epsilon \\ \partial_t \epsilon + \frac{4}{3} \partial_x (u \epsilon) = \frac{u}{3} \partial_x \epsilon \end{cases} . \quad (5.3)$$

The jacobian matrix of the hyperbolic terms can be computed to derive the eigenvalues:

$$\lambda_1 = u - c_m, \lambda_{2,3} = u \text{ and } \lambda_4 = u + c_m, \quad (5.4)$$

where  $c_m$  is the radiation-modified material speed of sound and is defined as follows:

$$c_m^2 = P_\rho + \underbrace{\frac{P}{\rho^2} P_e}_{c_{Euler}^2} + \frac{4\epsilon}{9\rho} \quad (5.5)$$

with  $P_x$  the standard shorthand notation for  $\partial_x P$ , and  $c_{Euler}^2$  denotes the definition of the speed of sound when considering only the 1-D Euler equations. The above hyperbolic system of equations can be recast in a conservative form. This allows us to assume the existence of an entropy function  $s$  [26] that depends upon the internal energy  $e$ , the density  $\rho$ , and the radiation energy density  $\epsilon$ . Following some algebra given in Appendix ??, an equation satisfied by the entropy  $s$  is obtained:

$$\rho \frac{ds}{dt} = \rho (\partial_t s + u \partial_x s) = 0, \quad (5.6)$$

where  $\frac{d}{dt}$  denotes the total or material derivative. Eq. (5.6) is often referred as the entropy residual and is used to prove the entropy minimum principle,  $\frac{ds}{dt} \geq 0$ , [40].

When adding dissipative terms to each equation of Eq. (5.3) as required in the

entropy viscosity method, the entropy residual equation is modified and some additional terms will appear in the right-hand side of Eq. (5.6). The sign of these extra terms needs to be studied for the entropy minimum principle to hold. As such, the entropy minimum principle is invoked to guide in the derivation of appropriate expressions for each of the dissipative terms. Obtaining the final expression of the dissipative terms is a lengthy process and only the final result along with the key assumptions are stated here. The reader is referred to Appendix ?? for the details of the derivation. The system of equations with the dissipative terms is as follows:

$$\left\{ \begin{array}{l} \partial_t (\rho) + \partial_x (\rho u) = \partial_x (\kappa \partial_x \rho) \\ \partial_t (\rho u) + \partial_x (\rho u^2 + P + \frac{\epsilon}{3}) = \partial_x (\kappa \partial_x \rho u) \\ \partial_t (\rho E) + \partial_x [u (\rho E + P)] + \frac{u}{3} \partial_x \epsilon = \partial_x (\kappa \partial_x (\rho E)) \\ \partial_t \epsilon + \frac{4}{3} \partial_x (u \epsilon) - \frac{u}{3} \partial_x \epsilon = \partial_x (\kappa \partial_x \epsilon) \end{array} \right. , \quad (5.7)$$

where  $\kappa$  is a locally defined positive viscosity coefficient. It was assumed that the following conditions hold:

$$\left\{ \begin{array}{l} P \frac{\partial s}{\partial e} + \rho^2 \frac{\partial s}{\partial \rho} + \frac{4}{3} \rho \epsilon \frac{\partial s}{\partial \epsilon} = 0 \\ s(\rho, e, \epsilon) = \hat{s}(\rho, e) + \frac{\rho_0}{\rho} \tilde{s}(\epsilon) \end{array} \right. \quad (5.8)$$

where  $-\tilde{s}$  is convex with respect to the radiation energy density  $\epsilon$  and  $-\hat{s}$  is convex with respect to the internal energy  $e$  and the specific volume  $\rho^{-1}$ . The constant  $\rho_0$  is of order one and appears only for dimensionality purposes.

Once the dissipative terms are obtained, it remains to define the local viscosity coefficient  $\kappa(x, t)$ . We require the following to hold in the prescription for  $\kappa$ :

- Since the entropy residual is a measure of the entropy production that occurs in shock regions, it is natural to define a viscosity coefficient proportional to

the entropy residual. This will enable shock detection and tracking and will also provide a measure of the viscosity required to stabilize the scheme. This viscosity coefficient is referred to as the *entropy viscosity coefficient* or *second-order viscosity coefficient* and is denoted by  $\kappa_e(x, t)$ .

- An upper bound on  $\kappa$  is to be set since entropy production can be very large in shocks. For explicit time integration, the maximum value of the viscosity coefficient is related to the Courant-Friedrichs-Lewy number (CFL). The upper bound on  $\kappa$  is defined by analogy to the standard upwind (Godunov) scheme that is known to efficiently smooth out oscillations (but is only first-order accurate). With implicit temporal integrators, the same reasoning is used even if the CFL number may not need to be strictly respected. This upper bound will be referred to as the *first-order viscosity*, denoted by  $\kappa_{max}(x, t)$ .
- The viscosity coefficient  $\kappa$  that is actually used in the dissipative terms of Eq. (5.3) is defined as follows:  $\kappa(x, t) = \min(\kappa_e(x, t), \kappa_{max}(x, t))$ . With such a definition, the viscosity added to the system of equations will saturate to the first order viscosity in the shock regions. Elsewhere, the entropy production and thus the viscosity coefficient  $\kappa$  are expected to be small.

Next, we define the local first- and second-order viscosity coefficients  $\kappa_{max}(x, t)$  and  $\kappa_e(x, t)$ , respectively. Following the work of Zingan et al. [43], the first-order viscosity definition is based on the local largest eigenvalue that is known to be  $|u| + c_m$  in 1-D:

$$\kappa_{max} = \frac{h}{2} (|u| + c_m) \quad (5.9)$$

where  $h$  is the local grid size. This definition is derived based on the upwind scheme and a simple derivation can be found in [19] in the case of a scalar hyperbolic equa-

tion. Through the definition of the radiation-modified speed of sound  $c_m$ , both the material and radiation properties are accounted for in the definition of the first-order viscosity coefficient.

The definition of the second order viscosity coefficient  $\kappa_e(x, t)$  is based upon the entropy residual (Eq. (5.6)) recast as a function of pressure  $P$ , density  $\rho$  and radiation energy density  $\epsilon$ :

$$\tilde{D}_e(x, t) = \frac{s_e}{P_e} \underbrace{\left( \frac{dP}{dt} - c_{Euler}^2 \frac{d\rho}{dt} \right)}_{\hat{D}_e(x, t)} \quad (5.10)$$

The term  $s_e$  is the inverse of the material temperature (Appendix ??) and  $P_e$  is computed from the IGEOS. These two terms are positive so that the sign of the entropy residual  $\tilde{D}_e(x, t)$  can be determined by simply inspecting the terms inside the parentheses, denoted by  $\hat{D}_e(x, t)$ . Such an expression is easier to compute than the one given in Eq. (5.6) which required an analytical expression for the entropy function. In addition to the entropy residual, inter-element jumps in the pressure and density gradients,  $J$ , are also accounted for. The objective is to be able to also detect discontinuities that are not shocks, such as contact waves (there is no entropy production in a contact wave), in order to stabilize them as well.

Thus, the entropy viscosity coefficient  $\kappa_e(x, t)$  is set to be proportional to  $\hat{D}_e(x, t)$  and  $J$  with the following form:

$$\kappa_e(x, t) = h^2 \frac{\max(|\hat{D}_e(x, t)|, J)}{n_P} \quad (5.11)$$

where  $J = \max_i(J(x_i, t))$ , and  $J(x_i, t)$  is the jump of a given quantity at cell interface  $x_i$ , and  $n_P$  is a normalization function (of the same units as pressure) that has to be chosen so that the viscosity coefficient  $\kappa$  has units of  $m^2/s$ . The following definition for the normalization function has been chosen:  $n_P = \rho c_m^2$ . Thus, the final definition

for the viscosity coefficient  $\kappa$  is the following:

$$\kappa_e(x, t) = h^2 \frac{\max(|\hat{D}_e(x, t)|, J)}{\rho c_m^2} \quad (5.12)$$

The jump  $J$  in the definition of  $\kappa(x, t)$  is piecewise-constant. Its definition is discretization-dependent and defined as follows for Continuous Galerkin FEM:

$$\begin{cases} J_P(x_i, t) = |u|[[\partial_x P]] \\ J_\rho(x_i, t) = c_m^2 |u|[[\partial_x \rho]] \\ J(x_i, t) = \max(J_\rho(x_i, t), J_P(x_i, t)) \end{cases} \quad (5.13)$$

The symbol  $[[\cdot]]$  denotes the jump at the cell interface.

The entropy viscosity method is now well defined for the hyperbolic system given in Eq. (5.3) and will be used to solve for the grey radiation-hydrodynamic equations given in Eq. (5.1). However, one may question how the relaxation source terms,  $\sigma_a c(aT^4 - \epsilon)$  and the physical diffusion term,  $\partial_x(D\partial_x \epsilon)$ , may affect the entropy viscosity method. When applying the entropy viscosity method, the radiation energy density equation will now contain a diffusive term and a numerical dissipative term with a vanishing viscosity coefficient  $\kappa$ . As long as the diffusive coefficient  $D = \frac{c}{3\sigma_t}$  is larger than the viscosity coefficient  $\kappa$ , the numerical dissipative term should not be required. A way to ensure consistency and prevent the formation of oscillations in the frozen limit is to merge the two second-order derivative terms into one as follows:

$$\partial_x \left( \frac{c}{3\sigma_t} \partial_x \epsilon \right) + \partial_x (\kappa \partial_x \epsilon) \implies \partial_x \left[ \max \left( \frac{c}{3\sigma_t}, \kappa \right) \partial_x \epsilon \right] \quad (5.14)$$

Thus, as long as the artificial viscosity coefficient  $\kappa$  is locally smaller than the physical diffusive coefficient  $D = \frac{c}{3\sigma_t}$ , no artificial viscosity is required to ensure stability of

the numerical scheme. As the diffusive coefficient  $D$  goes to zero, shocks can form in the radiation energy density profile and will require a certain amount of viscosity in order to prevent oscillations from appearing.

The effect of the relaxation source terms onto the entropy viscosity method can become problematic in the equilibrium diffusion limit ( $\sigma_a c \rightarrow \infty$ ): the relaxation source terms behave as dissipative terms and make the system parabolic [18]. In [22], a study on the impact of various artificial viscosity methods onto hyperbolic systems with relaxation terms was carried out. It was shown that high-order viscosity coefficients are more suitable since they do not alter the physical solution as much as first-order viscosity terms (upwind scheme). A manufactured solution is employed in Section 5.4.1 to test the convergence of the numerical solution in the equilibrium-diffusion limit. The normalization factor has to be larger than  $h$  in order to conserve high-order accuracy.

The reader will notice that, except for the definition of the jumps, the whole method is independent of the spatial discretization employed. The technique could be used with discontinuous Galerkin finite element or finite volume methods. In both cases, an adequate definition of the jump terms can be found in [43].

### 5.3 Numerical scheme and solution technique

The 1-D radiation-hydrodynamic equations Eq. (5.1) are discretized with the continuous Galerkin finite element method (CGFEM) under the MOOSE framework [9]. To obtain a weak form, the following generic form of Eq. (5.1) is considered:

$$\partial_t U + \partial_x F(U) = S + \partial_x H(U) \quad (5.15)$$

where  $U$  is the solution vector,  $F$  is a conservative vector flux,  $S$  is a vector containing the relaxation source terms and non-conservative terms, and  $H$  is the artificial

viscosity dissipative flux:

$$U = \begin{bmatrix} \rho \\ \rho u \\ \rho E \\ \epsilon \end{bmatrix}, \quad F(U) = \begin{bmatrix} \rho u \\ \rho u^2 + P + \frac{\epsilon}{3} \\ u(\rho E + P) \\ \frac{4}{3}u\epsilon \end{bmatrix}, \quad S = \begin{bmatrix} 0 \\ 0 \\ -\frac{u}{3}\partial_x\epsilon - \sigma_a c(aT^4 - \epsilon) \\ \frac{u}{3}\partial_x\epsilon + \partial_x\left(\frac{c}{3\sigma_t}\partial_x\epsilon\right) + \sigma_a c(aT^4 - \epsilon) \end{bmatrix},$$

$$\text{and } H(U) = \begin{bmatrix} \kappa\partial_x\rho \\ \kappa\partial_x(\rho u) \\ \kappa\partial_x(\rho e) + \frac{u^2}{2}\kappa\partial_x\rho + \rho u\mu\partial_x u \end{bmatrix}$$

In order to apply the continuous finite element method, Eq. (5.15) is multiplied by a test function  $\phi$ , integrated by parts over the discrete mesh  $\Omega$  bounded by  $\partial\Omega$ , to obtain a weak solution:

$$\sum_e \int_e \partial_t U \phi - \sum_e \int_e F(U) \partial_x \phi + \int_{\partial\Omega} F(U) \mathbf{n} \phi - \sum_e \int_e S \phi + \sum_e \int_e H(U) \partial_x \phi - \int_{\partial\Omega} H(U) \mathbf{n} \phi = 0 \quad (5.16)$$

where  $e$  represents the cells of  $\Omega$  and  $\mathbf{n}$  is the outward normal vector to the boundary of the computational domain.

The integrals over the elements  $e$  are evaluated using third-order Gauss quadrature rules. The time-dependent term will be evaluated using the implicit second-order temporal integrator BDF2 [18]. Only linear test functions are considered in this paper. The integral on  $\partial\Omega$  requires computation of the flux  $F(U)$  and  $H(U)$  on the boundary. It is chosen to treat the boundary for each physics component independently and details will be given in Section 5.4.2 on how to compute  $F(U)$ . The viscosity dissipative flux  $H(U)$  is zero on the boundaries since the viscosity



coefficients  $\kappa$  and  $\mu$  are set to zero [19, 20, 43].

The Jacobian-Free Newton Krylov method [23] is employed to solve the system for each time step: Newton’s and Krylov methods are used for the outer nonlinear and inner linear solves, respectively. The full Jacobian matrix is used as a preconditioner and is computed by finite difference: this is one of the options available in MOOSE and is reasonably efficient for 1-D simulations.

The entropy residual expression is not integrated over the cell volume as it is usually done in the Galerkin finite element method. The variable values and their gradients are available at quadrature points and at different times, and, thus, can be used to evaluate the entropy residual.

## 5.4 Numerical results

In this section, numerical results using the entropy viscosity method are presented for the dimensional 1-D grey radiation-hydrodynamic equations. First, second-order accuracy of the method is demonstrated using the method of manufactured solution (MMS). Then, results for some standard radiation-hydrodynamic test cases are given.

### 5.4.1 *Space/time accuracy*

The same manufactured solution as in [21] is used in order to test both the diffusive and streaming limit solutions in a slab of thickness  $L = 2\pi \text{ cm}$ . The manufactured solutions are composed of trigonometric functions. Periodic boundary conditions are used for all of the variables. The  $L_2$  norm of the error between the numerical and exact solutions are computed for density, momentum, total material energy, and radiation energy density. For each new simulation, the time step is divided by two and the number of spatial degrees of freedom is doubled. With such settings, the error is expected to decrease by a factor 4 if second-order convergence is achieved.

The first manufactured solution is designed to test the equilibrium-diffusion limit. In that case, the radiation energy is in equilibrium with the material temperature and the opacity is large which means that the radiation mean-free path is not resolved but the variation of the solution is resolved. The following exact solution was used:

$$\left\{ \begin{array}{l} \rho = \sin(x - t) + 2 \\ u = \cos(x - t) + 2 \\ T = \frac{0.5\gamma(\cos(x-t)+2)}{\sin(x-t)+2} \\ \epsilon = aT^4 \end{array} \right. . \quad (5.17)$$

The cross sections  $\sigma_a$  and  $\sigma_t$  are assumed constant and set to the same value  $1000 \text{ cm}^{-1}$ . The simulation is run until  $t = 3 \text{ sh}$  ( $1 \text{ sh} = 10^{-8} \text{ sec}$ ). The  $L_2$  error norm along with its ratio between consecutive simulations are given in Table 5.1 for the equilibrium diffusion limit case.

Table 5.1:  $L_2$  norms of the error for the equilibrium diffusion limit case using a manufactured solution.

# of cells	time step size ( $sh$ )	$\rho$	ratio	$\rho E$	ratio
20	$10^{-1}$	0.590766	NA	1.333774	NA
40	$5 \cdot 10^{-1}$	0.290626	2.03	0.478819	2.79
80	$2.5 \cdot 10^{-2}$	0.0959801	3.021	0.154119	3.11
160	$1.25 \cdot 10^{-2}$	0.02593738	3.70	0.0405175	3.80
320	$6.25 \cdot 10^{-3}$	$6.471444 \cdot 10^{-3}$	4.00	$9.90446 \cdot 10^{-3}$	4.09
640	$3.125 \cdot 10^{-3}$	$1.584158 \cdot 10^{-3}$	4.01	$2.44727 \cdot 10^{-3}$	4.04
# of cells	time step size ( $sh$ )	$\epsilon$	ratio	$\rho u$	ratio
20	$10^{-1}$	0.00650085	NA	0.910998	NA
40	$5 \cdot 10^{-1}$	0.00124983	5.20	0.4090946	2.23
80	$2.5 \cdot 10^{-2}$	0.000262797	4.76	0.125943	3.25
160	$1.25 \cdot 10^{-2}$	$6.17726 \cdot 10^{-5}$	4.25	$3.381042 \cdot 10^{-3}$	3.72
320	$6.25 \cdot 10^{-3}$	$1.509184 \cdot 10^{-5}$	4.09	$8.373657 \cdot 10^{-3}$	4.04
640	$3.125 \cdot 10^{-3}$	$3.72548 \cdot 10^{-6}$	4.05	$2.070538 \cdot 10^{-3}$	4.04

The second manufactured solution is used to test the method in the streaming limit: the radiation streaming dominates the absorption/re-emission term and

evolves at a fast time scale. The exact solution used is as follows :

$$\left\{ \begin{array}{l} \rho = \sin(x - t) + 2 \\ u = (\sin(x - t) + 2)^{-1} \\ T = 0.5\gamma \\ \epsilon = \sin(x - 1000t) + 2 \end{array} \right. \quad (5.18)$$

For this manufactured solution, the cross sections are still assumed constant and set to the same value  $1 \text{ cm}^{-1}$ . The final time is  $t_{final} = 3 \text{ sh}$ . Once again, the  $L_2$  error norm is given in Table 5.2 for the density, momentum, material total energy and radiation energy density.

Table 5.2:  $L_2$  norms of the error for the streaming limit case using a manufactured solution.

# of cells	time step size ( $sh$ )	$\rho$	ratio	$\rho E$	ratio
20	$10^{-1}$	$1.4373 \cdot 10^{-2}$	NA	$5.88521 \cdot 10^{-1}$	NA
40	$5 \cdot 10^{-2}$	$3.760208 \cdot 10^{-3}$	3.82	$1.4244 \cdot 10^{-1}$	4.13
80	$2.5 \cdot 10^{-2}$	$9.91724 \cdot 10^{-4}$	3.79	$3.2047 \cdot 10^{-2}$	4.44
160	$1.25 \cdot 10^{-2}$	$2.4455 \cdot 10^{-4}$	4.06	$7.4886 \cdot 10^{-3}$	4.28
320	$6.25 \cdot 10^{-3}$	$6.280715 \cdot 10^{-5}$	3.89	$1.82327 \cdot 10^{-3}$	4.11
640	$3.125 \cdot 10^{-3}$	$1.57920 \cdot 10^{-5}$	3.98	$4.50463 \cdot 10^{-4}$	4.05
1280	$1.5625 \cdot 10^{-4}$	$3.96096 \cdot 10^{-6}$	3.99	$1.12061 \cdot 10^{-4}$	4.02
# of cells	time step size ( $sh$ )	$\epsilon$	ratio	$\rho u$	ratio
20	$10^{-1}$	$3.82001 \cdot 10^{-1}$	NA	$2.354671 \cdot 10^{-3}$	NA
40	$5 \cdot 10^{-2}$	$1.21500 \cdot 10^{-1}$	3.14	$6.138814 \cdot 10^{-4}$	3.84
80	$2.5 \cdot 10^{-2}$	$3.27966 \cdot 10^{-2}$	3.70	$1.74974 \cdot 10^{-4}$	3.51
160	$1.25 \cdot 10^{-2}$	$8.38153 \cdot 10^{-3}$	3.91	$3.61297 \cdot 10^{-5}$	4.84
320	$6.25 \cdot 10^{-3}$	$2.10925 \cdot 10^{-3}$	3.97	$9.03866 \cdot 10^{-6}$	3.99
640	$3.125 \cdot 10^{-3}$	$5.28472 \cdot 10^{-4}$	3.99	$2.25649 \cdot 10^{-6}$	4.01
1280	$1.5625 \cdot 10^{-4}$	$1.322268 \cdot 10^{-4}$	3.99	$5.69984 \cdot 10^{-7}$	3.95

For both manufactured solutions the error is divided by four as the time step and the spatial mesh are reduced by a factor two. Thus, we conclude that GRH equations can be numerically solved with second-order accuracy using the entropy viscosity method when the exact solution is smooth.

#### 5.4.2 Radiation shock simulations

The purpose of this section is to show that the entropy-based viscosity method (Section 5.2) can accurately resolve shocks occurring in radiation-hydrodynamic simulations. Multiple test cases are considered, with Mach numbers of 1.05, 1.2, 2, 5 and 50 [36]. All of the simulations are run with 500 spatial cells and with a Courant-Friedrichs-Lewy (CFL number) of 10 until steady-state (even if the scheme employed here is fully implicit, a CFL number can still be computed and is a good reference for comparison against semi-implicit or fully explicit codes). Linear Lagrange polynomials and the second-order temporal integrator BDF2 are once again used. For clarity, the initial conditions for each test case will be recalled in a table and plots of the density,  $\rho(x)$ , the radiation temperature,  $\theta(x)$ , and material temperature,  $T(x)$ , at steady-state will be given as well as those of the viscosity coefficients,  $\kappa(x)$  and  $\kappa_{max}(x)$ . The computational domain consists of a 1-D slab of thickness  $L$ . The initial discontinuity between the left and right states is located at  $x_0$  and will be specified for all test cases. For all of the test cases presented in this paper, the cross sections  $\sigma_a$  and  $\sigma_t$  are assumed constant and set to  $853.144 \text{ cm}^{-1}$  and  $390.711 \text{ cm}^{-1}$ , respectively, if not otherwise specified. The heat capacity at constant specific volume is set to  $C_v = 0.12348 \text{ jerks}/(g - \text{keV})$ .

For the Mach 2 simulation, results will also be shown when employing only the first-order viscosity ( $\kappa(x, t) = \kappa_{max}(x, t)$ ) in order to show the benefits of using a high-order viscosity coefficient.

The inlet and outlet boundary conditions (BCs) are given next. The Euler equations and radiation equation are considered independently since the latter one is parabolic. At the inlet, the flow is supersonic and, therefore, no physical information exits the system. Thus, Dirichlet boundary condition can be used. At the outlet,

the flow become subsonic which requires a particular treatment. Following the work from [37], a static boundary condition is implemented. Only the back pressure is provided and the other variables are computed using the characteristic equations. For the radiation equation, vacuum boundary conditions are used at both inlet and outlet.

#### 5.4.2.1 An equilibrium diffusion test

For this test, the inlet Mach number is set to 1.05. The radiation field and material are in equilibrium. The initial conditions are given in Table 5.3. The

Table 5.3: Initial conditions for Mach 1.05.

	left	right
$\rho$ ( $g/cm^3$ )	1.	1.0749588
$u$ ( $cm/sh$ )	0.1228902	0.1144127
$T$ ( $keV$ )	0.1	0.1049454
$\epsilon$ ( $jerk/cm^3$ )	$1.372 \cdot 10^{-6}$	$1.6642117 \cdot 10^{-6}$

computational domain is of size  $L = 0.08$   $cm$  and the initial step is at  $x_0 = 0.015$   $cm$ . The numerical solutions at steady state are given in Fig. 5.1, Fig. 5.2 and Fig. 5.3.

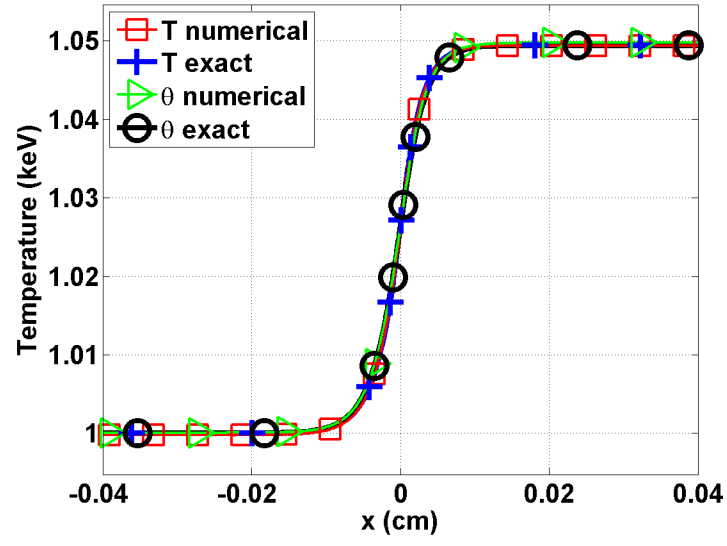


Figure 5.1: Material and radiation temperature profiles at steady state for Mach 1.05 test.

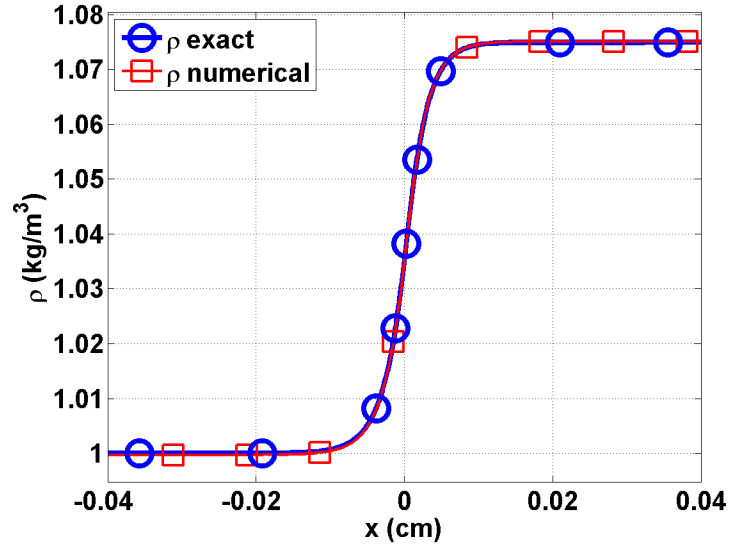


Figure 5.2: Material density profile at steady state for Mach 1.05 test.



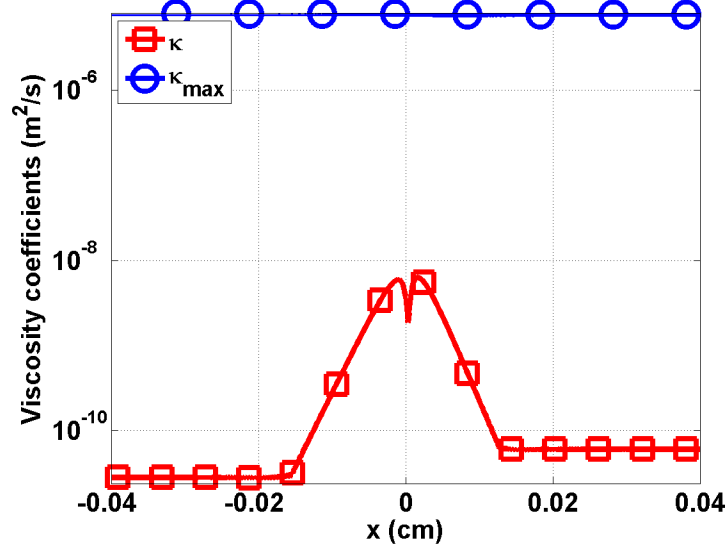


Figure 5.3: First-order viscosity  $\kappa_{max}$  and second-order viscosity  $\kappa$  profiles at steady state for Mach 1.05 test (logarithm scale).

The energy transfer between the material and radiation fields is not large enough to form a shock in the material. Thus, all of the material variables are smooth (Fig. 5.1 and Fig. 5.2) as well as the radiation temperature  $\theta$ . Because of the smoothness of the solution, the viscosity coefficient  $\kappa$  is three order of magnitude smaller than the first-order viscosity coefficient  $\kappa_{max}$  (Fig. 5.3).

#### 5.4.2.2 A 1.2 Mach hydrodynamic shock

In this test, the material experiences a shock and the radiation energy density remains smooth. The initial conditions, corresponding to a Mach number of 1.2 at the inlet, are as follows:

Table 5.4: Initial conditions for Mach 1.2.

	left	right
$\rho$ ( $g/cm^3$ )	1.	1.0749588
$u$ ( $cm/sh$ )	0.1405588	0.1083456
$T$ ( $keV$ )	0.1	0.1194751
$\epsilon$ ( $jerk s/cm^3$ )	$1.372 \cdot 10^{-6}$	$2.7955320 \cdot 10^{-6}$

The slab thickness is set to  $L = 0.045$   $cm$  and the initial step was located at  $x_0 = 0$   $cm$ .

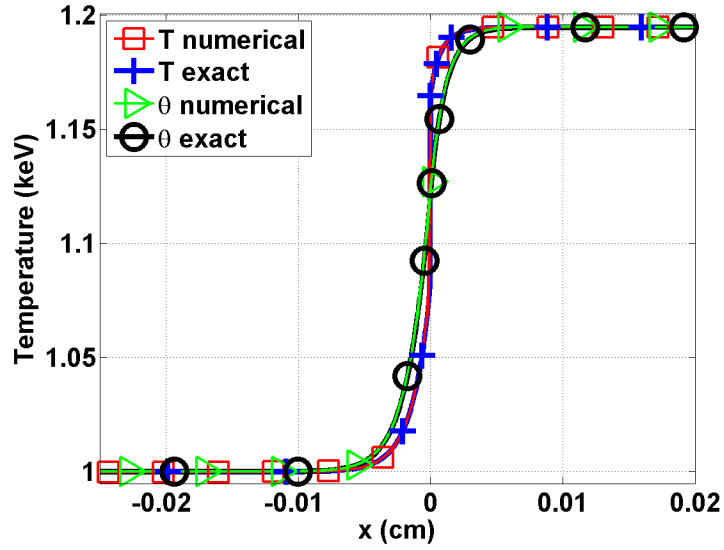


Figure 5.4: Material and radiation temperature profiles at steady state for Mach 1.2 test.

The radiation and material temperatures have two different behaviors (Fig. 5.4):

the later experiences an embedded hydrodynamic shock, whereas the radiation temperature is smooth because of the diffusion term. The material temperature profile does not show any pre- and post-shock oscillations. In Fig. 5.5, the material density profile has a shock as well. The viscosity coefficient (Fig. 5.6) is peaked in the shock as expected but does not saturate to the first-order viscosity. It is conjectured that the diffusion term in the radiation equation brings extra stability to the system. Overall, the numerical solution behaves as expected in the shock and the entropy-based viscosity method seems to efficiently stabilize the numerical scheme.

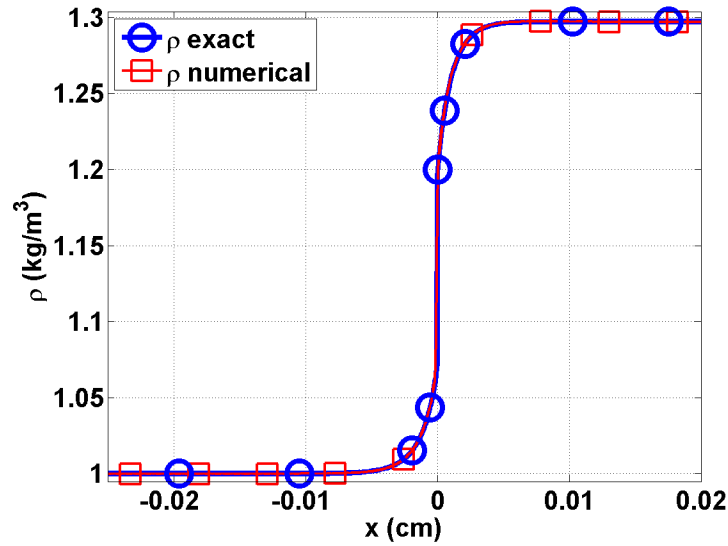


Figure 5.5: Material density profile at steady state for Mach 1.2 test.

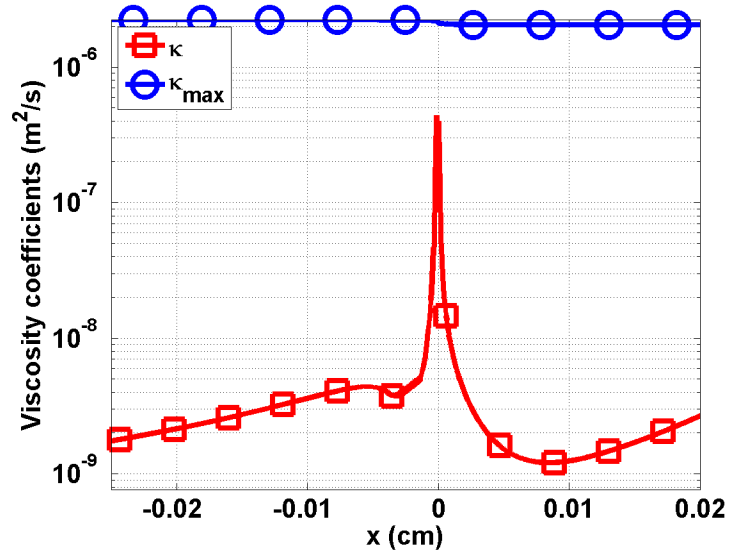


Figure 5.6: First-order viscosity  $\kappa_{\max}$  and second-order viscosity  $\kappa$  profiles at steady state for Mach 1.2 test (logarithm scale).

#### 5.4.2.3 A Mach 2 shock

The Mach 2 shock test has two features: a hydrodynamic shock and a Zeldovich spike, which make it interesting for testing the robustness of the entropy-based viscosity method. The initial conditions are specified in Table 5.5 for a slab of length  $L = 0.04 \text{ cm}$  with  $x_0 = 0. \text{ cm}$ .

Table 5.5: Initial conditions for Mach 2.

	left	right
$\rho$ ( $g/cm^3$ )	1.	1.0749588
$u$ ( $cm/sh$ )	0.1405588	0.1083456
$T$ ( $keV$ )	0.1	0.1194751
$\epsilon$ ( $jerk s/cm^3$ )	$1.372 \cdot 10^{-6}$	$2.7955320 \cdot 10^{-6}$

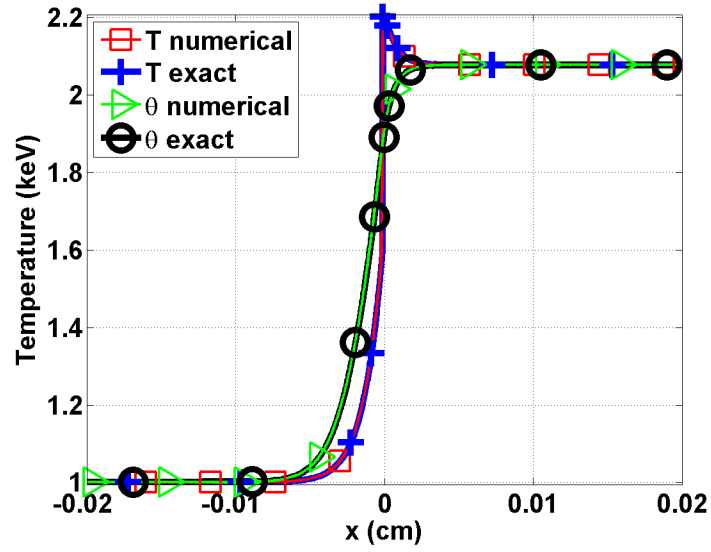


Figure 5.7: Material and radiation temperature profiles at steady-state for Mach 2 test.

Once again, the radiation temperature profile is smooth and the material temperature experiences an embedded hydrodynamic shock and a peak as shown in

Fig. 5.7. In Fig. 5.8, the shock is well resolved. The viscosity coefficient profile is given in Fig. 5.9 and is peaked, once again, in the shock region.

For comparison purpose, the same simulation was run with the first-order viscosity only, i.e.,  $\kappa$  was set equal to  $\kappa_{max}$  for the whole domain in order to see the advantage of using a second-order viscosity coefficient. The results are given in Fig. 5.10 for the material density and temperature. Numerical solutions with first- and second-order viscosity coefficients are graphed. The radiation temperature profile (not shown here) is not affected much by the first-order viscosity and the curves are coincident. This is expected because of the way the artificial viscosity term is treated in the radiation equation (Section 5.2). However, on the same figure, the shock and peak in the material temperature profile are smoothed out: the shock is not as sharp and the peak amplitude is reduced because of the larger amount of viscosity added to the system. This test shows the benefits of using a high-order viscosity coefficient in order to avoid over-dissipation.

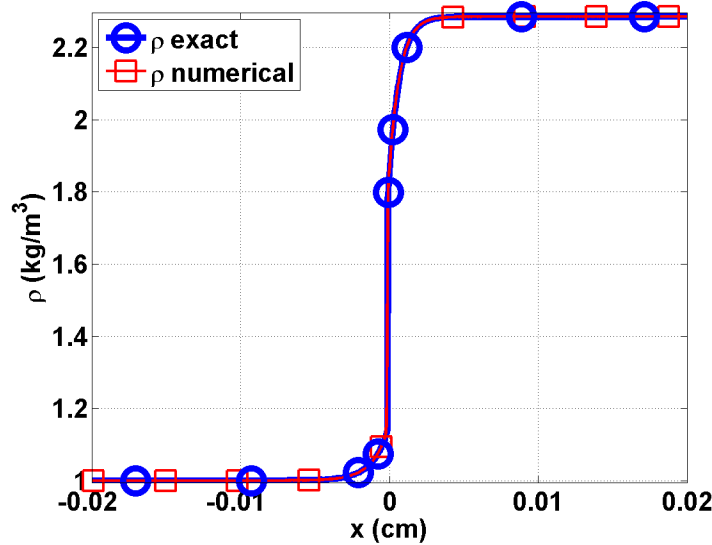


Figure 5.8: Material density profile at steady-state for Mach 2 test.

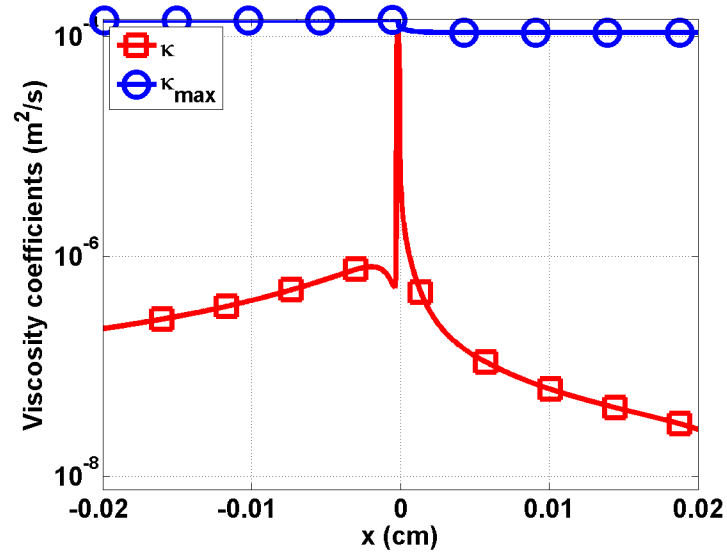


Figure 5.9: First-order viscosity  $\kappa_{max}$  and second-order viscosity  $\kappa$  profiles at steady state for Mach 2 test.

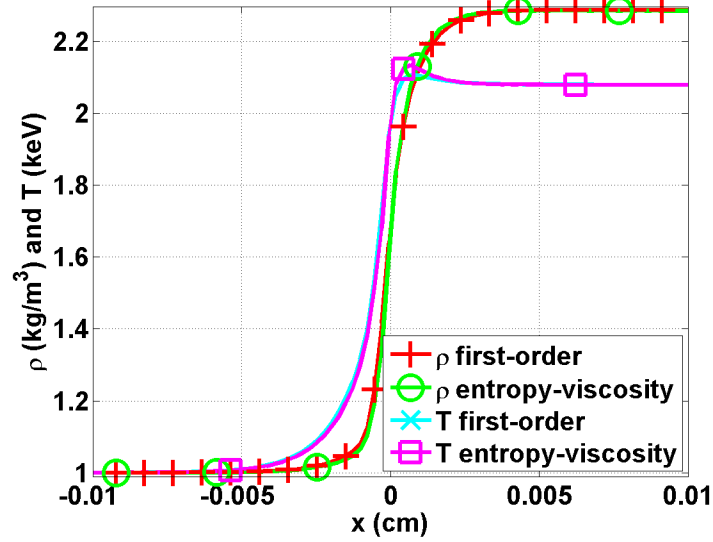


Figure 5.10: Comparison between the material density and temperature profiles run with the high-order and first-order viscosity coefficients.

#### 5.4.2.4 Mach 5 shock

A Mach 5 test is run with the initial conditions of Table 5.6 on a computational domain of length  $L = 0.05 \text{ cm}$  ( $x_0 = 0 \text{ cm}$ ). Steady-state results are shown in Fig. 5.11, Fig. 5.13, and Fig. 5.14 for the material and radiation temperatures, the density and the viscosity coefficients, respectively.

Table 5.6: Initial conditions for Mach 5.

	left	right
$\rho \text{ (g/cm}^3\text{)}$	1.	1.0749588
$u \text{ (cm/sh)}$	0.1405588	0.1083456
$T \text{ (keV)}$	0.1	0.1194751
$\epsilon \text{ (jerks/cm}^3\text{)}$	$1.372 \cdot 10^{-6}$	$2.7955320 \cdot 10^{-6}$



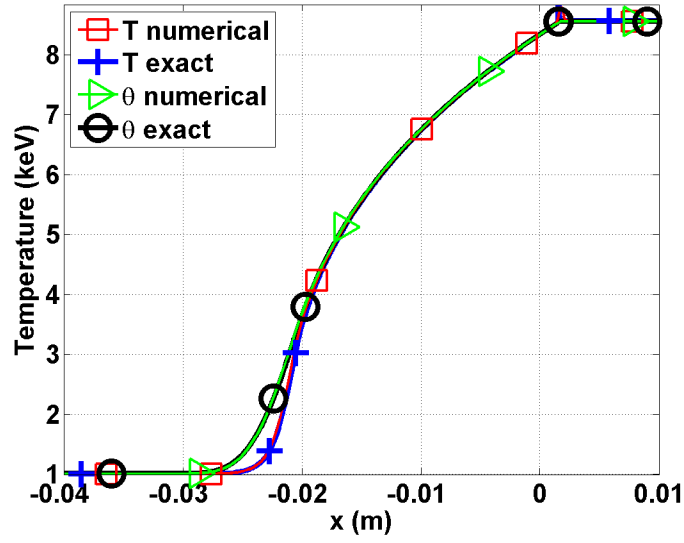


Figure 5.11: Material and radiation temperature profiles at steady state for Mach 5 test. Zoom at the location go the peak using different mesh resolutions.

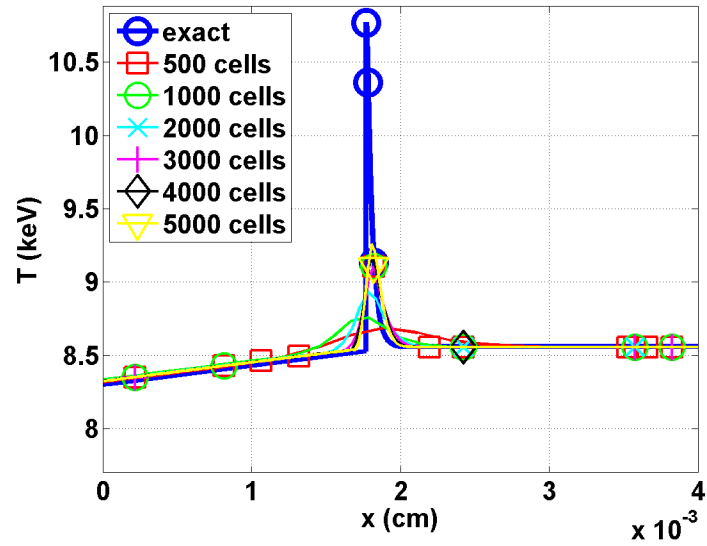


Figure 5.12: Material temperature profiles at steady state for the Mach 5 test in the neighborhood spike.

In Fig. 5.11, the radiation temperature profile is smooth. The material temperature no longer exhibits an embedded hydrodynamic shock but shows a Zeldovich spike. The mesh with 500 elements is not fine enough to correctly resolve the Zeldovich spike. In Fig. 5.12, the Zeldovich spike region is plotted for different mesh resolutions, using from 500 to 5000 elements: the peak is better resolved when using large numbers of elements and its position seems to be independent of the mesh size when appropriately refined. The density profile, Fig. 5.13, shows a shock located at the same position as the Zeldovich spike of the material temperature profile. The viscosity coefficient  $\kappa$  is also peaked in the shock region, as expected. The material and radiation variables do not present any numerical oscillations.

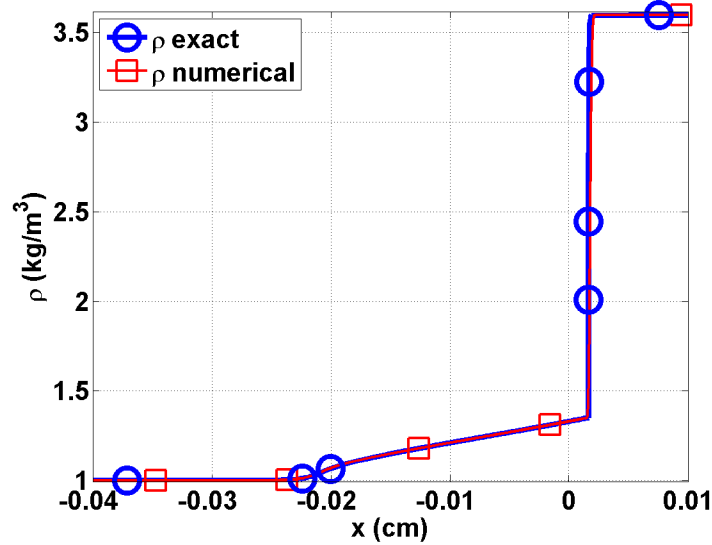


Figure 5.13: Material density profile at steady state for Mach 5 test.

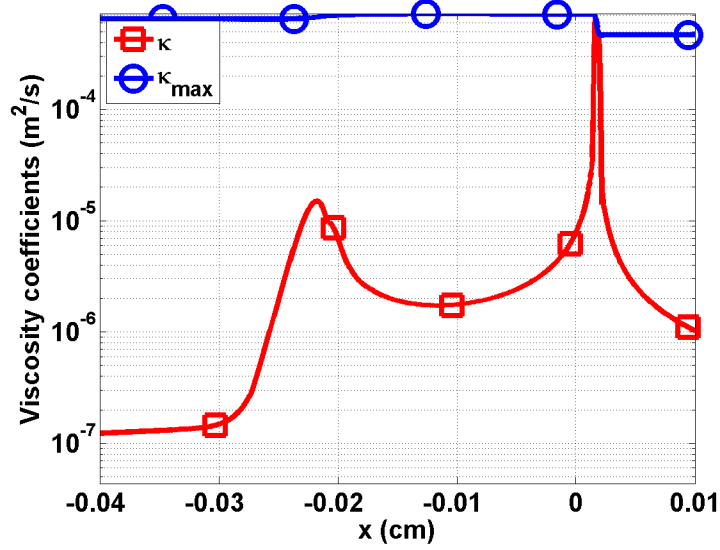


Figure 5.14: First-order viscosity  $\kappa_{max}$  and second-order viscosity  $\kappa$  profiles at steady state for Mach 5 test.

#### 5.4.2.5 Mach 50 shock

The Mach 50 test is known to be challenging. The initial conditions are given in Table 5.7. The computational domain is of length  $L = 0.2 \text{ cm}$ . Results are once again given at steady state.

Table 5.7: Initial conditions for Mach 50.

	left	right
$\rho \text{ (g/cm}^3\text{)}$	1.	6.5189217
$u \text{ (cm/sh)}$	585.6620	89.84031
$T \text{ (keV)}$	1.0	85.51552
$\epsilon \text{ (jerks/cm}^3\text{)}$	$1.372 \cdot 10^{-2}$	$7.33726 \cdot 10^5$

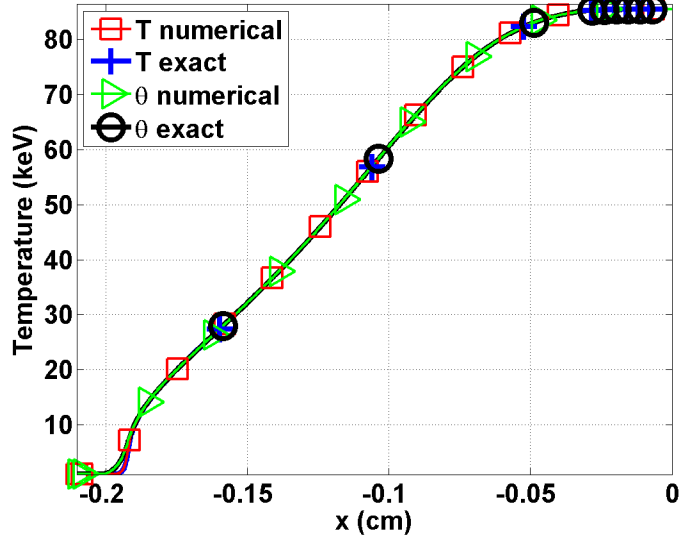


Figure 5.15: Material and radiation temperature profiles at steady state for Mach 50 test.

At Mach 50, there is no embedded hydrodynamic shock forming as shown in Fig. 5.15. The density profile is smooth as shown in Fig. 5.16. In Fig. 5.15, the material and radiation temperatures overlap on all of the computational domain except for a small region located between  $x = -0.2$  and  $x = -0.18$  cm. In this particular region, the viscosity coefficient saturates to the first-order viscosity (see Fig. 5.17) because of the inflection point in the material temperature profile. The artificial dissipative terms correctly stabilize the material temperature profile without altering the physical solution: the radiation temperature is expected to increase ahead of the material temperature.

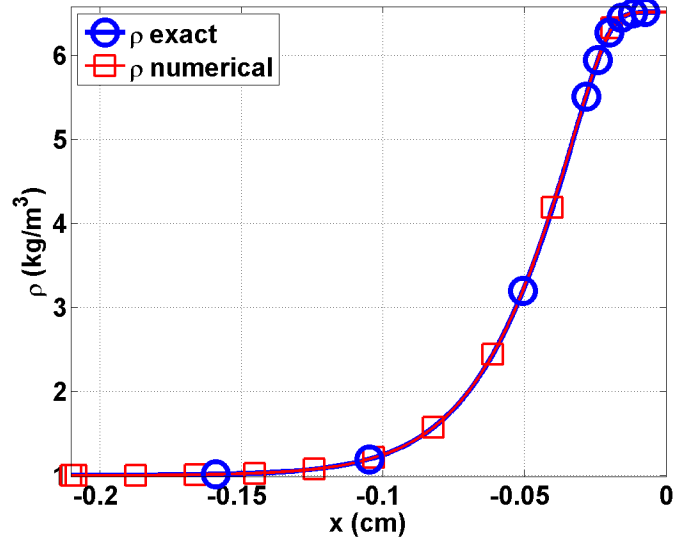


Figure 5.16: Material density profile at steady-state for Mach 50 test.

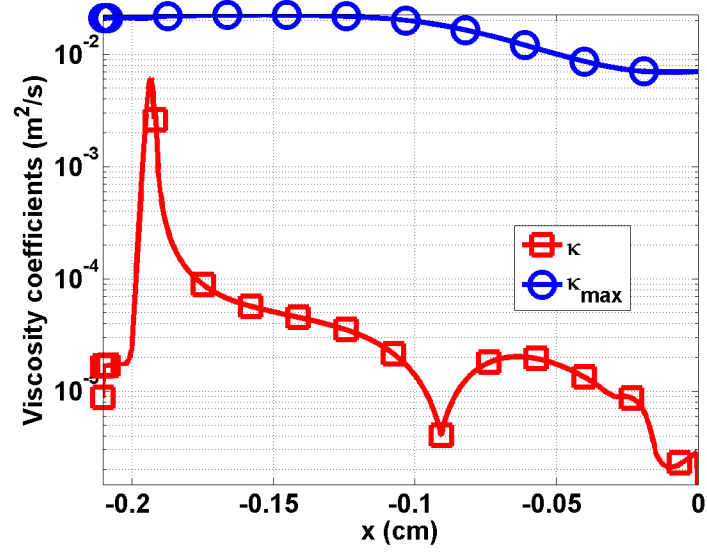


Figure 5.17: First-order viscosity  $\kappa_{max}$  and second-order viscosity  $\kappa$  profiles at steady-state for Mach 50 test.

## 5.5 Conclusions

In this paper, we have shown that the entropy-based viscosity method is a valid candidate for solving the 1-D radiation-hydrodynamic equations. A theoretical derivation is given for the derivation of the dissipative terms that are consistent with the entropy minimum principle. The viscosity coefficient  $\kappa$  is defined proportional to the entropy residual that measures the local entropy production allowing detection of shocks. Through the manufactured solution method, it is demonstrated, firstly, that second-order accuracy is achieved when the solution is smooth, and secondly, that the artificial dissipative terms do not affect the physical solution in the equilibrium-diffusion limit.

The entropy-based numerical scheme also behaves well in the tests performed for Mach numbers ranging from 1.05 to 50. The main features such as the embedded hydrodynamic shock and the Zeldovich spike are resolved accurately without spurious oscillations. The viscosity coefficient is peaked in the shock region only and behaves as expected. All of these results were obtained by using an unique definition of the viscosity coefficient that is computed on the fly. The addition of dissipative terms to the set of equations requires more computational work but is rather simple to implement.

As future work, extension to the multi-D equations could be considered: all of the derivations presented in this paper hold. The definition of the viscosity coefficients  $\kappa$  and  $\kappa_{max}$  do not need to be modified. It would be interesting to model the radiation equation with an  $S_n$  transport approximation and apply the entropy based artificial viscosity to the resultant radiation-hydrodynamics equations. Given the advective nature of the  $S_n$  equations, dissipation would need to be added to these equations.

fix spacing in bibliography, if any...

## REFERENCES

- [1] J D Anderson. Modern compressible flow. In *Guide for Verification and Validation in Computational Solid Mechanics.*, pages 10–2006, New York, 1982.
- [2] Perthane B. and Shu C-W. On positivity preserving finite volume schemes for euler equations. *Numer. Math.*, 73:119–130, 1996.
- [3] Dinshaw S. Balsara. An analysis of the hyperbolic nature of the equations of radiation hydrodynamics. *J. Quant. Spectrosc. Radiat. Transfer*, 61:617–627, 1999.
- [4] I Christov and B Popov. New non-oscillatory central schemes on unstructured triangulations for hyperbolic systems of conservation laws. *J Comput Phys*, 227:5736–5757, 2008.
- [5] B Cockburn, C Johnson, C Shu, and E Tadmor. Advanced numerical approximation of nonlinear hyperbolic equations. *Lecture Notes in Mathematics*, 1697:97109, 1998.
- [6] B Cockburn, C Johnson, C Shu, and E Tadmor. Advanced numerical approximation of nonlinear hyperbolic equations. *Lecture Notes in Mathematics*, 1697:97109, 1998.
- [7] B Cockburn, G Karniadakis, and C Shu. Discontinuous galerkin methods: theory, computation and applications. *Lecture Notes in Computer Science and Engineering*, 11:97109, 2000.
- [8] B Cockburn and C Shu. The local discontinuous galerkin method for time-dependent convection-diffusion systems. *Numer. Anal.*, 35:2440–2463, 1998.



- [9] G. Hansen D. Gaston, C. Newsman and D. Lebrun-Grandie. A parallel computational framework for coupled systems of nonlinear equations. *Nucl. Eng. Design*, 239:1768–1778, 2009.
- [10] Woodward P. R. Dai W. Numerical simulations for radiation hydrodynamics. i. diffusion limit. *Journal of Comput Phys*, 142:182–207, 1998.
- [11] D L Darmofal and K Siu. A robust multigrid algorithm for the euler equations with local preconditioning and semi-coarsening. *Journal of Computational Physics*, 151:728756, 1999.
- [12] R A DeVore and G G Lorentz. *Constructive Approximation*. Springer-Verlag, 1991.
- [13] J Donea and A Huerta. *Finite Element Methods for Flow Problems*. Oxford University Press, 2003.
- [14] J L Guermond and R Pasquetti. Entropy-based nonlinear viscosity for fourrier approximations of conservation laws. In *C.R. Math. Acad. Sci.*, volume 326, pages 801–806, Paris, 2008.
- [15] J-L. Guermond and B. Popov. Viscous regularization of the euler equations and entropy principles. *under review*, 2012.
- [16] H Guillard and C Viozat. On the behavior of upwind schemes in the low mach number limit. *Computers & Fluids*, 28:63–86, 1999.
- [17] Van Rosendale J Hussaini MY, van Leer B. Upwind and high-resolution schemes. *Berlin: Springer*, 12(1):1, 1997.
- [18] Leveque R. J. *Numerical methods for conservation laws*. Basel: Birhauser, Reading, Massachusetts, 1990.

- [19] B. Popov J-L. Guermond, R. Pasquetti. Entropy viscosity method for nonlinear conservation laws. *Journal Comput. Phys.*, 230:4248–4267, 2011.
- [20] R. Pasquetti J-L. Guermond. Entropy viscosity method for high-order approximations of conservation laws. *Lecture Notes in Computational Science and Engineering*, 76:411–418, 2011.
- [21] Robert B. Lowrie Jarrod D. Edwards, Jim E. Morel. Second-order discretization in space and time for radiation hydrodynamics. In *International Conference on Mathematics and Computational Methods Applied to Nuclear Science & Engineering (M&C 2013)*, Sun Valley, Idaho, USA, 2013.
- [22] Shi Jin and C. David Levermore. Numerical schemes for hyperbolic conservation laws with stiff relaxation terms. *Journal of Computational Physics*, 126:449–467, 1996.
- [23] Keyes D. E. Knoll D. A. Jacobian-free newton-krylov methods: a survey of approaches and applications. *Journal of Computational Physics*, 193:357–397, 2004.
- [24] J S Wong D L, Darmofal, and J Peraire. The solution of the compressible euler equations at low mach numbers using a stabilized finite element algorithm. *Comput. Methods Appl. Mech. Engrg.*, 190:5719–5737, 2001.
- [25] A Lapidus. A detached shock calculation by second order finite differences. *J. Comput. Phys.*, 2:154–177, 1967.
- [26] P. Lax. Weak solutions of nonlinear hyperbolic equations and their numerical computation. *Comm. Pure Appl. Math.*, 7:159–193, 1954.
- [27] S LeMartelot, B Nkonga, and R Saurel. Liquid and liquid-gas flows at all speeds: Reference solutions and numerical schemes. *Research report*, 7935:97109, 2012.

- [28] O LeMetayer, J Massoni, and R Saurel. Elaborating equation of state for a liquid and its vapor for two-phase flow models. *International Journal of Thermal Science*, 43:265–276, 2004.
- [29] X-S Li and C-W Gu. An all-speed roe-type scheme and its asymptotic analysis of low mach number behavior. *Journal of Computational Physics*, 227:5144–5159, 2008.
- [30] R Lohner. *Applied CFD Techniques: an Introduction based on Finite Element Methods*. 2<sup>nd</sup> Edition Wiley, 2003.
- [31] R Lohner, K Morgan, and J Peraire. A simple extension to multidimensional problems of the artificial viscosity due to lapidus. *Commun. Numer. Methods Eng.*, 1(14):141–147, 1985.
- [32] R Loubere. Validation test case suite for compressible hydrodynamics computation. *Theoretical Division T-7 Los Alamos National Laboratory*.
- [33] Hittinger J. Lowrie R., Morel J. Coupling radiation and hydrodynamics. *Journal Quant. Spectrosc. Radiat. Transfer*, 61:432–500, 1999.
- [34] B Muller. Low-mach number asymptotes of the navier-stokes equations. *Journal of Engineering Mathematics*, 34:97109, 1998.
- [35] P Perrot. *A to Z of Thermodynamics*. Oxford University Press, 1998.
- [36] J. D. Edwards R. B. Lowrie. Radiative shock solutions with grey non equilibrium diffusion. *Journal of Comput Phys*, 18:129–143, 2008.
- [37] O. LeMetayer R. Berry, R. Saurel. The discrete equation method (dem) for fully compressible, two-phase flows in ducts of spatially varying cross-section. *Nuclear Engineering and Design*, 240:3797–3818, 2010.

- [38] J.E. Morel R.B. Lowrie. Issues with high-resolution godunov methods for radiation hydrodynamics. *Journal of Quantitative Spectroscopy & Radiative Transfer*, 69:475–489, 2001.
- [39] J Reisner, J Serencsa, and Shkoller S. A space-time smooth artificial viscosity method for nonlinear conservation laws. *Journal of Computational Physics*, 253:912–933, 2013.
- [40] E. Tadmor. A minimum entropy principle in the gas dynamics equations. *Appl. Numer. Math.*, 2:211–219, 1986.
- [41] E.F. Toro. *Riemann Solvers and numerical methods for fluid dynamics*. 2<sup>nd</sup> Edition, Springer, 1999.
- [42] E Turkel. Preconditioned techniques in computational fluid dynamics. *Annu. Rev. Fluid Mech.*, 31:385–416, 1999.
- [43] J. Morel V. Zingan, J-L. Guermond and B. Popov. Implementation of the entropy viscosity method with the discontinuous galerkin method. *Journal of Comput Phys*, 253:479–490, 2013.
- [44] J von Neumann and R D Richtmyer. A method for the numerical calculation of hydrodynamic shocks. *J Appl Phys*, 190:232–237, 1950.